Functional fluorescent materials and migration dynamics of neural progenitor cells

Bossert, N.

FUNCTIONAL FLUORESCENT MATERIALS AND MIGRATION DYNAMICS OF NEURAL PROGENITOR CELLS

Proefschrift

ter verkrijging van
de graad van doctor aan de Universiteit Leiden,
op gezag van rector magnificus prof. dr. ir. H. Bijl,
volgens besluit van het college voor promoties
te verdedigen op donderdag 13 januari 2022
klokke 11:15 uur

door

Nelli BOSSERT

geboren te Kokchetav (Kazakhstan)
in 1986

Promotor:	Prof. dr. D. Bouwmeester
Co-Promotor:	Dr. D. M. Heinrich
Doctoral committee:	Dr. G. Noelke (Fraunhofer Institute Aachen, Germany)
	Dr. S. Streichan (USCB, Santa Barbara, USA)
	Prof. dr. J. Aarts
	Prof. dr. T. Schmidt
	Prof. dr. S. J. T. van Noort

Casimir PhD Series, Delft-Leiden 2021-46

ISBN 978-90-8593-509-4

An electronic version of this dissertation is available at
http://openaccess.leidenuniv.nl/

This work was supported by the Netherlands Organisation for Scientific Research (NWO/OCW), as part of the Frontiers of Nanoscience program.

The cover shows a neural progenitor cell spread out on a 2D honeycomb pattern. The cytoskeleton of the cell is fluorescently labelled showing actin in blue and microtubuli in green.

To my family and my husband.

CONTENTS

1

INTRODUCTION

1.1. GENERAL BACKGROUND

Cells are the building blocks of life. Research at the single cell level is crucial as it allows to unravel the complexity of this smallest living unit. On the inside, one cell holds a whole world of molecular machinery within its membrane. On the outside, it interacts and communicates with its environment and other cells. For complex mammalian organisms, understanding and influencing cells on individual level is fundamental to understanding and influencing them at the higher level of tissue, organs, and as a whole.

The development of light microscopy was crucial as it enabled to uncover the structure and dynamics of cells. However, cells are mainly composed of water and are thus translucent. Only the cellular membrane, the heterochromatin inside the cell nucleus, as well as several organelles are dense enough to be visible by light microscopy. For more detailed analysis, molecules and structures can be tagged with fluorescent materials allowing them to be better detectable. Beyond the mechanism of simple fluorescent tagging, functional materials have been created with capabilities to sense the environment or influence cells. Popular are systems enabling e.g., calcium concentration indication

or measurements of voltage change across the cellular membrane [1]. These tools also drive fundamental research and biomedical innovations.

Numerous fluorescent microscopy techniques exist allowing information acquisition for different research requirements. For example, a light sheet microscope is useful to study tissue assemblies [2], whereby Stochastic Optical Reconstruction Microscopy (STORM) is useful for high-resolution of small structures like microtubules [3]. For research on the single-cell level, light fluorescence microscopy has been widely employed. Hereby the entire sample is illuminated, and the resulting fluorescence collected, thus gathering also light from the out-of-focus planes (i.e., below and above the focal plane). Particularly when imaging cells the resulting images are blurry, as cells contain a high volume of liquid that scatters light. Laser scanning confocal microscopy (LSCM) employs a pinhole that blocks the out-of-focus light and creates greater resolution and lower noise levels. However, as the pinhole only illuminates a small area, the whole sample needs to be scanned line by line. This process is time-consuming and can cause photo-damage to live samples.

The design of the spinning disc confocal microscopy (SDCM) improves these conditions. Instead of a single pinhole as in the LSCM, the SDCM system uses a spinning disc with thousands of pinholes in it. These are arranged in a way that every point in the field of view is covered when the disc rotates, resulting in a simultaneous and thus fast illumination of the whole sample. The pinholes are placed with interspace between them to avoid crosstalk between the “mini-beams” of light going through the pinholes. However, these interspaces also block most of the excitation light. In the Yogokawa disc this condition is improved by an additional disc containing an array of micro-lenses that match the array of the pinholes sample [4]. These micro-lenses collect and focus the excitation light thus improving the illumination of the. To collect the image information, charge-coupled device (CCD) cameras are used. These are two-dimensional detectors that simultaneously record the spatial as well as the intensity information of all mini-beams thus leading to high speed of image acquisition. This high temporal resolution allows imaging of fast dynamic processes. Combined with the reduced photodamage resulting from the pinhole design, the SDCM system is particularly advantageous for the imaging of dynamic processes and motility of living cells and is the main method that was employed in this thesis.

Despite the lower photodamage in the SDCM system, light exposure can still be damaging for cells. Next to the damaging effect of high intensity light, the main phototoxic effect often results from fluorophore photobleaching [5]. With each illumination of the fluorescent sample a fraction of the fluorescent probe is irreversibly destroyed and additionally generates free radicals and other reactive breakdown products. The best way to reduce photodamage is to reduce exposure time and intensity during excitation, while still retaining a useful signal-to-noise ratio. Additionally, good cell permeability is crucial to accumulate enough fluorescent material inside the cell and beyond that the probe should not interfere with the biological system. Thus, fluorescent probes need to fulfil a range of requirements to ensure a healthy cellular state.

A myriad of fluorescent probes has been developed, each trying to perform better than previous probes. Their performance is defined by various features: (1) Photostability - the capability to withstand photobleaching. (2) Signal intensity - the brightness of

the emitted light, specified by the extinction coefficient (fraction of absorbed light at a given wavelength) and the quantum yield (ratio of emitted photons relative to absorbed photons). (3) Biocompatibility – defined as the inertness of the material to cellular environment, without perturbations of its system. (4) Cellular permeability or uptake - the internalization of probes over cellular membrane. (5) Specificity or functionality – defined as how well the aimed target or intended function is achieved. Material development aims at fulfilling the listed requirements, whereby different probes are needed for the diverse research questions and applications. The current range of available fluorescent materials is enormous and includes organic molecules, synthetic dyes, quantum dots, metal nanoparticles, silica nanoparticles, organic and inorganic polymers, nanotubes, and nucleic acid-based materials [6].

Despite technological advances in the design of fluorescent probes, many still face challenges of strong background fluorescence, photobleaching, or limited cell permeability. Fluorophores at higher energy with short wavelengths of the visible spectra, i.e., ultraviolet (e.g., Hoechst 33342 with excitation at 405 nm) and blue (e.g., GFP with excitation at 488 nm), usually yield bright signals but also result in higher phototoxicity [7, 8]. These probes are great for short-term experiments or snap shots. Fluorescent probes in lower energy with higher wavelengths, i.e., green (e.g., RFP with excitation at 561 nm), red (e.g., Cy5 with excitation at 647 nm), often yield less bright species but also have a lower photodamaging effect [7, 9]. These probes are useful for long-term imaging and frequent time-lapse experiments. The "perfect" fluorescent probe for a given experiment is rarely perfect, but most often a balance between the requirements and current possibilities. Each of the available materials were created to fulfill certain functions and the development of better and more functional materials is ongoing.

The work presented in this thesis encompasses different topics, centring around confocal microscopy of fluorescent objects and living cells. In the first part of this thesis, two functional fluorescent materials are employed. In chapter 2 DNA-encapsulated silver nanoclusters (Ag-DNA) are used as an intracellular sensor. In chapter 3 polymersomes are employed as a long-term imaging probe in living cancer cells. Both materials are very interesting for a wide range of applications and an overview of the multifaceted research as well as background information is given in the following sections (1.2 and 1.3).

The second part of this thesis focuses on neural progenitor cells (NPCs). In chapter 4 various fluorescent probes are tested for the purpose of long-term visualization of the NPCs and their nucleus during imaging. Chapter 5 observes and analyses the migratory dynamics of NPCs on uniform and patterned structures utilizing fluorescent reporters. Spinning-disc confocal microscopy and time-lapse imaging allow to resolve the dynamics of cell machinery and are employed here to gather data on NPC dynamics. Furthermore, *in vivo*, NPCs are surrounded by nano and micro-sized structures providing attachment sites and influencing their behaviour. Thus, various patterning techniques have been developed to mimic these structures *in vitro*, two of which are employed in this thesis. NPCs are in the focus of attention due to their inherent capabilities to regenerate the nervous system. Learning more about cellular behaviour and dynamics will provide more insights on organism development, as well as for treatment of central nervous system injuries and diseases. Background information on these fascinating cells is provided in section 1.4.

1

1.2. DNA-TEMPLATED SILVER NANOCLUSTERS (AG-DNA)

1.2.1. AG-DNA BACKGROUND AND PROPERTIES

Metals are intriguing materials as their size and shape determine their electrical, magnetic, and optical properties [10, 11]. Due to nearly freely moving electrons in the overlapping outer shells of metal atoms, they are exceptional electrical conductors and optical reflectors. Oscillations in the electron charge density on the surface of the metal, known as surface plasmons, can be induced through photon or electron excitation. Reducing the size of the metal to nanoparticle dimensions (i.e., 1 to 100 of nanometres), enables interesting coupling interactions with fields, dependent on the dimensions of the particle, including fluorescence emission. When the metal size is further decreased and approaches the Fermi wavelength of electrons (about 0.5 nm for Ag and Au), the band structure breaks up into discrete energy levels [12]. Thus, these metallic nanoclusters are expected to resemble the energy levels of molecules, equipping them with molecule-like properties [13]. Consequently, these metals show strong photoluminescence and photostability [14] and provide the link between single metal atoms and plasmonic metal nanoparticles.

Nanoclusters comprised of silver have been in focus due to their brighter fluorescence than gold particles [12] and their intrinsic anti-bacterial properties [15]. However, various factors affect the stability of silver nanoclusters in solution, leading to agglomeration and oxidation [16]. Polyanionic molecules with high affinity for silver ions have been utilized to protect the clusters, yielding water-soluble and stable silver nanoclusters under physiological conditions [17]. Among them are (synthetic) polymers, phosphines, proteins, solid matrices, thiolates, and nucleic acid molecules; all leading to nanoclusters with different fluorescence spectra and varying quantum yields [13, 16].

The combination of silver nanoclusters and DNA molecule in particular yields an intriguing blend, producing a new class of nanophotonics [18]. The metal clusters have been indicated to be rod-shaped [19], with varying resonances yielding emission wavelengths from the blue to the near infrared spectrum [18, 20]. Remarkably, because the DNA stabilization determines the size and shape of the cluster, the fluorescence of this hybrid molecule can be tuned by the selection of the DNA length and sequence [21, 22]. The connection with DNA bases appears to have a significant effect on the intrinsic optical properties of the nanoclusters, as only specific configurations exhibit significant fluorescence.

Ag-DNA exhibit a strong variation in optical properties with characteristics including bright fluorescence, high photostability [23], and quantum yields over 90% [19]. The optical properties of Ag-DNA are not only highly dependent on the nucleobase sequence, but also on pH and temperature and ultimately their cluster size and shapes. Further, because the DNA configuration influences which species exhibit fluorescence, after synthesis, their fluorescence can still be tuned or switched on and off through the interaction with nearby DNA templates [24, 25]. All these characteristics make these nanomaterials valid competitors to standard fluorophores. Compared to organic dyes, Ag-DNA can be brighter and more photostable. Compared to quantum dots, they are smaller and can be less toxic and less prone to blinking on longer timescales [26].

Beyond that, nucleic acid nanotechnology has exhibited tremendous advances in its field, by using the molecules as architectural elements to build nanostructures with var-

ious functionalities [27]. For more targeted applications, any recognition sequence can be integrated naturally into the DNA template without the need of chemical modifications. Additionally, being a natural molecule, DNA is fully biocompatible. This increases its value as a stabilizing ligand and facilitates broad application.

DNA-stabilized silver nanoclusters (Ag-DNA) were first introduced by the Dickson group in 2004 (Petty 2004). Since then, these nanomaterials have been employed for numerous applications as fluorescent trackers. Particularly its sensitivity to environmental cues, expressed through shifts in the fluorescence spectra, makes Ag-DNA a valuable tool for sensing applications. It has been applied for the detection of genetic mutations [25, 28, 29], as well as low concentrations of metal ions [30, 31] and DNA/RNA molecules [24, 32]. Additionally, the tuneable optical properties and easy positioning make these structures interesting for applications in nanophotonics and optoelectronics [18, 33].

Beyond that, existing research is strongly focused on uncovering the structure of the Ag-DNA and understanding how the tunability of the fluorescence spectra arises. Despite this focus, these nanomaterials are poorly understood in their formation pathways and photo-physical properties as it is challenging to obtain structural information. The conformational states of Ag-DNA are usually short-lived, impeding measurements to uncover its secondary structure. RNA can also be implemented to stabilize silver clusters [34], but DNA is the more favourable choice due to its higher stability.

The synthesis of Ag-DNA is relatively fast (1h), low in cost, and easy. However, due to oxidation by air and photobleaching, as well as continuing chemical interactions, many species are short-lived (i.e., hours) [35], and only specific purified samples show high stability (e.g., a certain 28mer is stable for 30 days at room temperature) [36].

To synthesize Ag-DNA, silver salts (such as $AgNO_3$) are mixed in a specific ratio with DNA templates and subsequently reduced, typically with sodium borohydride ($NaBH_4$). Although cations generally bind to the negatively charged phosphate backbone of the DNA, silver ions (Ag^+) associate with the DNA bases [37]. Hereby, silver ions show a strong affinity order for the bases, preferring cytosine over guanine, followed by adenine, and at last thymine [36, 38]. Reduction with (NaBH4) leads to nucleation of the neutral silver core (Ag_0), whereby silver ions in the periphery remain, acting as “glue” and connecting the silver core to the DNA bases (Figure 1.1).

Notably, upon synthesis, an individual DNA template produces a heterogeneous mixture of distinct Ag-DNA conformations and silver cluster products. Many of these species, present in a single solution, are non-fluorescent, whereby only about 25% might show high fluorescence (i.e., signal considerably higher than noise level) [39].

Recently, methods have been developed to isolate individual species. Using high-performance liquid chromatography with in-line mass spectrometry (HPLC-MS), it is possible to select for pure Ag-DNA complexes and to identify their total number of silver atoms and silver cations [39]. This method yields spectrally pure and more stable fluorescent products and facilitates the continued research and application of Ag-DNA.

1.2.2. TEMPLATE DESIGN AND STRUCTURE

To increase the pool of fluorescent species, cytosine- and guanine-rich sequences were found to be important [40, 41]. However, using solely homopolymers of cytosine

or guanine produces species with low temporal stability [42]. Thus, a mixture is necessary to produce fluorescent products with longer stability. Long oligomers were found to yield products with higher stability and tend to generate bigger clusters [19, 39, 43, 44].

Beyond that, the understanding of how the composition of a mixed-base sequence determines the cluster formation, is still poor. The range of possible permutations is enormous. Considering using a short template with only 10 bases, already allows for over 10 Million possible sequence arrangements [42]. Thus, the design of DNA templates is still tedious as finding effective sequences is generally done by experimentally testing them.

With advanced understanding of the interactions between silver ions and DNA bases, machine learning can be used to predict sequences that stabilize fluorescent clusters. Copp *et al.* (2014) used pattern recognition to find "base motifs" which favour radiative over non-radiative decay. A "base motif" consists of 3-5 bases which are necessary to encapsulate a cluster. Examples for found motifs include GCG, CGC, and GG_AC for bright clusters, and TTG, ATT, and AT_T for dark clusters, confirming the necessity of guanine and cytosine bases for a fluorescent product. Employing this model and a learning algorithm, the authors were able to predict templates that produce bright Ag-DNA with 80% accuracy [42].

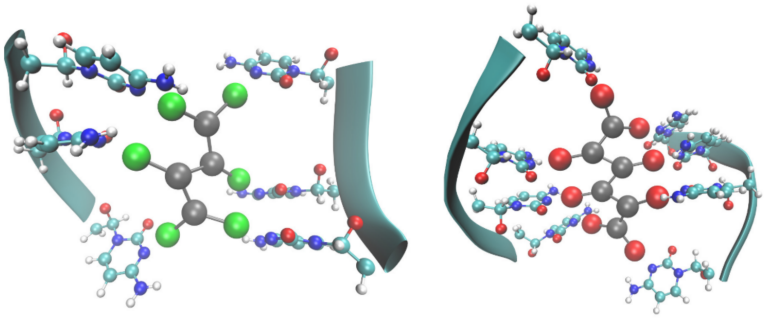

Figure 1.1: Illustration of Ag-DNA structures. Representation of Ag-DNA constructs containing four silver atoms (left) and six silver atoms (right), exhibiting fluorescence in the green (left) and red (right) spectrum. Grey represents the silver atoms, green and red colours represent silver cations. Figure from Taccone *et al.* (2018), *Physical Chemistry Chemical Physics* ([45]. (Image reprinted with permission of the rights holder, Royal Society of Chemistry).

Obtaining structural information of Ag-DNA is challenging. Many conformational states are very short-lived (milliseconds to seconds), thus only long-lived states can be measured. Interestingly, dynamic microstates were found to be intrinsic to the long-lived states [36]. In general, conformational transitions have been associated with optical changes [46, 47], but whether these microstates might influence the fluorescent properties of Ag-DNA, and how, was not determined. The shape of the DNA template is reorganized as silver ions bind to cytosine and guanine bases via nitrogen and oxygen sites. Hereby, an ion can be shared between these attachment sites within one base [36]. Contrary, in polyadenine and polythymine, silver ions were found to primarily affect sugar geometries [36].

Generally, single stranded DNA is employed as a template as it is more flexible than double stranded DNA and thus enables better silver incorporation. The commonly used template length consists of 12-30 bases [16, 23]. Due to steric constraints, short templates (< 15 bases) often form dimers which frame the silver cluster [34]. Longer templates also permit interstrand binding, like their short counterpart. Additionally, they often form intrastrand products by wrapping around the silver cluster. The shape of the neutral silver cluster core was repeatedly demonstrated to be rod-like [18, 19], whereby peripheral silver ions align along the DNA template. Thereby, their fluorescence properties are similar to larger nanorods, with resonance largely determined by their sizes and aspect ratios.

The optical properties of Ag-DNA were found to be primarily determined by the size and shape of the silver core. Larger clusters can be associated with higher wavelengths, as they permit greater delocalization of electronically excited states [39]. Dark species were found to appear at lower silver number (< 10), but silver content of 10 - 15 occurred both in dark and bright species [39]. Thus, silver content number by itself does not control whether the nanomaterial is fluorescent. Certain dark complexes can still be optically switched to become fluorescent e.g., by adding a guanine-rich template [24].

The total silver content of one cluster generally lies between 10-24 atoms [44], including neutral and positive atoms. A cluster with an equal number of neutral atoms may exhibit different numbers of ions and thus different charges, and vice versa. Analysing over 600 of 10-base templates and assessing past literature, Copp *et al.* (2014) found a domination of specific atom numbers, independent of the DNA length and sequence [44]. Groupings of 4 and 6 neutral atoms suggest enhanced stabilities around these numbers, while displaying wide-ranging numbers of cations. These termed “magic numbers” correspond to emissions at green (540 ± 20 nm) and red (630 ± 30 nm), respectively, producing the “magic colours”.

The fluorescence properties of Ag-DNA after synthesis can be influenced by factors that influence the DNA conformation such as pH and ionic strength. Additionally, silver ion movements can affect the shape of the silver chain modifying its aspect ratio and/or curvature, and consequently shifting the fluorescence spectra [48]. Smaller wavelength differences between Ag-DNA can also emerge from fluctuations in the number or type of bound bases [49]. This shows the incredible tunability of Ag-DNA pre and post synthesis.

Another remarkable feature is the existence of two distinct absorbance bands and only one emission band. Excitation of the nanomaterial can occur directly via the silver cluster or via the DNA bases [45, 50]. The excitation band via the silver cluster can be tuned within 480-750 nm, as discussed above. Contrary, excitation via the DNA bases is fixed at 260-270 nm and is general to all Ag-DNA species. For more information regarding the origin of photoluminescence and photodynamical properties of the DNA-Ag system, see Thyrhaug *et al.* (2017) [51] and Berdakin *et al.* (2016) [52].

1.2.3. AG-DNA IN CELLS

In contrast to the wide range of publications focusing on sensing ions, small molecules, and proteins in solution *in vitro* by Ag-DNA, research published on applications in (liv-

ing) cells is limited [53–55].

Despite the general high photostability, Ag-DNA face challenges in biological applications. Due to the highly negatively charged DNA backbone, repulsion between the membrane and the phosphate groups leads to poor internalization into cells. To circumvent this, methods like microinjection and transfection have been used successfully [56–58]. However, both methods are time-consuming and impact cellular viability. Further, modifications like the attachment of aptamers or cell penetrating peptide to DNA template were shown to achieve targeted cellular binding or cell penetration. For fixed cells, linking antibodies to Ag-DNA resulted in intracellular staining [55]. Another important challenge is the poor chemical stability of Ag-DNA in biological media and cellular environment. High salt concentrations present in physiological buffers or cell culture media usually lead to silver chloride precipitation and thus destruction of the nanoclusters. Additionally, nucleases within cells can digest the DNA template.

Choi *et al.* (2011) improved Ag-DNA stability by modifying several factors: increasing the base/silver ion ratio during synthesis, elongate and adapt the DNA template, and performing the synthesis directly in physiological buffer or cell culture media [55]. Another group succeeded to improve the stability by forming complexes comprised of Ag-DNA and polycationic electrolytes [57]. As there is high interest in simple and label-free bioimaging probes, the application of Ag-DNA will likely expand in this field when these fascinating nanomaterials are better understood.

In chapter 2 we present three different Ag-DNA forms with three different functionalities. Depending on the employed sequences either stable forms are created that can be used for intracellular labeling purposes or more sensitive forms that are useful as intracellular, optical sensors. Furthermore, the inherent cytotoxic effect due to the silver content in Ag-DNA materials, can be tuned and allows the generation of either biocompatible or low to high cytotoxic probes. Considering the growing interest of researchers to measure the biochemical processes and concentrations inside living cells, Ag-DNAs potential as a sensitive intracellular sensor becomes more and more relevant. Next, the tunability of the toxicity is also highly relevant and can become a powerful tool in cancer research and treatment.

1.3. POLYMERSOMES

1.3.1. POLYMERSOMES BACKGROUND AND PROPERTIES

The organisation and function of a eukaryotic cell is enabled by spatial compartmentalization with lipid membranes. The cell itself is separated from its environment by a double layered lipid membrane, mainly consisting of phospholipids and cholesterol. Likewise, within the cell, biomolecules and ions are confined within subcellular compartments allowing separation of biochemical reactions and degradation processes, as well as intracellular delivery and protection of biomolecules.

Beyond internal vesicles, which are crucial for intracellular function, extracellular vesicles (EVs) exist to coordinate intercellular communication. Practically all biological fluids have been found to contain EVs, including blood, saliva, breast milk, and in the supernatant of cultured cells [59], confirming their importance in cell-cell communication. EVs can efficiently deliver various biomolecules like DNA [60], RNA [61], or

functional proteins [62] to target cells. Hereby, the lipid membrane protects these cargoes from degradation by nucleases and proteases, which are commonly present in the extracellular environment. Currently, EVs are in the focus of attention as they have been demonstrated to participate in important physiological and pathological processes, like the immune response or neuronal degeneration [63, 64]. Due to these exceptional aspects, scientists are highly motivated to use this carrier system deliberately for disease treatment and biomedical research.

Although strategies exist to extract naturally occurring EVs and to load them with exogenous cargoes, these "modified-EVs" suffer from low yield, low purity, and little flexibility [65]. This challenge inspired researchers to create artificial EV counterparts, mimicking the lipid membrane which physically separates the aqueous inner compartment from the surround environment. While EVs have the advantage of full biocompatibility, artificial vesicles (AVs) can be easily synthesized in higher concentrations and modified according to the application requirements.

Liposomes are the best-known AVs and consist of a lipid bilayer of phospholipids, the natural components also integrated in the cellular membrane and vesicles. Their structure allows hydrophobic molecules to be encapsulated in the membrane, and hydrophilic molecules to be loaded into the aqueous lumen. Liposomes have been widely employed in research and as drug carriers, whereby several liposome formulations are FDA-approved [66]. However, liposome surface is strongly affected by interactions with circulating proteins in blood, a phenomenon called opsonization. Thus, liposomes generally display fast clearance due to opsonization by serum proteins and detection by the immune system [67]. Their circulation time can be highly increased by incorporating the polymer polyethylene-glycol (PEG) on the vesicles surface, thus sterically inhibiting electrostatic and hydrophobic interactions with plasma proteins [68]. However, further limitations are low stability and poor flexibility in the synthesis of conventional liposomes.

The main goal of AV development, is to create vehicles which can be loaded with variable cargoes, subsequently protect this cargo from degradation, and efficiently deliver it in a time- and space-controlled way, according to the required question. Thus, high tunability of the carrier vehicle is necessary. A successful approach to fulfill these needs is creating vesicular carriers by using fully synthetic polymers. Discher *et al.* (1999) was the first to implement amphiphilic block copolymers, which chemically resemble cellular phospholipids while displaying increased structural stability and mechanical resistance compared to liposomes [69]. The huge advantage of polymersomes is the high versatility of their physicochemical properties, which allows careful tuning of the physical properties of the AV for any biochemical application.

For the synthesis, one hydrophobic and one hydrophilic polymer are used as a pair, which self-assemble into a bi-layered structure as hydrogen bonds form between the polymers and the surrounding water molecules [70]. The palette of possibble constructions is considerable due to the broad range of available polymers like polyisobutylene-monomethyl polyethylene (PiB) or poly(2-(diisopropylamino)ethyl methacrylate) (PDPA). PEG plays also here an important, due to its stealth properties which grant the carrier with longer bioavailability *in vivo* [71].

1.3.2. POLYMERSOMES IN CELLS

The transport of polymersomes over the cellular membrane is crucial for any therapeutic or imaging application. Intracellular uptake of moieties depends on several factor, and polymersome size plays an important role [72]. Thus, the tuneability of polymersome diameter is highly advantageous and can be controlled via polymer concentration and mixing rate during synthesis [73]. Often the yield contains a broad size distribution, but this polydispersity can be reduced by using standard AV purification techniques like centrifugation or size exclusion chromatography [74].

One of the ways polymersomes can enter cells is via the clathrin-mediated endocytosis. Hereby, particles form contacts with cell surface receptors, initiating the cellular membrane to wrap around and subsequently internalize them [75]. Thereafter, the internalized vesicle (endosome) is actively transported along the cytoskeleton towards the perinuclear area, where the vesicle contents are selected for uptake or secretion. To achieve targeted delivery to particular cell types, polymersome surface is often modified with homing ligands such as aptamers, antibodies, metabolites [76]. Further, controlled cargo release can be attained by creating stimulus-responsive polymersomes which dissociate in response to pH, temperature, redox agents, or light [77]. Due to its synthetic nature, the clearance of polymersomes is often lower than for liposomes, which ensures longer circulation times but can lead to undesired accumulation. Employing biodegradable polymers like polylactide (PLA) and poly(caprolactone) PCL is thus becoming a favourable choice [78].

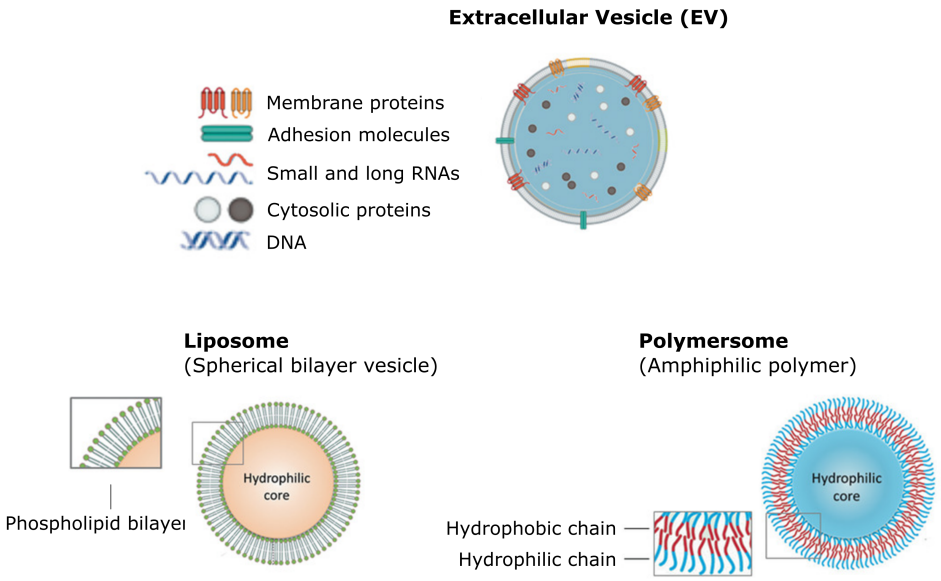

Figure 1.2: Illustration of the membrane compositions of extracellular and artificial vesicles. a) An extracellular vesicle (EV) is comprised of membrane proteins and adhesion molecules, containing various molecules in its aqueous interior. b) A liposome is comprised of a shperical bilayer vesicle with a hydrophilic core. c) The membrane of a polymersome vesicle is built by amphiphilic polymers, containing hydrophobic and hydrophilic chains, and encloses an aqueous interior. Modified figure from Leggio *et al.* (2020), *Advanced Healthcare Materials* ([79]. (Image reprinted and adapted with permission of the rights holder, John Wiley & Sons - Books).

Morphology of polymersomes can also be controlled via the ratio of hydrophilic-to-hydrophobic sections resulting in micelles, ellipsoids, vesicles, or tubular structures. Spherical polymersomes are more common being the thermodynamically most stable structure. Further, the choice of polymer as well as the hydrophilic-to-hydrophobic ratio determine additional physicochemical properties such as the permeability, thickness, rigidity, and surface charge of the membrane [70]. All features influence polymersome function as well as cellular uptake and thus enable adaptability of the carrier to the question of research.

Polymersomes high mechanical and chemical stability as well as their capability to encapsulate molecules makes them interesting systems for *in vivo* fluorescence imaging in cells, tissue, or small animals. As carriers of imaging probes, they serve to improve fluorophore limitations like low tissue penetration, short half-life circulation and fast photo-bleaching. Due to their capacity to entrap large volumes of moieties in their inner aqueous compartment as well as their membrane, high local concentration of fluorophores can be achieved yielding robust fluorescent signal. Combining pH-sensitivity and fluorophore-loading, Massignani *et al.* (2010) achieved efficient endosomal escape and subsequent cytosolic labelling of living cells [80]. By comparing Rhodamine encap-

sulated in a polymersome to not encapsulated CellTracker^{TM} dye, the former was found to be longer fluorescent (up to 14 days) and non-toxic, in contrary to the pure dye, confirming the advantages of employing polymersomes.

Fluorescent polymersomes are widely employed for imaging purposes in living cells or whole organisms like the zebrafish [81, 82]. Further, they are highly interesting for biomedical applications focusing on targeted drug-delivery and tumor-imaging [70]. However, studies are lacking that analyse the dynamics of polymersome uptake, their potential as long-term imaging probes, as well as their degradation in cells. Investigating these processes is important and would provide more insights for research and biomedical application of polymersomes.

In chapter 3 the capacity of polymersomes to entrap an aqueous and a lipophilic dye simultaneously and their ability to preserve the fluorescence of these dyes longer was used. Here, dual-labeled polymersomes were employed for live-cell imaging. By labelling the membrane as well as the interior of the nanovesicle, a great tool was created that allowed to observe the integrity of the polymersomes inside living cells and follow them over days, with hardly impacting the cellular health state. We observed a fast uptake of the dual-labeled polymersomes and could confirm their stable fluorescence over an imaging period of 86 h. Further, the particles were divided on average 50-50 among daughter cells, thus facilitating tracking of all cells equally while their proliferate. At day 7, we observed a strong decrease in fluorescence intensity, whereby the membrane dye showed a higher signal than the encapsulated dye, suggesting a rupture of numerous polymersomes. This highlights the practicality of using dual-labeled vesicles for imaging as a clear indicator of their state. Our results showed that the employed polymersomes are excellent candidates for *in vivo* imaging application for observation periods of up to 3 days.

1.4. NEURAL PROGENITOR CELLS

1.4.1. BACKGROUND INFORMATION

Neurogenesis is a complex process whereby new neural cells are generated. It takes place through proliferation, migration, and eventual differentiation of neural progenitor cells (NPCs) into mature neurons and glial cells. Neurogenesis mainly occurs during embryonic and early postnatal development but is also known to prevail throughout adulthood [83, 84]. In the adult brain, NPCs reside within specialized neurogenic niches which provide the necessary environment to support their maintenance and development of NPCs [85]. NPCs are characterized based on their location in the brain, gene expression profile, temporal distribution, and morphology [86]. Since the research in this thesis mainly focuses on the general mobility and interaction characteristics of NPCs, the complex organization of these niches as well as the terminology of NPC subtypes will not be elaborated on. For more information on this topic see Obernier and Alvarez-Buylla (2019) [85] and Martinze-Cerdeno *et al.* (2018) [86].

Between species, major differences exist regarding the spatial regions in which neurogenesis occurs as well as the extent to which neurogenesis happens [87]. In rodents, the two prominent niches are the subventricular zone (SVZ) of the lateral ventricle and the subgranular zone in the dentate gyrus (SGZ) of the hippocampus. In humans, the

SGZ and the striatum are most active [88, 89].

Neural progenitors in the SGZ generate new excitatory neurons for the dentate gyrus, which are important for learning, pattern recognition, and memory [90, 91]. In the SVZ, NPCs are destined to migrate long distances (3-8 mm in mice) to the olfactory bulb (OB) and differentiate into olfactory interneurons [92]. These are important for fine odour discrimination as well as odour-reward association [93, 94].

The pathway connecting the SVZ and OB is called the rostral migratory stream (RMS) (Figure 1.3. Here, NPCs migrate in chains using blood-vessels and glia cells as guiding structures [95, 96]. Interestingly, in case of an injury, the traveling NPCs can exit the RMS, or migrate directly from the SVZ, towards the injury side following the inflammatory signal [97, 98]. Once arrived at their destination, NPCs can generate functional neurons and integrate into the existing network [99, 100], showing regenerative capacity of the adult brain. Since the heterogeneity of neural subtypes in the CNS is huge, an extensive variety of cell types must be generated for regeneration.

1.4.2. NPCS FOR CENTRAL NERVOUS SYSTEM REGENERATION

NPCs are an exceptional tool here as their multipotency enables them to differentiate into different neuronal and glial cells, depending on the environmental cues. Besides this direct regenerative mechanism, NPCs secrete neurotrophic factors including BDNF, NGF, and VEGF, which support the survival and function of damaged tissue [101, 102]. For this reason, the “secretome” of NPCs has been in focus of research and has been shown to improve the condition of neurodegenerative diseases in animal models [103, 104]. Neurodegenerative diseases like Parkinson’s disease (PD), Alzheimer’s disease (AD), or amyotrophic lateral sclerosis (ALS), as well as injuries like stroke and spinal cord damages, affect millions of people worldwide without the possibility to arrest its progress or cure its state. Considering the current lack of efficient treatments for central nervous system (CNS) injuries and degenerative disease, the regenerative ability of NPC is highly interesting. Despite the natural ability of NPCs to regenerate, the innate response is by far not sufficient to recover the damages caused by physical injuries or neurological disorders [105–107].

Currently, two promising approaches exist which focus on harnessing the full regenerative potential of NPCs. The first way is the mobilization and recruitment of endogenous NPCs. Utilizing internal NPCs has the advantage of avoiding immunocompatibility problems [108]. Mobilization means achieving a higher release of NPCs from their niche, and recruitment means attracting the cells to a specific location. For both goals, biochemicals can be employed. For NPC mobilization, Leukemia inhibitory factor (LIF) can be used, as it plays an important role in proliferation and fate regulation [109, 110]. To recruit NPCs to the injury location, factors like stromal cell-derived factor-1 (SDF-1) and hepatocyte growth factor (HGF) have been shown to successfully act as chemoattractants [111, 112]. The second way is the injection of exogenous NPCs which have been differentiated *in vitro* or isolated from another source. Transplantation of exogenous NPCs into animal models of various neurodegenerative diseases has been shown to result in functional improvements [113, 114]. The benefits of this method include the possibility to control various factors, e.g., by genetically modifying cells to overexpress

1

neurotrophic factors. Current challenges with this technique include well-characterized cells, height of dose numbers, low viability upon transplantation, as well as sufficient migration, differentiation, and network integration at the impaired location [115].

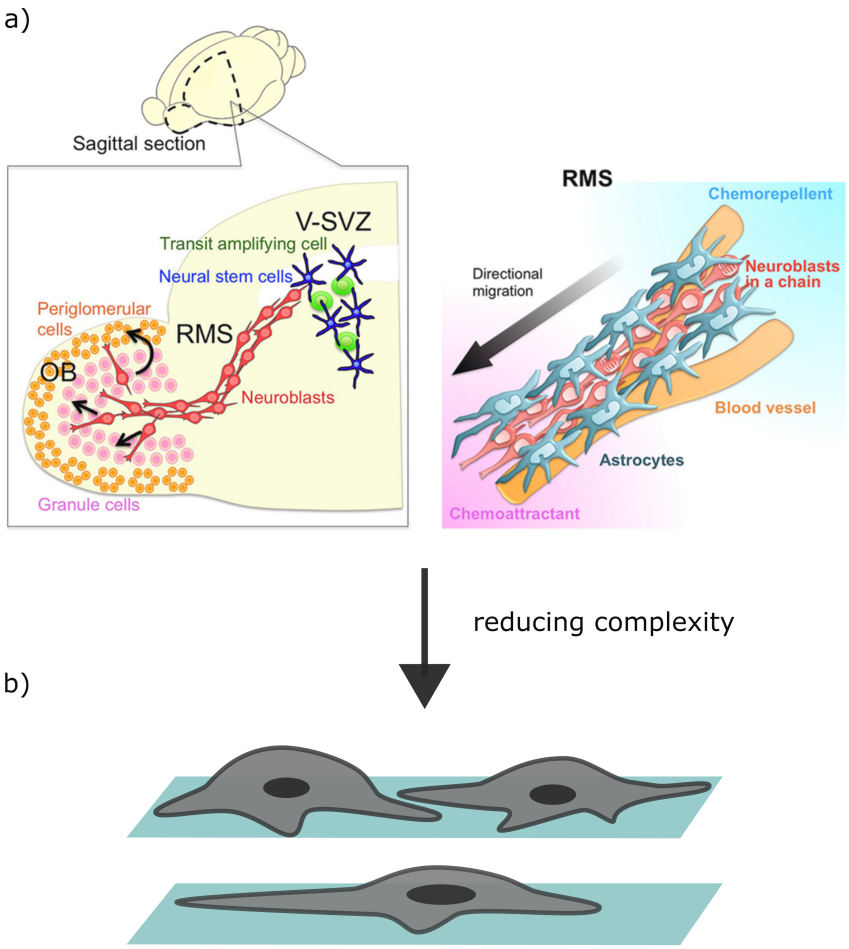

Figure 1.3: Illustration of RMS and V-SVZ localization and composition. a) Overview of the migration of neuroblasts within the RMS, starting in the V-SVZ and moving towards the OB. Overview of the situation of an injury and the migration of neuroblasts from the RMS and V-SVZ towards the lesion site. Figure modified from Kaneko *et al.* (2017), ([116]. (Image reprinted and adapted with permission of the rights holder, John Wiley & Sons - Books)

For therapeutic effects of NPC treatments, it is crucial that high numbers of cells arrive at specific locations. Direct injection is not always possible, especially when the damage is spread out throughout the brain as in neurodegenerative diseases. Thus, it is essential to understand the migration mechanism of NPCs and the influence of the environment on their motion capability. Available studies on NPC migration mainly focus on their progressive movement within days or weeks, and the final arrival at the side of inflammation [117–119]. Although these results give valuable insights into the migratory capacity of NPCs, data on the fundamental migratory behaviour on the timescale of minutes and hours is missing.

Despite the success of complex *in vivo* studies, *in vitro* experiments can still give important information as they provide a clean and fully controllable environment. Most *in vitro* studies on NPC focus on their lineage progression [120, 121], as their commitment to a differentiated state is still an important field to understand, or they look only at the broad migration distances [122]. However, hardly any studies analyse the fundamental migratory behaviour of NPCs. Since multiple factors influence the safe journey of migrating NPCs, collecting *in vitro* migration data on a single-cell level will enhance understanding of their innate characteristics and ultimately contribute to advancement in clinical applications. Multiple possibilities exist to reduce the complexity of an *in vivo* system but still emulate the different factors that cells encounter while migrating. By using patterning techniques to print lines and other geometries on 2D surfaces, minimalistic systems can be created that mimic the scaffold of blood vessels and astrocytes along which NPCs migration *in vivo*. To simulate the pores and tight openings that NPCs need to squeeze through on their journey, 3D channels with confinements present a great *in vitro* analysis system. Both systems are employed in chapter 5.

Chapter 5 focuses on the biophysical basics of NPCs with and without physical constrictions using patterned surfaces. In experiments we observed that NPC motility can be described by the mathematical persistent-random motion (PRW) model, whereby cells move with persistence on long time scale but show random motion on long time scale. Constricting NPCs to line patterns did not influence their velocity but did reduce the persistence time. Interestingly, by observing the cells visually on lines and more complex geometries, we detected several behavioral patterns highlighting how these cells interact with each other and explore their environment. Lastly, NPCs readily migrated through narrow 3D channels and squeezed through tight pores with a smaller size than their nucleus. The preliminary observations of NPC made on the various *in vitro* environments contribute to our understanding of their inherent behaviour and provide tools for further investigations.

1

1.5. REFERENCES

[1] Rishikesh U Kulkarni and Evan W Miller. “Voltage imaging: pitfalls and potential”. In: *Biochemistry* 56.39 (2017), pp. 5171–5177.

[2] Elizabeth MC Hillman et al. “Light-sheet microscopy in neuroscience”. In: *Annual review of neuroscience* 42 (2019), pp. 295–313.

[3] Jianquan Xu, Hongqiang Ma, and Yang Liu. “Stochastic optical reconstruction microscopy (STORM)”. In: *Current protocols in cytometry* 81.1 (2017), pp. 12–46.

[4] Shinya Inoué and Ted Inoue. “Direct-view high-speed confocal scanner: the CSU-10”. In: *Cell biological applications of confocal microscopy* (2002), pp. 88–128.

[5] Jaroslav Icha et al. “Phototoxicity in live fluorescence microscopy, and how to avoid it”. In: *BioEssays* 39.8 (2017), p. 1700003.

[6] Elizabeth A Specht, Esther Braselmann, and Amy E Palmer. “A critical and comparative review of fluorescent tools for live-cell imaging”. In: *Annual review of physiology* 79 (2017), pp. 93–117.

[7] Stephen Douthwright and Greenfield Sluder. “Live cell imaging: assessing the phototoxicity of 488 and 546 nm light and methods to alleviate it”. In: *Journal of cellular physiology* 232.9 (2017), pp. 2461–2468.

[8] Martin Purschke et al. “Phototoxicity of Hoechst 33342 in time-lapse fluorescence microscopy”. In: *Photochemical & Photobiological Sciences* 9.12 (2010), pp. 1634–1639.

[9] Samantha L Hopkins et al. “An in vitro cell irradiation protocol for testing photopharmaceuticals and the effect of blue, green, and red light on human cancer cell lines”. In: *Photochemical & Photobiological Sciences* 15.5 (2016), pp. 644–653.

[10] Younan Xia et al. “Shape-controlled synthesis of metal nanocrystals: simple chemistry meets complex physics?” In: *Angewandte Chemie International Edition* 48.1 (2009), pp. 60–103.

[11] Mostafa A El-Sayed. “Small is different: shape-, size-, and composition-dependent properties of some colloidal semiconductor nanocrystals”. In: *Accounts of chemical research* 37.5 (2004), pp. 326–333.

[12] Jie Zheng, Philip R Nicovich, and Robert M Dickson. “Highly fluorescent noble-metal quantum dots”. In: *Annu. Rev. Phys. Chem.* 58 (2007), pp. 409–431.

[13] Yen-Chun Shiang et al. “Fluorescent gold and silver nanoclusters for the analysis of biopolymers and cell imaging”. In: *Journal of Materials Chemistry* 22.26 (2012), pp. 12972–12982.

[14] Libing Zhang and Erkang Wang. “Metal nanoclusters: new fluorescent probes for sensors and bioimaging”. In: *Nano Today* 9.1 (2014), pp. 132–157.

[15] Svitlana Chernousova and Matthias Epple. “Silver as antibacterial agent: ion, nanoparticle, and metal”. In: *Angewandte Chemie International Edition* 52.6 (2013), pp. 1636–1653.

[16] Sungmoon Choi, Robert M Dickson, and Junhua Yu. “Developing luminescent silver nanodots for biological applications”. In: *Chemical Society Reviews* 41.5 (2012), pp. 1867–1891.

[17] M Mostafavi et al. “Early steps of formation of silver/polyacrylate complexed oligomer clusters. A pulse radiolysis study”. In: *International Journal of Radiation Applications and Instrumentation. Part C. Radiation Physics and Chemistry* 40.6 (1992), pp. 445–450.

[18] Elisabeth Gwinn et al. “DNA-protected silver clusters for nanophotonics”. In: *Nanomaterials* 5.1 (2015), pp. 180–207.

[19] Danielle Schultz et al. “Evidence for rod-shaped DNA-stabilized silver nanocluster emitters”. In: *Advanced materials* 25.20 (2013), pp. 2797–2803.

[20] Min Yang et al. “The Fluorescent Palette of DNA-Templated Silver Nanoclusters for Biological Applications”. In: *Frontiers in Chemistry* 8 (2020), p. 1089.

[21] Jeffrey T Petty et al. “Optically enhanced, near-IR, silver cluster emission altered by single base changes in the DNA template”. In: *The Journal of Physical Chemistry B* 115.24 (2011), pp. 7996–8003.

[22] Liam E Yourston et al. “First Step Towards Larger DNA-Based Assemblies of Fluorescent Silver Nanoclusters: Template Design and Detailed Characterization of Optical Properties”. In: *Nanomaterials* 9.4 (2019), p. 613.

[23] Tom Vosch et al. “Strongly emissive individual DNA-encapsulated Ag nanoclusters as single-molecule fluorophores”. In: *Proceedings of the National Academy of Sciences* 104.31 (2007), pp. 12616–12621.

[24] Hsin-Chih Yeh et al. “A DNA- silver nanocluster probe that fluoresces upon hybridization”. In: *Nano letters* 10.8 (2010), pp. 3106–3110.

[25] Hsin-Chih Yeh et al. “A fluorescence light-up Ag nanocluster probe that discriminates single-nucleotide variants by emission color”. In: *Journal of the American Chemical Society* 134.28 (2012), pp. 11550–11558.

[26] Judy M Obliosca et al. “DNA/RNA detection using DNA-templated few-atom silver nanoclusters”. In: *Biosensors* 3.2 (2013), pp. 185–200.

[27] Thomas Schlichthaerle et al. “DNA nanotechnology and fluorescence applications”. In: *Current opinion in biotechnology* 39 (2016), pp. 41–47.

[28] Weiwei Guo et al. “Highly sequence-dependent formation of fluorescent silver nanoclusters in hybridized DNA duplexes for single nucleotide mutation identification”. In: *Journal of the American Chemical Society* 132.3 (2010), pp. 932–934.

[29] Donny de Bruin et al. “Measuring DNA hybridization using fluorescent DNA-stabilized silver clusters to investigate mismatch effects on therapeutic oligonucleotides”. In: *Journal of nanobiotechnology* 16.1 (2018), pp. 1–8.

[30] Weiwei Guo, Jipei Yuan, and Erkang Wang. “Oligonucleotide-stabilized Ag nanoclusters as novel fluorescence probes for the highly selective and sensitive detection of the Hg2+ ion”. In: *Chemical communications* 23 (2009), pp. 3395–3397.

[31] Guo-Yu Lan, Chih-Ching Huang, and Huan-Tsung Chang. “Silver nanoclusters as fluorescent probes for selective and sensitive detection of copper ions”. In: *Chemical Communications* 46.8 (2010), pp. 1257–1259.

[32] Seong Wook Yang and Tom Vosch. “Rapid detection of microRNA by a silver nanocluster DNA probe”. In: *Analytical chemistry* 83.18 (2011), pp. 6935–6939.

[33] Tae-Hee Lee et al. “Single-molecule optoelectronics”. In: *Accounts of chemical research* 38.7 (2005), pp. 534–541.

[34] Danielle Schultz and Elisabeth Gwinn. “Stabilization of fluorescent silver clusters by RNA homopolymers and their DNA analogs: C, G versus A, T (U) dichotomy”. In: *Chemical communications* 47.16 (2011), pp. 4715–4717.

[35] SY New, ST Lee, and XD Su. “DNA-templated silver nanoclusters: structural correlation and fluorescence modulation”. In: *Nanoscale* 8.41 (2016), pp. 17729–17746.

[36] Danielle Schultz et al. “Structural insights into DNA-stabilized silver clusters”. In: *Soft matter* 15.21 (2019), pp. 4284–4293.

[37] H Arakawa, JF Neault, and HA Tajmir-Riahi. “Silver (I) complexes with DNA and RNA studied by Fourier transform infrared spectroscopy and capillary electrophoresis”. In: *Biophysical Journal* 81.3 (2001), pp. 1580–1587.

[38] Sourabh Shukla and Murali Sastry. “Probing differential Ag+–nucleobase interactions with isothermal titration calorimetry (ITC): Towards patterned DNA metallization”. In: *Nanoscale* 1.1 (2009), pp. 122–127.

[39] Danielle Schultz and Elisabeth G Gwinn. “Silver atom and strand numbers in fluorescent and dark Ag: DNAs”. In: *Chemical Communications* 48.46 (2012), pp. 5748–5750.

[40] Bidisha Sengupta et al. “Base-directed formation of fluorescent silver clusters”. In: *The Journal of Physical Chemistry C* 112.48 (2008), pp. 18776–18782.

[41] Matías Berdakin et al. “DNA-protected silver emitters: charge dependent switching of fluorescence”. In: *Physical Chemistry Chemical Physics* 19.8 (2017), pp. 5721–5726.

[42] Stacy M Copp et al. “Base motif recognition and design of DNA templates for fluorescent silver clusters by machine learning”. In: *Advanced Materials* 26.33 (2014), pp. 5839–5845.

[43] Jeffrey T Petty et al. “Near-infrared silver cluster optically signaling oligonucleotide hybridization and assembling two DNA hosts”. In: *Analytical chemistry* 86.18 (2014), pp. 9220–9228.

[44] Stacy M Copp et al. “Magic numbers in DNA-stabilized fluorescent silver clusters lead to magic colors”. In: *The journal of physical chemistry letters* 5.6 (2014), pp. 959–963.

[45] Martín I Taccone et al. “Optical properties and charge distribution in rod-shape DNA–silver cluster emitters”. In: *Physical Chemistry Chemical Physics* 20.35 (2018), pp. 22510–22516.

[46] Steven M Swasey et al. “Chiral electronic transitions in fluorescent silver clusters stabilized by DNA”. In: *ACS nano* 8.7 (2014), pp. 6883–6892.

[47] Jeffrey T Petty et al. “A silver cluster–DNA equilibrium”. In: *Analytical chemistry* 85.20 (2013), pp. 9868–9876.

[48] Ruslan R Ramazanov and Alexei I Kononov. “Excitation spectra argue for thread-like shape of DNA-stabilized silver fluorescent clusters”. In: *The Journal of Physical Chemistry C* 117.36 (2013), pp. 18681–18687.

[49] Víctor Soto-Verdugo, Horia Metiu, and Elisabeth Gwinn. “The properties of small Ag clusters bound to DNA bases”. In: *The Journal of chemical physics* 132.19 (2010), 05B606.

[50] Patrick R O’Neill, Elisabeth G Gwinn, and Deborah Kuchnir Fygenson. “UV excitation of DNA stabilized Ag cluster fluorescence via the DNA bases”. In: *The Journal of Physical Chemistry C* 115.49 (2011), pp. 24061–24066.

[51] Erling Thyrhaug et al. “Ultrafast coherence transfer in DNA-templated silver nanoclusters”. In: *Nature communications* 8.1 (2017), pp. 1–7.

[52] Matias Berdakin et al. “Disentangling the photophysics of DNA-stabilized silver nanocluster emitters”. In: *The Journal of Physical Chemistry C* 120.42 (2016), pp. 24409–24416.

[53] Jinbo Zhu et al. “G-quadruplex enhanced fluorescence of DNA–silver nanoclusters and their application in bioimaging”. In: *Nanoscale* 7.31 (2015), pp. 13224–13229.

[54] Junhua Yu et al. “Live cell surface labeling with fluorescent Ag nanocluster conjugates”. In: *Photochemistry and photobiology* 84.6 (2008), pp. 1435–1439.

[55] Sungmoon Choi et al. “Tailoring silver nanodots for intracellular staining”. In: *Photochemical & Photobiological Sciences* 10.1 (2011), pp. 109–115.

[56] Jing Wu et al. “DNA-stabilized silver nanoclusters for label-free fluorescence imaging of cell surface glycans and fluorescence guided photothermal therapy”. In: *Analytical chemistry* 90.24 (2018), pp. 14368–14375.

[57] Danya Lyu et al. “Cationic-Polyelectrolyte-Modified Fluorescent DNA–Silver Nanoclusters with Enhanced Emission and Higher Stability for Rapid Bioimaging”. In: *Analytical chemistry* 91.3 (2018), pp. 2050–2057.

[58] Yasuko Antoku et al. “Transfection of living HeLa cells with fluorescent poly-cytosine encapsulated Ag nanoclusters”. In: *Photochemical & Photobiological Sciences* 9.5 (2010), pp. 716–721.

[59] Raghu Kalluri and Valerie S LeBleu. “The biology, function, and biomedical applications of exosomes”. In: *Science* 367.6478 (2020).

[60] Akira Yokoi et al. “Mechanisms of nuclear content loading to exosomes”. In: *Science advances* 5.11 (2019), eaax8849.

[61] Olivier G de Jong et al. “A CRISPR-Cas9-based reporter system for single-cell detection of extracellular vesicle-mediated functional transfer of RNA”. In: *Nature communications* 11.1 (2020), pp. 1–13.

[62] Nunzio Iraci et al. “Extracellular vesicles are independent metabolic units with asparaginase activity”. In: *Nature chemical biology* 13.9 (2017), p. 951.

[63] Alexander G Thompson et al. “Extracellular vesicles in neurodegenerative disease—pathogenesis to biomarkers”. In: *Nature Reviews Neurology* 12.6 (2016), p. 346.

[64] Xiaoxue Zhou et al. “The function and clinical application of extracellular vesicles in innate immune regulation”. In: *Cellular & molecular immunology* 17.4 (2020), pp. 323–334.

[65] Pieter Vader et al. “Extracellular vesicles for drug delivery”. In: *Advanced drug delivery reviews* 106 (2016), pp. 148–156.

[66] Upendra Bulbake et al. “Liposomal formulations in clinical use: an updated review”. In: *Pharmaceutics* 9.2 (2017), p. 12.

[67] Lisa Sercombe et al. “Advances and challenges of liposome assisted drug delivery”. In: *Frontiers in pharmacology* 6 (2015), p. 286.

[68] Hwankyu Lee and Ronald G Larson. “Adsorption of plasma proteins onto PEGylated lipid bilayers: the effect of PEG size and grafting density”. In: *Biomacromolecules* 17.5 (2016), pp. 1757–1765.

[69] Bohdana M Discher et al. “Polymersomes: tough vesicles made from diblock copolymers”. In: *Science* 284.5417 (1999), pp. 1143–1146.

[70] Jiayu Leong et al. “Engineering polymersomes for diagnostics and therapy”. In: *Advanced healthcare materials* 7.8 (2018), p. 1701276.

[71] Jung Seok Lee and Jan Feijen. “Polymersomes for drug delivery: design, formation and characterization”. In: *Journal of controlled release* 161.2 (2012), pp. 473–483.

[72] René P Brinkhuis et al. “Size dependent biodistribution and SPECT imaging of 111In-labeled polymersomes”. In: *Bioconjugate chemistry* 23.5 (2012), pp. 958–965.

[73] Regina Bleul, Raphael Thiermann, and Michael Maskos. “Techniques to control polymersome size”. In: *Macromolecules* 48.20 (2015), pp. 7396–7409.

[74] James D Robertson et al. “Purification of nanoparticles by size and shape”. In: *Scientific reports* 6.1 (2016), pp. 1–9.

[75] Marko Kaksonen and Aurélien Roux. “Mechanisms of clathrin-mediated endocytosis”. In: *Nature reviews Molecular cell biology* 19.5 (2018), p. 313.

[76] Prasad V Pawar et al. “Functionalized polymersomes for biomedical applications”. In: *Polymer Chemistry* 4.11 (2013), pp. 3160–3176.

[77] Hailong Che and Jan CM van Hest. “Stimuli-responsive polymersomes and nanoreactors”. In: *Journal of Materials Chemistry B* 4.27 (2016), pp. 4632–4647.

[78] Fariyal Ahmed and Dennis E Discher. “Self-porating polymersomes of PEG–PLA and PEG–PCL: hydrolysis-triggered controlled release vesicles”. In: *Journal of controlled release* 96.1 (2004), pp. 37–53.

[79] Loredana Leggio et al. “Mastering the Tools: Natural versus Artificial Vesicles in Nanomedicine”. In: *Advanced healthcare materials* 9.18 (2020), p. 2000731.

[80] Marzia Massignani et al. “Enhanced fluorescence imaging of live cells by effective cytosolic delivery of probes”. In: *PLoS one* 5.5 (2010), e10459.

[81] Agnese Kocere et al. “Real-time imaging of polymersome nanoparticles in zebrafish embryos engrafted with melanoma cancer cells: Localization, toxicity and treatment analysis”. In: *EBioMedicine* 58 (2020), p. 102902.

[82] Marine Camblin et al. “Polymersomes containing quantum dots for cellular imaging”. In: *International journal of nanomedicine* 9 (2014), p. 2287.

[83] Carlos Lois and Arturo Alvarez-Buylla. “Long-distance neuronal migration in the adult mammalian brain”. In: *Science* 264.5162 (1994), pp. 1145–1148.

[84] J Tiago Gonçalves, Simon T Schafer, and Fred H Gage. “Adult neurogenesis in the hippocampus: from stem cells to behavior”. In: *Cell* 167.4 (2016), pp. 897–914.

[85] Kirsten Obernier and Arturo Alvarez-Buylla. “Neural stem cells: origin, heterogeneity and regulation in the adult mammalian brain”. In: *Development* 146.4 (2019).

[86] Verónica Martínez-Cerdeño and Stephen C Noctor. “Neural progenitor cell terminology”. In: *Frontiers in neuroanatomy* 12 (2018), p. 104.

[87] Alessandro Alunni and Laure Bally-Cuif. “A comparative view of regenerative neurogenesis in vertebrates”. In: *Development* 143.5 (2016), pp. 741–753.

[88] Olaf Bergmann, Kirsty L Spalding, and Jonas Frisén. “Adult neurogenesis in humans”. In: *Cold Spring Harbor perspectives in biology* 7.7 (2015), a018994.

[89] Aurélie Ernst et al. “Neurogenesis in the striatum of the adult human brain”. In: *Cell* 156.5 (2014), pp. 1072–1083.

[90] Katherine G Akers et al. “Hippocampal neurogenesis regulates forgetting during adulthood and infancy”. In: *Science* 344.6184 (2014), pp. 598–602.

[91] Christoph Anacker and René Hen. “Adult hippocampal neurogenesis and cognitive flexibility—linking memory and mood”. In: *Nature Reviews Neuroscience* 18.6 (2017), pp. 335–346.

[92] Fiona Doetsch and Arturo Alvarez-Buylla. “Network of tangential pathways for neuronal migration in adult mammalian brain”. In: *Proceedings of the National Academy of Sciences* 93.25 (1996), pp. 14895–14900.

[93] Wankun L Li et al. “Adult-born neurons facilitate olfactory bulb pattern separation during task engagement”. In: *Elife* 7 (2018), e33006.

[94] Anne Grelat et al. “Adult-born neurons boost odor–reward association”. In: *Proceedings of the National Academy of Sciences* 115.10 (2018), pp. 2514–2519.

[95] Mary C Whitman et al. “Blood vessels form a migratory scaffold in the rostral migratory stream”. In: *Journal of Comparative Neurology* 516.2 (2009), pp. 94–104.

[96] Woong Sun, Hyun Kim, and Younghye Moon. "Control of neuronal migration through rostral migration stream in mice." In: *Anatomy & cell biology* 43.4 (2010), pp. 269–279.

[97] Mayara Vieira Mundim et al. "A new function for Prokineticin 2: Recruitment of SVZ-derived neuroblasts to the injured cortex in a mouse model of traumatic brain injury". In: *Molecular and Cellular Neuroscience* 94 (2019), pp. 1–10.

[98] Takuro Kojima et al. "Subventricular zone-derived neural progenitor cells migrate along a blood vessel scaffold toward the post-stroke striatum". In: *Stem cells* 28.3 (2010), pp. 545–554.

[99] Toru Yamashita et al. "Subventricular zone-derived neuroblasts migrate and differentiate into mature neurons in the post-stroke adult striatum". In: *Journal of Neuroscience* 26.24 (2006), pp. 6627–6636.

[100] Shang-Wei Hou et al. "Functional integration of newly generated neurons into striatum after cerebral ischemia in the adult rat brain". In: *Stroke* 39.10 (2008), pp. 2837–2844.

[101] Naosuke Kamei et al. "BDNF, NT-3, and NGF released from transplanted neural progenitor cells promote corticospinal axon growth in organotypic cocultures". In: *Spine* 32.12 (2007), pp. 1272–1278.

[102] Samuel E Marsh and Mathew Blurton-Jones. "Neural stem cell therapy for neurodegenerative disorders: The role of neurotrophic support". In: *Neurochemistry international* 106 (2017), pp. 94–100.

[103] Cory M Willis et al. "The neural stem cell secretome and its role in brain repair". In: *Brain research* 1729 (2020), p. 146615.

[104] Jin-Jing Zhang et al. "Transplantation of bFGF-expressing neural stem cells promotes cell migration and functional recovery in rat brain after transient ischemic stroke". In: *Oncotarget* 8.60 (2017), p. 102067.

[105] Nathalie Picard-Riera, Brahim Nait-Oumesmar, and Anne Baron-Van Evercooren. "Endogenous adult neural stem cells: limits and potential to repair the injured central nervous system". In: *Journal of neuroscience research* 76.2 (2004), pp. 223–231.

[106] Hideyuki Okano et al. "Regeneration of the central nervous system using endogenous repair mechanisms". In: *Journal of neurochemistry* 102.5 (2007), pp. 1459–1465.

[107] Andreas Arvidsson et al. "Neuronal replacement from endogenous precursors in the adult brain after stroke". In: *Nature medicine* 8.9 (2002), pp. 963–970.

[108] Xuan Li et al. "Administration of signalling molecules dictates stem cell homing for in situ regeneration". In: *Journal of cellular and molecular medicine* 21.12 (2017), pp. 3162–3177.

[109] Matthew V Covey and Steven W Levison. "Leukemia inhibitory factor participates in the expansion of neural stem/progenitors after perinatal hypoxia/ischemia". In: *Neuroscience* 148.2 (2007), pp. 501–509.

[110] Sylvian Bauer and Paul H Patterson. “Leukemia inhibitory factor promotes neural stem cell self-renewal in the adult brain”. In: *Journal of Neuroscience* 26.46 (2006), pp. 12089–12099.

[111] Jaime Imitola et al. “Directed migration of neural stem cells to sites of CNS injury by the stromal cell-derived factor 1α/CXC chemokine receptor 4 pathway”. In: *Proceedings of the National Academy of Sciences* 101.52 (2004), pp. 18117–18122.

[112] Stephen E Kendall et al. “Neural stem cell targeting of glioma is dependent on phosphoinositide 3-kinase signaling”. In: *Stem cells* 26.6 (2008), pp. 1575–1586.

[113] Giulia Forotti et al. “CSF transplantation of a specific iPSC-derived neural stem cell subpopulation ameliorates the disease phenotype in a mouse model of spinal muscular atrophy with respiratory distress type 1”. In: *Experimental neurology* 321 (2019), p. 113041.

[114] Il-Shin Lee et al. “Human neural stem cells alleviate Alzheimer-like pathology in a mouse model”. In: *Molecular neurodegeneration* 10.1 (2015), pp. 1–16.

[115] Roberta De Gioia et al. “Neural Stem Cell Transplantation for Neurodegenerative Diseases”. In: *International journal of molecular sciences* 21.9 (2020), p. 3103.

[116] Naoko Kaneko, Masato Sawada, and Kazunobu Sawamoto. “Mechanisms of neuronal migration in the adult brain”. In: *Journal of neurochemistry* 141.6 (2017), pp. 835–847.

[117] Christiane L Mallett, Dorela D Shuboni-Mulligan, and Erik M Shapiro. “Tracking neural progenitor cell migration in the rodent brain using magnetic resonance imaging”. In: *Frontiers in neuroscience* 12 (2019), p. 995.

[118] Kapinga P Ngalula et al. “Transplanted neural progenitor cells from distinct sources migrate differentially in an organotypic model of brain injury”. In: *Frontiers in neurology* 6 (2015), p. 212.

[119] Dorela D Shuboni-Mulligan et al. “In vivo serial MRI of age-dependent neural progenitor cell migration in the rat brain”. In: *Neuroimage* 199 (2019), pp. 153–159.

[120] Felipe Ortega, Benedikt Berninger, and Marcos R Costa. “Primary culture and live imaging of adult neural stem cells and their progeny”. In: *Imaging and Tracking Stem Cells*. Springer, 2013, pp. 1–11.

[121] Marcos R Costa et al. “Continuous live imaging of adult neural stem cell division and lineage progression in vitro”. In: *Development* 138.6 (2011), pp. 1057–1068.

[122] Katja M Piltti et al. “Live-cell time-lapse imaging and single-cell tracking of in vitro cultured neural stem cells–Tools for analyzing dynamics of cell cycle, migration, and lineage selection”. In: *Methods* 133 (2018), pp. 81–90.

2

FLUORESCENCE-TUNABLE AG-DNA BIOSENSOR WITH TAILORED CYTOTOXICITY FOR LIVE-CELL APPLICATIONS

DNA-stabilized silver clusters (Ag-DNA) show excellent promise as a multifunctional nanoagent for molecular investigations in living cells. The unique properties of these fluorescent nanomaterials allow for intracellular optical sensors with tunable cytotoxicity based on simple modifications of the DNA sequences. Three Ag-DNA nanoagent designs are investigated, exhibiting optical responses to the intracellular environments and sensing-capability of ions, functional inside living cells. Their sequence-dependent fluorescence responses inside living cells include (1) a strong splitting of the fluorescence peak for a DNA hairpin construct, (2) an excitation and emission shift of up to 120 nm for a single-stranded DNA construct, and (3) a sequence robust in fluorescence properties. Additionally, the cytotoxicity of these Ag-DNA constructs is tunable, ranging from highly cytotoxic to biocompatible Ag-DNA, independent of their optical sensing capability. Thus, Ag-DNA represents a versatile live-cell nanoagent addressable towards anti-cancer, patient-specific and anti-bacterial applications.

.

This chapter is based on the publication: Bossert N., de Bruin D., Gotz M., Bouwmeester D., Heinrich D.: Fluorescence-tunable Ag-DNA Biosensor with tailored Cytotoxicity for Live-Cell Applications, Scientific Reports (6.1) (2016) 1-8

2.1. INTRODUCTION

DNA-encapsulated silver nanoclusters (Ag-DNA) have recently attracted much attention, as they exhibit numerous unique fluorescence properties, like high photostability, fluorescence quantum yields of up to 90% and tunable excitation and emission spectra [1–6]. The high sensitivity to their surroundings is one of the most intriguing properties of Ag-DNA nanoclusters, allowing them to exhibit an optical response due to enviro nmental changes: conformational changes of the DNA template lead to varying distances and interactions between DNA bases and silver clusters[7, 8].In solution, Ag-DNA have been shown to even respond to single-base mutations [9, 10], and to detect molecule concentrations down to 0.37 nm [11]. Therefore, Ag-DNA are very promising for intracellular bio-sensing applications and to investigate intracellular dynamics, as so far is done mostly with fluorescent nanobead probes [12–15]. Most fluorescent agents show functional limitations, like photobleaching or low absorption coefficients and often fulfill one function only. This makes the search for alternative nanomaterials an ongoing quest.

The encapsulated silver in Ag-DNA nanoagents further allow for multifunctional applications, as these optical sensors exhibit tunable degrees of cytotoxicity [16]. In the past years, silver has been increasingly used in cosmetics, clothes, implant coatings, and for burn wound dressings, to obtain an antibacterial effect [17–20]. Its inherent toxicity makes the metal a particularly promising alternative to antibiotics, as bacterial resistances rise [21, 22], as well as an anti-cancer agent [23–25]. However, the toxicity mechanism of silver is not yet clearly understood [26, 27]. As nano-sized silver is highly bioactive, its broad utilization bears a potential risk for humans ([28–30], making a more controlled and tunable way of its application appealing.

Furthermore, these fluorescent Ag-DNA nanomaterials are easily compatible with DNA nanotechnology and DNA origami, and provide an easy attachment site for specific addition of desired targets and recognition elements. This has been implemented for specific labeling of cellular membrane and nuclei ([31–34], using the Ag-DNA emitters as a replacement of an organic dye. So far, however, the optical sensor functionality, particularly in combination with independently tunable cytotoxicity of Ag-DNA constructs, has not been investigated in live-cell interiors.

Fluorescent Ag-DNA are synthesized upon reduction of silver ions by sodium borohydride ($NaBH_4$) in the presence of DNA (Figure 2.1), resulting in rod-shaped silver cores comprised of 4–12 neutral Ag atoms ([35, 36]. Remarkably, these nanomaterials can exhibit peak emission wavelengths across the visible and near-IR spectrum ([37] determined by the variant sizes and aspect ratios of the noble metal nanoclusters ([36]. Similar to larger noble metal nanoparticles, larger silver rods correspond to a longer wavelength resonance than smaller particles ([38–40], with the DNA template also playing a role in the fluorescence variance of the emitters.

Using these dependencies, we selected and optimized Ag-DNA templates to function as an optical sensor in living cells' interior enviro nments (Figure 2.1 b-d) (for DNA sequences please see section 2.4 Table 2.1). At the same time, by utilizing the endogenous silver core, we tuned Ag-DNA from cytotoxic to completely biocompatible (Figure 2.1b-d), creating an intracellular toxicity-tunable optical sensor. Here, we demonstrate the functionality of the designed nanoagents in a live-cell enviro nment.

2.2. RESULTS AND DISCUSSION

2.2.1. AG-DNA NANOAGENT DESIGN

The choice of DNA sequences is the result of optimizing fluorescence and/or sensor properties of Ag-DNA within the cell by varying the base sequences for enhanced performance. The strong interaction of cytosine and guanine bases with Ag(I)ions allows effective stabilization of a silver cluster. Furthermore, the addition of adenine and thymine bases throughout the DNA strand increase the yields of fluorescent species and fluorescence quantum yields. By varying the base sequences, the resulting different sizes and shapes of Ag-DNA structures define their particular functionality as nanoagents.

First, we demonstrate a robust and bright Ag-DNA structure, applicable as a fluorescent marker inside living cells. The DNA template, consisting of 28 single bases, yields an Ag-DNA construct (Ag-28b in Figure 2.1 b) with strong and stable fluorescence properties [35], which we show are retained upon insertion into living cells. Thus, in this DNA-design, the encapsulated silver cluster preserves its fluorescence properties when inside living cells, not reacting to the complex intracellular enviro nment.

While the relatively long single strand wrapping around the silver cluster seems to protect the cluster enough to maintain a strong fluorescence, any exposed parts of the silver surface could still interact with cellular molecules, altering cellular processes.

Small changes in the DNA template can have a significant effect on the functionality of the Ag-DNA nanomaterials. Here, we demonstrate that a simple modification of Ag-28b produces an Ag-DNA construct which shows optical sensor functionality inside living cells: shortening the 28b sequence by nine bases produces the Ag-19b construct [41] (Figure 2.1c), which exhibits an optical response to the intracellular enviro nment. By using the shorter sequence, we reduce the shielding of cellular molecules from the silver surface as compared to Ag-28b, resulting in a higher level of cytotoxicity and yielding a stronger sensitivity to the change in conditions inside living cells. To decrease the toxicity level to a biocompatible Ag-DNA for an optical biosensor sensitive to intracellular ions, we designed an Ag-hairpin (Ag-HP) construct (Figure 2.1 c), as DNA hairpins with Poly-C loops have been shown to stabilize strongly fluorescent Ag-DNA species [37]. As the molecular dynamics of single- and double-stranded DNA heavily depend on the presence of salts [42], DNA-ions interactions lead to conformational changes of the hairpin loop resulting in optical emission shifts inside living cells, yielding an optical sensor. The amount of cytosine bases in the loop, and the length and sequence of the double stranded stem were optimized for sensitivity. The Poly-C-loop wrapping around the silver cluster through strong Cytosine-Ag(I)ions interactions prevents the silver surface from interacting with cellular molecules, yielding a biocompatible construct.

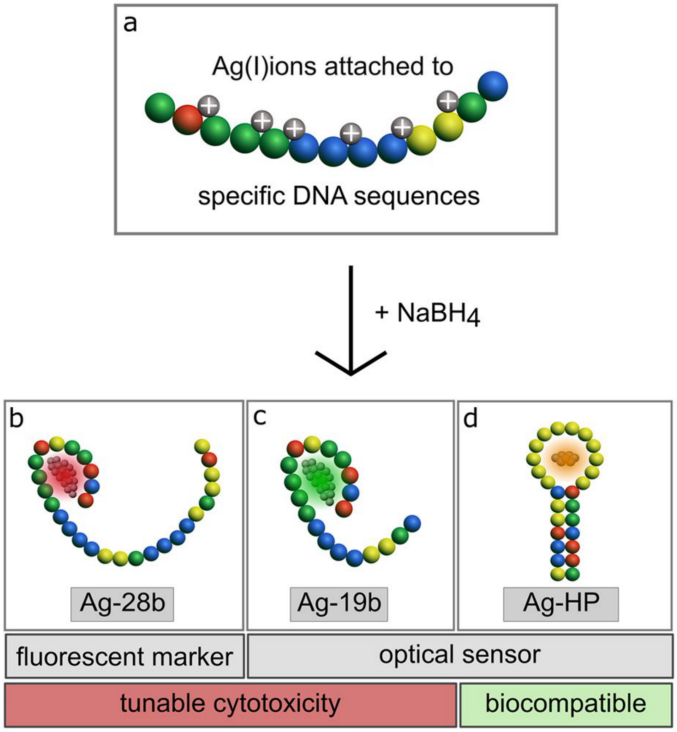

Figure 2.1: Schemes of general Ag-DNA synthesis (a) and specifically designed Ag-DNA constructs (b–d). Fluorescent Ag-DNA are synthesized upon reduction of silver ions by sodium borohydride ($NaBH_4$) in the presence of a specific DNA template. The designed Ag-DNA structures, utilized here, show different functionalities as a fluorescent marker or as an optical sensor, as well as exhibit tunable cytotoxicity or biocompatibility. DNA sequences color code are displayed for (b) Ag-28b, (c) Ag-19b and (d) Ag-HP by Cytosine=yellow, Guanine=green, Thymine=blue, Adenine=red.

2.2.2. FLUORESCENCE-TUNABLE PROPERTIES OF AG-DNA OPTICAL SENSORS

By acquiring the excitation and emission spectra, the fluorescence properties of the Ag-DNA structures were investigated in solution and in comparison in real cell environments (Figure 2.2 and 2.3). All three types of Ag-DNA were quickly internalized into living cells and showed a homogeneous distribution throughout the cytoplasm and the cell nucleus (section 2.4 Figure 2.5, negative control section 2.4 Figure 2.6).

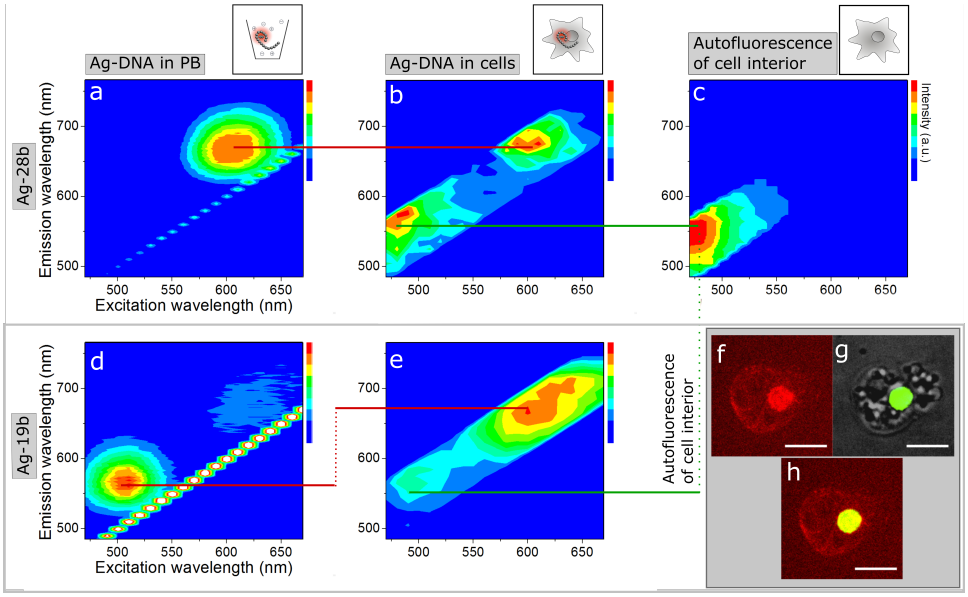

Figure 2.2: Fluorescence excitation/emission spectra of Ag-DNA nanoagents of type Ag-28b and Ag-19b, before (a,d) and after (b,e) internalization in D.*discoideum* wildtype cells. Fluorescence spectra are measured within the excitation range of 470–670 nm and the emission range of 490–760 nm, each in 10 nm steps. Ag-28b exhibits a fluorescence peak at $\lambda_{(ex)}$=605 nm/$\lambda_{(em)}$=665 nm in PB (a), which is preserved upon internalization in living cells (b) (illustrated by the red line). Without addition of Ag-DNA variants, cell interiors exhibit a peak at $\lambda_{(ex)}$=470 nm/$\lambda_{(em)}$=550 nm, corresponding to autofluorescence (c) (illustrated by the green lines). Ag-19b shows a dominant emitter at $\lambda_{(ex)}$=495 nm/$\lambda_{(em)}$=560 nm in PB (d). Upon internalization in living cells, the peak shifts to $\lambda_{(ex)}$=625 nm/$\lambda_{(em)}$=680 nm(e) yielding a shift of $\Delta\lambda_{(ex)}$=130 nm/$\Delta\lambda_{(em)}$=120 nm (illustrated by the red lines). The regions of interest (ROIs) for intracellular fluorescence spectra are displayed in section 2.4 Figure 2.7. Confocal fluorescence images display the accumulation of Ag-19b at cellular membranes and inside the cell nucleus (f). The nucleus is labeled by GFP-histone (green) (g) and nuclear localization is shown by the overlay (yellow) (h) of the Ag-19b signal (red) (f) with GFP-labeled histones. The scale bar is 10 μm.

In phosphate buffer (PB), Ag-28b exhibits a single fluorescence peak at $\lambda_{(ex)}$=605 nm/$\lambda_{(em)}$=665 nm (Figure 2.3 a). When exposing these Ag-DNA structures to the interior of a living cell, the fluorescence properties of Ag-28b are not influenced, as indicated by the red line in Figure 2.3 a,b. The second peak at $\lambda_{(ex)}$=470 nm/$\lambda_{(em)}$=550 nm arises from the autofluorescence of D.*discoideum* wildtype cells (Figure 2.3b,c) (indicated by the green line), as observed in all intracellular fluorescence spectra.

Shortening the DNA template reveals a significant effect on the enviro nmental sensing function of the Ag-DNA construct. Inside cells, Ag-19b show a significant fluorescence shift of $\Delta\lambda_{(ex)}$=130 nm/$\Delta\lambda_{(em)}$=120 nm (Figure 2.2d,e)(indicated by the red lines). This relocates the dominant peak observed in PB at $\lambda_{(ex)}$=495 nm/$\lambda_{(em)}$=560 nm to $\lambda_{(ex)}$ =625 nm/$\lambda_{(em)}$=680 nm in the living cell.

A fluorescence peak in this wavelength range is typically exhibited by Ag-DNA with DNA strands longer than 19 bases, such as in Ag-28b, which stabilize larger silver clusters. Hence, these larger clusters likely require higher molecular stability to reach the fluorescent state, which can be provided by the interactions of Ag-19b with the nuclear

DNA, as well as relatively dense cellular structures like membrane proteins and lipids. Accumulation of Ag-19b in these cellular regions was observed, as shown in Figure 2.2 f-h.

The hairpin structure (Ag-HP) was designed as a biosensor specific to intracellular ions. When in PB, Ag-HP emits at $\lambda_{(ex)}$=540 nm/$\lambda_{(em)}$=590 nm (Figure 2.3 a). Upon internalization by cells, its fluorescence properties show a split into two peaks. The previously observed peak is largely retained. Additionally, a second peak is observed at $\lambda_{(ex)}$=580 nm/$\lambda_{(em)}$=650 nm, thus providing a shift in emission of $\Delta\lambda_{(ex)}$=60 nm (Figure 2.3 a,b) (indicated by the red lines).

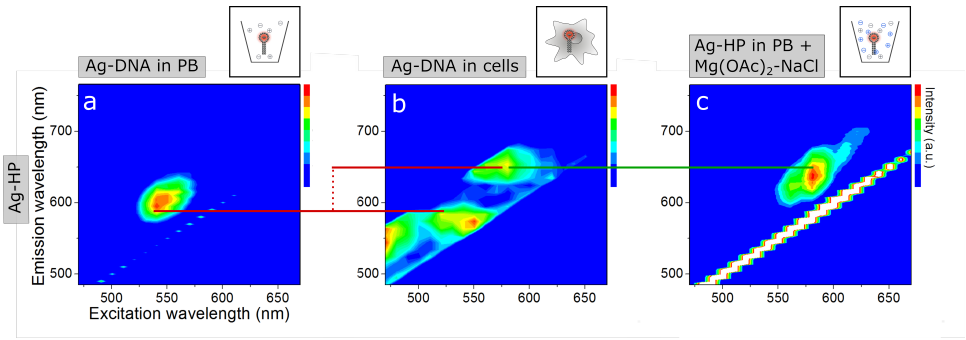

Figure 2.3: Fluorescence excitation/emission spectra of Ag-HP before (a) and after (b) internalization in D.*discoideum* wildtype cells, and in presence of specific ions (c). Fluorescence spectra were measured within the excitation range of 470–670 nm and the emission range of 490–760 nm, each in 10 nm steps. In PB, Ag-HP exhibits a peak at $\lambda_{(ex)}$=540 nm/$\lambda_{(em)}$=590 nm (a). Upon internalization in cells, a split into a second peak at $\lambda_{(ex)}$=580 nm/$\lambda_{(em)}$=650 nm occurs, yielding a shift of $\Delta\lambda_{(ex)}$=40 nm/$\Delta\lambda_{(em)}$=60 nm, whereas the first peak is mainly preserved (illustrated by the red lines) (b). Addition of 40mM $Mg(OAc)_2$ and 30mM NaCl reproduces the red-shifted peak at $\lambda_{(ex)}$=580 nm/$\lambda_{(em)}$=640 nm observed only inside cells (illustrated by the green line), yet not the peak in PB (c). The regions of interest (ROIs) for intracellular fluorescence spectra are displayed in Figure 2.7.

To confirm the role of ions in the observed red-shifted fluorescence peak, we exposed Ag-HP to various salt types and concentrations in PB. By the addition of 40 mM $Mg(OAc)_2$ in combination with 30 mM NaCl (Figure 2.3 c), the red-shifted intensity distribution near $\lambda_{(ex)}$=580 nm/$\lambda_{(em)}$=650 nm, as observed inside living cells in Figure 2.3b, was reproduced (Figure 2.3 b,c) (indicated by the green line). Exposing Ag-HPs only to monovalent (Na^+) or only to divalent (Mg^{2+}) cations did not reproduce the spectrum in Figure 2.3 b. Cations in particular reduce the flexibility of double stranded DNA, and can induce a conformational change, depending on the type of cations bound [43]. In high salt conditions, even chloride anions have been suggested to localize on parts of the DNA surface, as well as in the grooves [44]. We observed that the addition of chloride anions was necessary for reproducing the shift of the peak in PB to higher wavelengths, that was measured in living cells, in $Mg(OAc)_2$-NaCl. Noble metal nanoparticles and clusters are known to exhibit sensitivity to their enviro nment, like the dielectric constant of a medium, as is reflected by changes in their plasmonic resonance [39]. However, for small particles these effects typically lead to relatively small shifts in resonance [40],

which has been demonstrated recently for purified, individual Ag-DNA species, leading to an absorption shift of up to 8 nm [36].

Here, we utilize the fact that synthesis of Ag-DNA yields a heterogeneous distribution of different Ag cluster sizes and DNA conformations [45]. After synthesis, the formed silver nanoclusters can occur in a fluorescent or a dark state [45]. Hence, we attribute the observed optical shifts to rearrangements in switching these optically different emitters 'on' or 'off', resulting from conformational changes of the DNA template. This way we facilitate much larger shifts of up to $\Delta\lambda_{(ex)}$=120 nm, which allow the varying responses of Ag-19b and Ag-HP to be easily separated and identified by conventional microscopy methods. In particular, DNA hairpin structures have been shown to typically stabilize a broader range of active fluorescent emitters than the single stranded variants [46], making them very suitable for biosensing applications.

2.2.3. TUNABLE CYTOTOXICITY OF AG-DNA

In addition to this biosensing functionality, we utilize the toxicity effect of endogenous silver clusters in Ag-DNA for live-cell applications. We show the tunability of cytotoxicity in Ag-DNA, which is controlled independently of the optical sensor ability of the Ag-DNA constructs.

In the cytotoxicity experiment, 100% cell viability corresponds to control experiments with cells not exposed to Ag-DNA or $AgNO_3$ agents under the same conditions. Figure 2.4 displays the concentration-dependent toxicity of Ag-28b, Ag-19b, and Ag-HP on D.*discoideum* wildtype cells, with exposures ranging between 75 nm and 36 μM. Ag-HP exhibit biocompatibility, with cell viabilities within 80–100% at all concentrations. When incubated with Ag-19b and Ag-28b, cell survival was increasingly impaired with rising Ag-DNA concentrations. For Ag-28b a slight decrease in cell viability was observed, with over 60% viable cells at 36 μM. Ag-19b had the strongest negative effect on cell survival, still yielding 30% of living cells at the highest concentration. As a reference measurement for cytotoxicity we used $AgNO_3$, which readily releases free Ag(I)ions in solution. This resulted in the highest cytotoxic effect for the same concentration of silver, as compared to the DNA-stabilized silver clusters.

To exclude other sources for cytotoxicity beside Ag-DNA, the following steps were taken. We removed potentially harmful byproducts or educts possibly causing toxicity by filtration of the synthesized Ag-DNA. Also we confirmed experimentally that a toxic effect caused by oligonucleotides is unlikely. Furthermore, for the cytotoxicity experiments, incubation steps and subsequent cell viability assays were performed in the dark, to exclude possible light-induced toxicity, like ROS generation. These points allow us to identify the silver in the Ag-DNA constructs as the only significant source of cytotoxicity, which is supported by the biocompatibility of Ag-HP.

We conclude from these results that the DNA templates can protect cells from silver and the selected DNA-sequence determines the toxic effect, ranging from non-toxic for Ag-HP to highly toxic for Ag-19b. This mechanism of protection results from distinct interactions of silver with DNA bases and the steric conditions of the Ag-DNA, varying the degree of silver exposure to cellular structures. Due to high binding energies of silver clusters to cytosine and guanine bases, which are several times stronger than Watson-

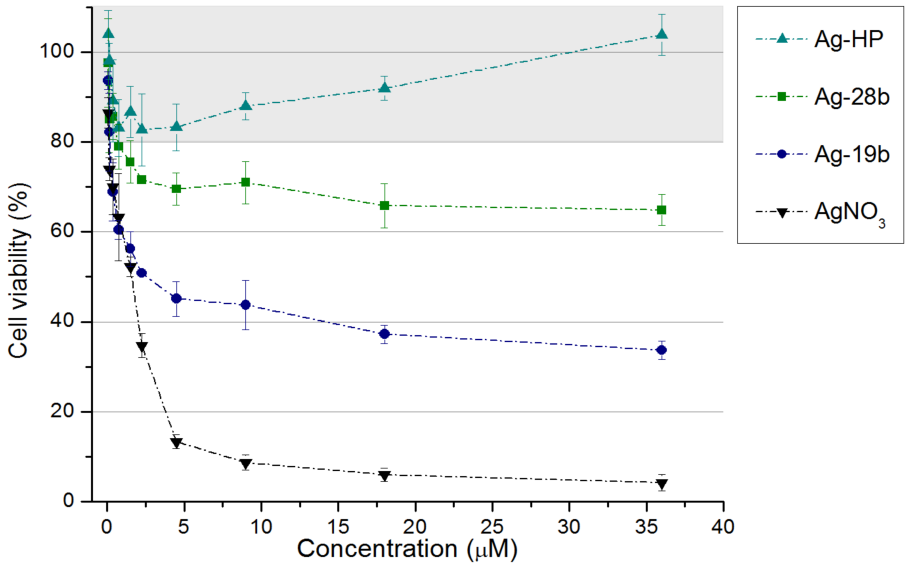

Figure 2.4: The number of living cells was quantified by incubation with Fluorescein diacetate and measuring the average fluorescence intensity. Cell viability of 100% was defined by a control incubated simultaneously without addition of any agents.Data shown represents the mean ± standard deviation (n=3).

Crick base pairs [46], we can assume that the silver clusters mainly remain contained in the Ag-DNA structures. Hence, the observed cytotoxicity effect of single stranded Ag-DNA nanomaterials most likely results from direct contact of cellular structures and molecules with exposed areas of the silver clusters as well as possibly released individual Ag(I)ions.

In Ag-HP, the silver cluster is surrounded by a Poly-C loop. As guanine and cytosine bases in particular show a high affinity to Ag(I)ions [45, 47], multiple Ag(I)ions-DNA base connections are formed which lead to a strongly shielded silver cluster, allowing for a decrease in Ag-DNA cytotoxicity. Both Ag-28b and Ag-19b constructs are single stranded DNA templates, which are expected to wrap around the silver cluster upon reduction with $NaBH_4$, due to Ag(I)ions-base bonding. The sequences in Ag-28b and Ag-19b lack the high density of cytosines of the Poly-C loop in Ag-HP, hence a larger area of the silver nanocluster is exposed in Ag-28b and Ag-19b, which can interact with surrounding molecules and impact cellular processes. Since Ag-28b provides a higher amount of cytosine and guanine bases, and additionally, its longer strand offers the possibility of a more stable Ag-DNA conformation, it yields a lower cytotoxicity than its shorter counterpart Ag-19b. In these three variants, we show the potential for cytotoxicity tuning by adapting the cytosine and guanine amount and location in the implemented DNA template.

2.2.4. CONCLUSIONS

In conclusion, we show that the unique properties of Ag-DNA allow for nanomaterials with multiple functionalities, targeted at optical sensing in combination with tunable cytotoxicity, by simple modifications of Ag-DNA designs. Ag-28b exhibits stable fluorescence properties and is thus suitable for bright and persistent labeling of cells, as well as localization experiments. Its shorter counterpart, Ag-19b, is enviro nmentally sensitive with an optical emission shift of $\Delta\lambda_{(em)}$=120 nm and exhibits higher cytotoxicity, making it interesting as an anti-bacterial or anti-cancer agent. The biocompatible, non-toxic Ag-HP optically responds to intracellular salt concentrations, visible as a large fluorescence shift of about $\Delta\lambda_{(em)}$=60 nm, which allows a convenient detection of signal changes for both, Ag-HP and Ag-19b, by commonly used fluorescence microscope systems.

These results will allow us to extend these Ag-DNA constructs to more complex DNA-origami structures, and the investigations from single cells to living organisms. Therefore, Ag-DNA represent a new nanomaterial with high potential for a multi-functional nanoagent, combining bio-sensing and effector functionality. Possible targeted DNA-sequence specific applications would open a large field of patient-specific treatment including cancer or rare and degenerative diseases, as well as specific antimicrobial targeting.

2.3. MATERIALS AND METHODS

2.3.1. CHEMICALS

DNA strands 5'-CAC CGC TTT TGC CTT TTG GGG ACG GAT A-3'(28b), 5'-TGC CTT TTG GGG ACG GAT A-3'(19b), and (b) 5'-CT TAC CTC CCC CCC CCC CCA GGT AAG-3'(HP) with standard desalting (Integrated DNA Technologies, USA), AgNO3 (99.9999%, Sigma Aldrich, The Netherlands), NH4OAc (99.99%, Sigma Aldrich, The Netherlands) $NaBH_4$ (99%, Sigma Aldrich, The Netherlands), KH_2PO_4 (>99%, Sigma Aldrich, The Netherlands), Na^2HPO_4 (>99%, Sigma Aldrich, The Netherlands), Maltose (Duchefa Biochemie B. V., Netherlands), Fluorescein diacetate (F7378, Sigma Aldrich Merck, Germany), HL5-C medium (Formedium™, United Kingdom), NaCl (Fisher Scientific Company LLC, USA), $Mg(OAc)_2$ (>99%, Sigma Aldrich, The Netherlands), Geneticin (Sigma Aldrich, The Netherlands), 3kDa and 50kDa centrifugal filter (Merck Millipore, Germany) were used as received without further purification. Bi-distilled water from a Millipore system (Milli-Q Academic A-10, Merck Millipore Germany) was used for all solutions.

2.3.2. AG-DNA PREPARATION

For synthesis of (a) Ag-28b and Ag19b, and (b) Ag-HP solutions, 50 nmol of the respective DNA molecules were mixed with $AgNO_3$ in a ratio of (a) 9.6 : 1 silver ions: DNA strands, or (b) 7: 1 silver ions: DNA strands in 1ml 20 mM NH_4OAc. The solutions were incubated for 30min at 4° C and then reduced with $NaBH_4$ at 4° C over night. The reduction ratios were (a) 0.5: 1 and (b) 0.3: 1 $NaBH_4$: Ag^+. To exclude formed silver clumps and unbound Ag(I) ions as well as other salts, Ag-DNA constructs were filtered using

a 3kDa centrifugal filter and subsequently a 50kDa centrifugal filter, simultaneously exchanging the buffer with phosphate buffer (PB; 3.57mM KH_2PO_4, 3.46mM Na^2HPO_4, pH 6.0). The concentration of the DNA was calculated based on the absorption at 260 nm, measured with a Cary 50 UV-Vis spectrophotometer (Varian Medical Systems, Netherlands). For the reproduction of the observed peaks, various concentrations of $Mg(OAc)_2$ and NaCl were added to a 15 μM solution of Ag-HP in PB and the fluorescence properties measured. The excitation and emission properties of the Ag-DNA in PB were determined by Cary Eclipse fluorimeter (Varian Medical Systems, Netherlands.

2.3.3. CELL CULTURE

Dictyostelium *discoideum* HG1729 histone-GFP in AX2 and Dictyostelium *discoideum* Wildtype in AX2 cells were cultured in HL5-C medium adjusted to pH 6.7 at 21° C; medium for HG1729 histone-GFP was supplemented with 10 μg/ml Geneticin. For the experiments the cells were harvested below a confluency of 40% and washed three times with PB by centrifugation at 400 g for 5 min. Subsequently, cells dispersed in PB were seeded onto an observation chamber (composed of a cover glass and a custom-made Teflon® frame) and rested for 30 min, allowing the cells to settle down.

2.3.4. MICROSCOPY

Imaging of cells incubated with Ag-DNA was performed by confocal microscopy setup equipped with a Yokogawa 10,000 rpm spinning disc unit (Andor Technology Ltd., UK), Eclipse TiE Nikon inverted microscope (Nikon Corporation, Japan) and an IXON Ultra EMCCD camera (Andor Technology Ltd., UK). Ag-28b and Ag-19b were added to D. *discoideum* HG1729 histone-GFP cells to an end concentration of 4.5 μM and 3 μM, respectively, in an observation chamber and immediately imaged with a 100x oil immersion objective with NA 1.45. Ag-28b and Ag-19b were excited at 640 nm, histone GFP at 480 nm. As negative controls, also cells without Ag-DNA were imaged, as well as cells incubated in 36μM $AgNO_3$ and 4.5μM 28b-DNA, separately and mixed. Local fluorescence spectra measurements were performed with a Leica TCS SP8 STED 3X Microscope and with a 63x objective lens (Leica Microsystems, Germany), additionally equipped with HyD detectors (Leica Microsystems, Germany). The excitation wavelengths ranged from 470 to 670 nm in 10 nm steps and the emission wavelengths ranged from 480 to 770 nm, with a step size of 10 nm and a detection window of 10 nm. For this assay, solutions of Ag-28b (4.5 μM), Ag-19b (3 μM) and Ag-HP (15 μM) were incubated with D. *discoideum* wildtype cells.

2.3.5. CYTOTOXICITY ASSAY

D. *discoideum* wildtype cells were harvested and washed three times with a maltose-loaded phosphate buffer (3.57 mM KH_2PO_4, 3.46 mM Na^2HPO_4, 52.58 mM Maltose, pH 6.70) by centrifugation at 400 g for 4 min. Cells were incubated for 2 h with Ag-28b, Ag-19b and Ag-HP, with concentrations ranging between 75 nm and 36μM, as triplicates with 25000 cells/condition in the dark. As a positive control, incubation with $AgNO_3$ was

performed under the same conditions, as well as a negative control without agent incubation. To determine cell viability, cells were incubated with 50μg/ml Fluorescein diacetate for 15 min, and the average fluorescence intensity was measured using a TECAN Infinite M200 well plate reader (Tecan Trading AG, Switzerland). To avoid background fluorescence from the Ag-DNA, 50 mM NaCl was introduced to all samples prior to measurements.

2.4. ADDITIONAL INFORMATION

In this section additional information and figures are displayed that support the data presented in this chapter.

Table 2.1: DNA sequences used for Ag-DNA synthesis.

DNA sequence	Abbreviation
5'-CAC CGC TTT TGC CTT TTG GGG ACG GAT A-3'	28b
5'-TGC CTT TTG GGG ACG GAT A-3'	19b
5'-CT TAC CTC CCC CCC CCC CCA GGT AAG-3'	HP

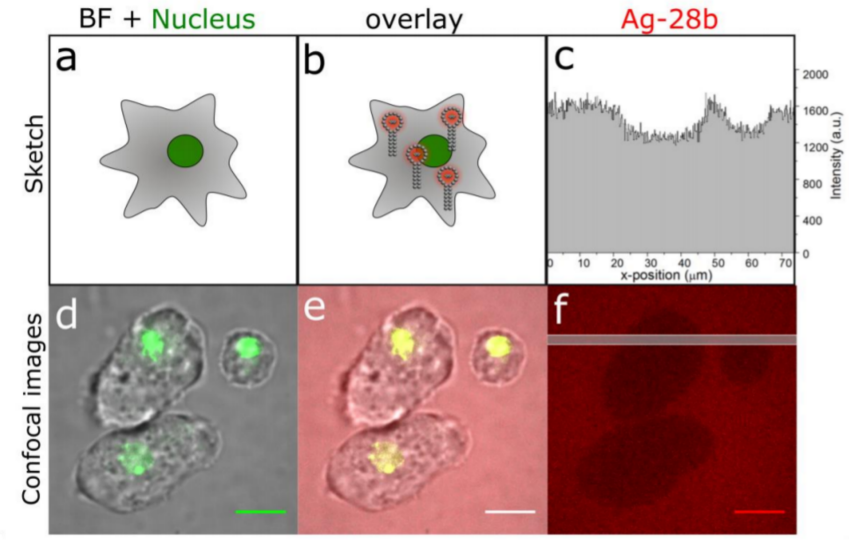

Figure 2.5: Internalization and distribution of Ag-28b inside D. *discoideum* cells. Overlay of brightfield images of cells with labeled GFP histones (green), showing the cell nucleus (a, d) (excitation at 488 nm), and including Ag-28b fluorescence (b, e) (excitation at 640 nm). Profile of the mean fluorescence intensity of Ag-28b (c) for positions along the grey line in the image of red Ag-28b fluorescence (f), showing about 80% of the intensity from the surrounding medium at positions corresponding to the cell interior. The scale bars are 10 μm.

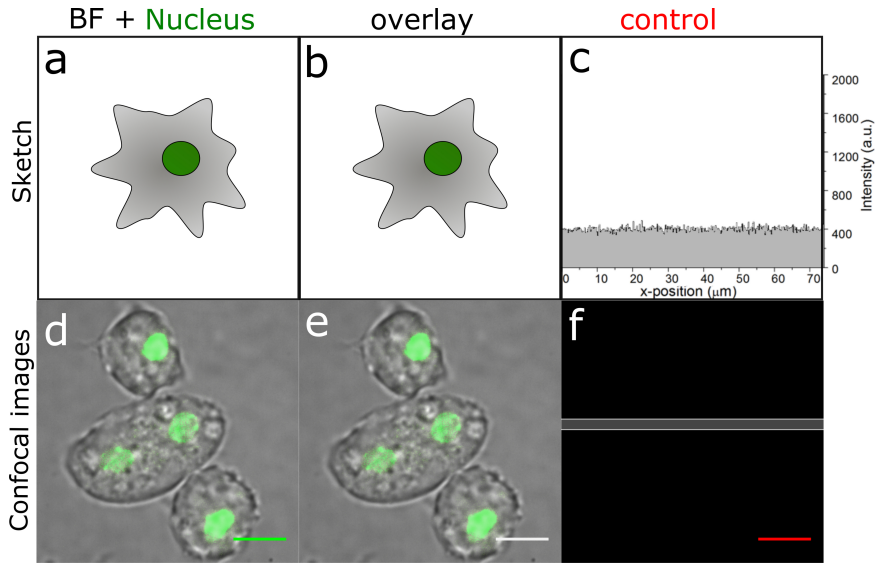

Figure 2.6: Negative control for the internalization and distribution of Ag-28b inside D. *discoideum* cells in Figure 2.5. Overlay of brightfield images of cells with labeled GFP histones, showing the cell nucleus (a, d) (excitation at 488 nm), and including any red autofluorescence (b, e) (excitation at 488 nm and 640 nm). Profile of the mean fluorescence intensity at 640 nm excitation (c) for positions along the grey line in the image of only the red channel (f). This control shows that there is only slight autofluorescence (e) when excited at 640 nm compared to the strong signal when employing Ag-28b as in 2.5 e. The scale bars are 10 μm.

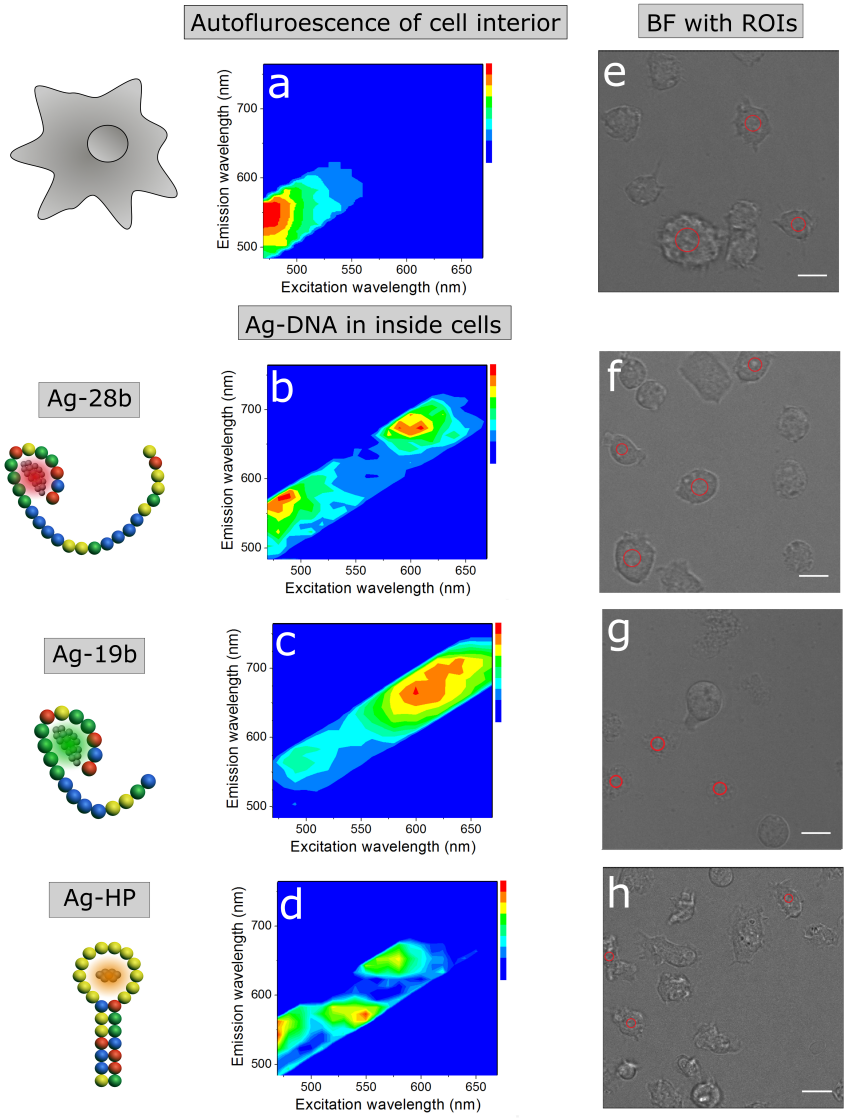

Figure 2.7: Region of interest (ROI) selection (e-h) for the fluorescence spectra analysis of Ag-DNA variants after internalization inD. *discoideum* wildtype cells (a-d). The 1st column shows sketches of used Ag-DNAs. DNA sequence color code: Cytosine = yellow, Guanine = green, Thymine = blue, Adenine = red. The spectra correspond to the fluorescence collected from the ROIs designated by red circles in the microscopy images. Fluorescence spectra were measured within excitation range of 470-670 nm and emission range of 490-760 nm, each in 10 nm steps. ROIs were chosen to remain entirely within the center of the cell throughout the measurement to avoid collection of light from the surrounding medium. The scale bars are 10 μm.

2.5. REFERENCES

[1] Jaswinder Sharma et al. “Silver nanocluster aptamers: in situ generation of intrinsically fluorescent recognition ligands for protein detection”. In: *Chemical Communications* 47.8 (2011), pp. 2294–2296.

[2] Bidisha Sengupta et al. “DNA templates for fluorescent silver clusters and i-motif folding”. In: *The Journal of Physical Chemistry C* 113.45 (2009), pp. 19518–19524.

[3] Chris I Richards et al. “Oligonucleotide-stabilized Ag nanocluster fluorophores”. In: *Journal of the American Chemical Society* 130.15 (2008), pp. 5038–5039.

[4] Tom Vosch et al. “Strongly emissive individual DNA-encapsulated Ag nanoclusters as single-molecule fluorophores”. In: *Proceedings of the National Academy of Sciences* 104.31 (2007), pp. 12616–12621.

[5] Danielle Schultz et al. “Dual-color nanoscale assemblies of structurally stable, few-atom silver clusters, as reported by fluorescence resonance energy transfer”. In: *ACS nano* 7.11 (2013), pp. 9798–9807.

[6] Bidisha Sengupta et al. “Base-directed formation of fluorescent silver clusters”. In: *The Journal of Physical Chemistry C* 112.48 (2008), pp. 18776–18782.

[7] Til Driehorst et al. “Distinct conformations of DNA-stabilized fluorescent silver nanoclusters revealed by electrophoretic mobility and diffusivity measurements”. In: *Langmuir* 27.14 (2011), pp. 8923–8933.

[8] Hsin-Chih Yeh et al. “A DNA- silver nanocluster probe that fluoresces upon hybridization”. In: *Nano letters* 10.8 (2010), pp. 3106–3110.

[9] Hsin-Chih Yeh et al. “A fluorescence light-up Ag nanocluster probe that discriminates single-nucleotide variants by emission color”. In: *Journal of the American Chemical Society* 134.28 (2012), pp. 11550–11558.

[10] Weiwei Guo et al. “Highly sequence-dependent formation of fluorescent silver nanoclusters in hybridized DNA duplexes for single nucleotide mutation identification”. In: *Journal of the American Chemical Society* 132.3 (2010), pp. 932–934.

[11] Jing-Jing Liu et al. “Label-free and fluorescence turn-on aptasensor for protein detection via target-induced silver nanoclusters formation”. In: *Analytica chimica acta* 749 (2012), pp. 70–74.

[12] Delphine Arcizet et al. “Temporal analysis of active and passive transport in living cells”. In: *Physical review letters* 101.24 (2008), p. 248103.

[13] M Götz et al. “Probing cytoskeleton dynamics by intracellular particle transport analysis”. In: *The European Physical Journal Special Topics* 224.7 (2015), pp. 1169–1183.

[14] Marcus Otten et al. “Local motion analysis reveals impact of the dynamic cytoskeleton on intracellular subdiffusion”. In: *Biophysical journal* 102.4 (2012), pp. 758–767.

[15] Carina Pelzl et al. “Axonal guidance by surface microstructuring for intracellular transport investigations”. In: *Chemphyschem* 10.16 (2009), pp. 2884–2890.

[16] Jaswinder Sharma et al. “A DNA-templated fluorescent silver nanocluster with enhanced stability”. In: *Nanoscale* 4.14 (2012), pp. 4107–4110.

[17] Richard Kuehl et al. “Preventing implant-associated infections by silver coating”. In: *Antimicrobial agents and chemotherapy* 60.4 (2016), pp. 2467–2475.

[18] Sogol Asghari, Sarvesh Logsetty, and Song Liu. “Imparting commercial antimicrobial dressings with low-adherence to burn wounds”. In: *Burns* 42.4 (2016), pp. 877–883.

[19] Fenella D Halstead et al. “Antimicrobial dressings: Comparison of the ability of a panel of dressings to prevent biofilm formation by key burn wound pathogens”. In: *Burns* 41.8 (2015), pp. 1683–1694.

[20] Svitlana Chernousova and Matthias Epple. “Silver as antibacterial agent: ion, nanoparticle, and metal”. In: *Angewandte Chemie International Edition* 52.6 (2013), pp. 1636–1653.

[21] A Kedziora et al. “Silver nanoforms as a therapeutic agent for killing Escherichia coli and certain ESKAPE pathogens”. In: *Current microbiology* 73.1 (2016), pp. 139–147.

[22] MA Radzig et al. “Antibacterial effects of silver nanoparticles on gram-negative bacteria: influence on the growth and biofilms formation, mechanisms of action”. In: *Colloids and Surfaces B: Biointerfaces* 102 (2013), pp. 300–306.

[23] Samad Mussa Farkhani et al. “Enhancing antitumor activity of silver nanoparticles by modification with cell-penetrating peptides”. In: *Artificial cells, nanomedicine, and biotechnology* 45.5 (2017), pp. 1029–1035.

[24] Pallab Sanpui, Arun Chattopadhyay, and Siddhartha Sankar Ghosh. “Induction of apoptosis in cancer cells at low silver nanoparticle concentrations using chitosan nanocarrier”. In: *ACS applied materials & interfaces* 3.2 (2011), pp. 218–228.

[25] Muthuraman Pandurangan et al. “Time and concentration-dependent therapeutic potential of silver nanoparticles in cervical carcinoma cells”. In: *Biological trace element research* 170.2 (2016), pp. 309–319.

[26] Bin-Hsu Mao et al. “Mechanisms of silver nanoparticle-induced toxicity and important role of autophagy”. In: *Nanotoxicology* 10.8 (2016), pp. 1021–1040.

[27] Yan Li et al. “Differential genotoxicity mechanisms of silver nanoparticles and silver ions”. In: *Archives of toxicology* 91.1 (2017), pp. 509–519.

[28] Esther E Fröhlich and Eleonore Fröhlich. “Cytotoxicity of nanoparticles contained in food on intestinal cells and the gut microbiota”. In: *International journal of molecular sciences* 17.4 (2016), p. 509.

[29] Anastasia Georgantzopoulou et al. “Effects of silver nanoparticles and ions on a co-culture model for the gastrointestinal epithelium”. In: *Particle and fibre toxicology* 13.1 (2015), pp. 1–17.

[30] Ivana Vinković Vrček et al. “Comparison of in vitro toxicity of silver ions and silver nanoparticles on human hepatoma cells”. In: *Environmental toxicology* 31.6 (2016), pp. 679–692.

[31] Jinjin Yin et al. “One-step engineering of silver nanoclusters–aptamer assemblies as luminescent labels to target tumor cells”. In: *Nanoscale* 4.1 (2012), pp. 110–112.

[32] Zhipeng Sun et al. “Ag cluster–aptamer hybrid: specifically marking the nucleus of live cells”. In: *Chemical Communications* 47.43 (2011), pp. 11960–11962.

[33] Junhua Yu et al. “Live cell surface labeling with fluorescent Ag nanocluster conjugates”. In: *Photochemistry and photobiology* 84.6 (2008), pp. 1435–1439.

[34] Jingjing Li et al. “Binding-induced fluorescence turn-on assay using aptamer-functionalized silver nanocluster DNA probes”. In: *Analytical chemistry* 84.12 (2012), pp. 5170–5174.

[35] Danielle Schultz et al. “Evidence for rod-shaped DNA-stabilized silver nanocluster emitters”. In: *Advanced materials* 25.20 (2013), pp. 2797–2803.

[36] Stacy M Copp et al. “Cluster plasmonics: dielectric and shape effects on DNA-stabilized silver clusters”. In: *Nano letters* 16.6 (2016), pp. 3594–3599.

[37] Patrick R O’Neill et al. “Hairpins with poly-C loops stabilize four types of fluorescent Ag n: DNA”. In: *The Journal of Physical Chemistry C* 113.11 (2009), pp. 4229–4233.

[38] K Lance Kelly et al. *The optical properties of metal nanoparticles: the influence of size, shape, and dielectric environment*. 2003.

[39] Huanjun Chen et al. “Shape-and size-dependent refractive index sensitivity of gold nanoparticles”. In: *Langmuir* 24.10 (2008), pp. 5233–5237.

[40] Danielle Schultz and Elisabeth Gwinn. “Stabilization of fluorescent silver clusters by RNA homopolymers and their DNA analogs: C, G versus A, T (U) dichotomy”. In: *Chemical communications* 47.16 (2011), pp. 4715–4717.

[41] Danielle Schultz and Elisabeth G Gwinn. “Silver atom and strand numbers in fluorescent and dark Ag: DNAs”. In: *Chemical Communications* 48.46 (2012), pp. 5748–5750.

[42] Vladimir P Denisov and Bertil Halle. “Sequence-specific binding of counterions to B-DNA”. In: *Proceedings of the National Academy of Sciences* 97.2 (2000), pp. 629–633.

[43] Péter Várnai and Krystyna Zakrzewska. “DNA and its counterions: a molecular dynamics study”. In: *Nucleic acids research* 32.14 (2004), pp. 4269–4280.

[44] OO Liubysh, AV Vlasiuk, and SM Perepelytsya. “Structuring of counterions around DNA double helix: a molecular dynamics study”. In: *arXiv preprint arXiv:1503.05334* (2015).

[45] Elisabeth G Gwinn et al. “Sequence-Dependent fluorescence of DNA-Hosted silver nanoclusters”. In: *Advanced Materials* 20.2 (2008), pp. 279–283.

[46] Steven M Swasey et al. “Silver (I) as DNA glue: Ag+-mediated guanine pairing revealed by removing Watson-Crick constraints”. In: *Scientific reports* 5.1 (2015), pp. 1–9.

[47] Hidetaka Torigoe et al. “Thermodynamic and structural properties of the specific binding between Ag+ ion and C: C mismatched base pair in duplex DNA to form C–Ag–C metal-mediated base pair”. In: *Biochimie* 94.11 (2012), pp. 2431–2440.

3

FLUORESCENT POLYMERSOMES IN LIVING CELLS

Fluorescent nanoparticles are becoming a broadly used tool in bio-imaging and medical research. Here, the intracellular fate of novel dual-fluorescent polyisobutylene-polyethylene glycol (PiB-PEG) polymersomes was investigated using confocal microscopy. Short-interval time-lapse imaging visualized fast endocytosis of the nanovesicles by A549 lung carcinoma cells and an active transport within the endolysosomal network. Long-term time-lapse imaging showed that the polymersomes remained intact and fluorescent for at least 90h and were approximately equal distributed during mitosis. The cells were followed for up to 11 days confirming the biocompatibility of the polymersomes and showing their full degradation between day 7 to 11.

This chapter is based on the publication: S.H.C. Askes, N. Bossert, J. Bussmann, V. Saez Talens, M.S., Meijer, R. E. Kieltyka, A. Kros, S. Bonnet, D. Heinrich, Dynamics of dual-fluorescent polymersomes with durable integrity in living cancer cells and zebrafish embryos, Biomaterials (168) (2018) 54-63. Here we focus on the results obtained by optical imaging.

3.1. INTRODUCTION

Over the last decades, fluorescence imaging and functionalized nanomaterials became crucial tools in the fields of biological and medical research [1, 2]. For acquisition of good imaging data and low phototoxicity, suitable equipment along with appropriate fluorescent materials are required [3]. The employed fluorescent materials need to fulfill a range of criteria, including easy uptake by cells and biocompatibility, high signal intensity and high resistance; particularly when detection over a prolonged time is required. Thus, in an attempt to meet these requirements, numerous nanoparticles have been designed with polymersomes being a popular member of this array [4, 5].

Polymersomes are synthetic amphiphilic block copolymers which self-assemble into nanovesicles. Their basic form consists of one hydrophilic block and one hydrophobic block mimicking the composition of natural phospholipids [6, 7]. Due to their synthetic nature, all parameters like polymer combination, size and membrane thickness, are tuneable [8, 9]. This provides an ample palette of possible creations adaptable to any application requirements.

In addition to their versatility, polymersomes show remarkable properties including fast endocytosis by cells and biocompatibility, high resilience and low permeability (For a more detailed description of polymersomes see chapter 1). These properties make them attractive candidates for drug delivery [10, 11] and as optical markers for in vivo imaging applications [12–14]. Loading fluorescent materials into polymersomes often helps to reduce the innate cytotoxicity of the labels [15].

Among the numerous studies only very few have focused on the dynamics of polymersome uptake, their long-term imaging potential or their degradation in vitro and in vivo. Gathering information on these aspects is crucial when considering polymersomes for bioimaging and medical applications. For this study, polymersome synthesis was performed using the block copolymer Polyisobutylene-monomethyl polyethylene glycol (PIB-PEG-Me), see Figure 3.1 (design and preparation of polymersomes was done by Dr. Sven Askes, Leiden). Polyisobutylene (PiB) was chosen as a hydrophobic block as it is known for its high hydrophobicity and is approved by the FDA for its great biocompatibility. Further, it exhibits low permeability for small molecules (e.g., water), as well as high chemical resistance [16]. As a hydrophilic block Polyethylene glycol (PEG) was used. PEG became a standard for surface functionalization and is widely applied in bio-imaging applications. Additionally, PEG forms a maximum-density brush on the surface of polymersomes, providing them with in vivo stealthiness to evade the immune system [17, 18]. Lastly, the application of PiB-PEG based polymersomes for bio-imaging applications is still limited [19], thus providing novelty to this study.

The amphiphilic nature of polymersomes allows it to encapsulate hydrophobic molecules in the membrane and hydrophilic molecules in the vesicle interior [20]. Thus, to investigate the long-term stability of the nanovesicles, two fluorescent dyes with distinct fluorescence spectra were incorporated (Figure 3.1). The aqueous interior was loaded with sulforhodamine B (SRB). This dye has its excitation maxima at $\lambda_{(ex)}$ = 532 nm and is well suited for frequent and long-term exposure imaging. Additionally, it is quickly removed by the cells when released from liposomes reducing any toxicity [21].

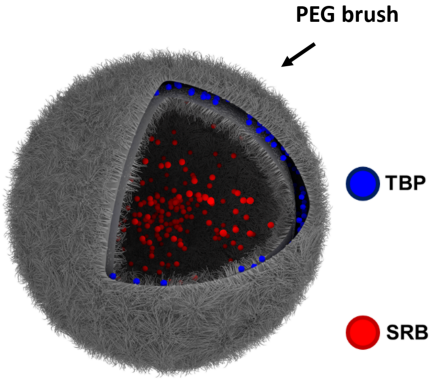

Figure 3.1: Schematic representation of the dual fluorescent polymersomes. The representation shows the localization of the fluorophores 2,5,8,11-tetra(tert-butyl)perylene (TBP) and sulforhodamine B (SRB), and the polyethylene glycol (PEG-) brush (adapted from Askes *et al.* (2018)).

The membrane was labelled with lipophilic 2,5,8,11-tetra(tert-butyl)perylene (TBP) which absorbs at 360-450 nm and fluoresces at 450-550 nm [22]. The TBP fluorescence signal was excited with at $\lambda_{(ex)}$ = 405 nm and used to check for colocalization with the SRB signal at different time points. In this way, we were able to examine whether the polymersomes remained fully intact. In the case of a membrane rupture, the SRB would leak out while TBP would still provide information about the localization of the ruptured remains of the particle. Further, the fluorescence spectra of both dyes are not spectrally overlapping and SRB is not efficiently excited using 405 nm light. Thus, these dyes qualify well as a double label.

To study uptake dynamics and intracellular long-term fate of the dual-labelled PiB-PEG-Me polymersomes, we utilized a Spinning Disc Confocal Microscope (Nikon) and employed a well-studied human lung carcinoma cell line (A-549). This cell line is frequently used as a tool for biomedical research as well as drug screening [23, 24].

3.2. RESULTS AND DISCUSSION

3.2.1. ENDOCYTOSIS AND INTRACELLULAR TRANSPORT

To visualize the endocytosis and transport of polymersomes by A-549 cells, time-lapse with an imaging period of 2h was performed (Figure 3.2). Image acquisition started 5 min before adding the polymersomes (t = 0 min) to catch the docking moment of the particles at the cell membrane. The frame rate was one image every 5 s including four z-slices with a spacing of 1.5 μm. The z-slices were used for a maximum intensity projection of the signal.

For a better cell volume resolution and fast imaging settings, carboxyfluorescein succinimidyl ester (CFSE; $\lambda_{(ex)}$ = 488 nm) was used as a fluorescent cytoplasmic label. Due

to the flat structure of A-549 cells, the voluminous nucleus can be easily distinguished using this cytoplasmic label. Microscopy of polymersomes was performed using only 561 nm laser as frequent exposure with 405 nm damages cells [25].

Hardly minutes after introducing polymersomes, an initial docking of numerous particles at the outer cell membrane was observed. Then the particles lining the membrane were taken inside, moving steadily towards the nucleus (Figure 3.2 a; Video 1 at Askes *et al.* (2018) [26]). The persistency of their movement strongly indicates an active transport mechanism along the cytoskeleton [27, 28].

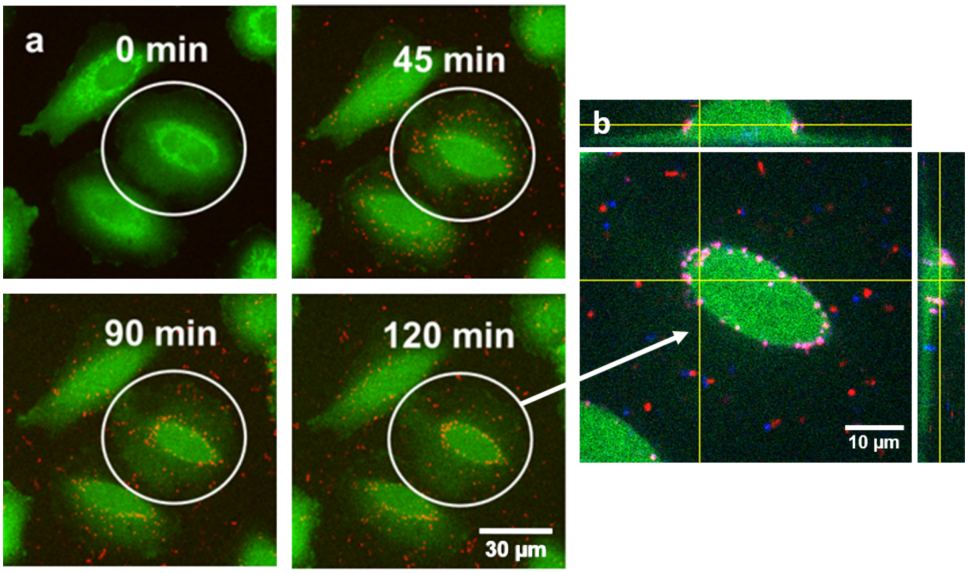

Figure 3.2: Two-hour time-lapse confocal fluorescence imaging of dual-fluorescent polymersomes (red, $\lambda_(ex) = 561nm$) in living A549 cells (labeled with CFSE; green, $\lambda_(ex) = 488nm$). a) Selected frames at 0 min, 45 min, 90 min, and 120 min. Polymersomes were added at t = 5 min. Each image is created using a maximum intensity projection of 4 z-slices with 1.5 μm distance. b) Detailed z-stack (0.3 μm distance) showing a xz and yz projection at the yellow lines. Collected after 2h of incubation with $\lambda_(ex) = 405, 488, and 561nm$ (blue, green, and red, respectively). The full experiment is shown online in Video V1 of Askes *et al.* (2018).

With advancing imaging time, a growing number of particles localized at the perinuclear area. The first wave of docked polymersomes achieved their destination area by the end of 1.5 h (Figure 3.2 a, t = 90 min). Once there, they remained stationary, thus indicating that no exocytosis was taking place. A close-up and lateral view taken at the end of the time-lapse imaging is shown in Figure 3.2 b. The 405 nm laser was included to show the colocalization (violet) of TBP (blue) and SRB (red), confirming the presence of intact polymersomes.

The uptake and intracellular sorting of nanoparticles depend on many factors. The influencers are on the one hand particle parameters, and on the other hand the cell type and state [29]. However, nanoparticles are typically endocytosed via a clathrin-dependent pathway, transported actively by microtubule motors, and finally deposited

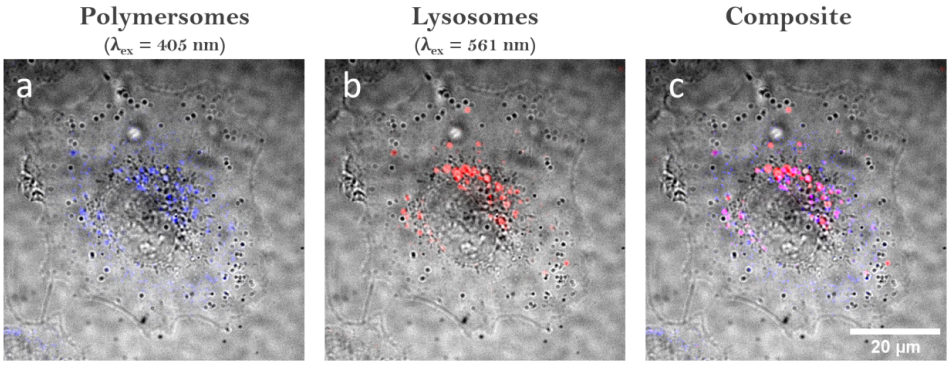

Figure 3.3: Confocal imaging showing the localization of polymersomes, lysosomes and the composite inside A549 cells. a) Single-labelled TBP polymersomes ($\lambda_(ex) = 405nm$; blue) after 30 min incubation in A549 cells (BF). SRB was excluded during preparation, i.e. polymersomes show no signal under 561 nm excitation. b) Lysosomes labelled with LysoTracker Red ($\lambda_(ex) = 561nm$; red) after 2h incubation. c) Composite of a&b showing colocalization of polymersomes and lysosomes (purple).

in lysosomes [30, 31].

To confirm that the particles are enclosed by lysosomes, we employed LysoTracker Red ($\lambda_{(ex)}$ = 561 nm) and used single-labelled polymersomes loaded only with TBP ($\lambda_{(ex)}$ = 405 nm). Thus, polymersomes did not fluoresce when excited with 561 nm. Further, the irradiation of LysoTracker with 405 nm was negligible, as verified by control experiments (not shown). For this test, we incubated the polymersomes for 2 h with A-549 cells (Figure 3.3 a), giving them sufficient time to be incorporated. Subsequently, we removed the excess by washing and stained the living cells with the lysosomal label (Figure 3.3 b). The composite in Figure 3.3 c shows a clear overlay of both signals, particularly in the perinuclear area, confirming the assumed endo-lysosomal pathway. In summary, imaging of the first 2 h shows that dual-fluorescent polymersomes are quickly endocytosed by A549 cells, actively transported to the perinuclear area within 1.5 h and deposited in lysosomes.

3.2.2. 86H TIME-LAPSE IMAGING AND MITOSIS

To investigate the intracellular fate of PiB-PEG-polymersomes on a longer time scale, we performed a time-lapse with an imaging period of 86 h and images taken every 2 min. Based on our prior observation that forerunner polymersomes needed about 1.5 h to be fully incorporated, we incubated the cells and particles for 4h. This gave sufficient time for a high number of polymersomes to be endocytosed and transported to the perinuclear area. Not (yet) incorporated nanovesicles were removed by washing. Cells were visualized using brightfield and 561 nm laser excitation to track polymersome (Figure 3.4 a; Video 2 at Askes *et al.* 2018 [26]). Excitation with 405 nm was again omitted during imaging to reduce phototoxicity.

At the start of the experiment the polymersomes were localized in the perinuclear

area, as expected. Throughout the duration of the imaging period they were shuffled around probably due to intracellular activity and cytoskeletal rearrangements, but they remained located in the perinuclear area. The cells exhibited usual behaviour of locomotion and mitosis, without any signs of polymersome-caused cell stress. Note that there are no free-floating particles observed at any time indicating that cells did not exocytose the nanovesicles.

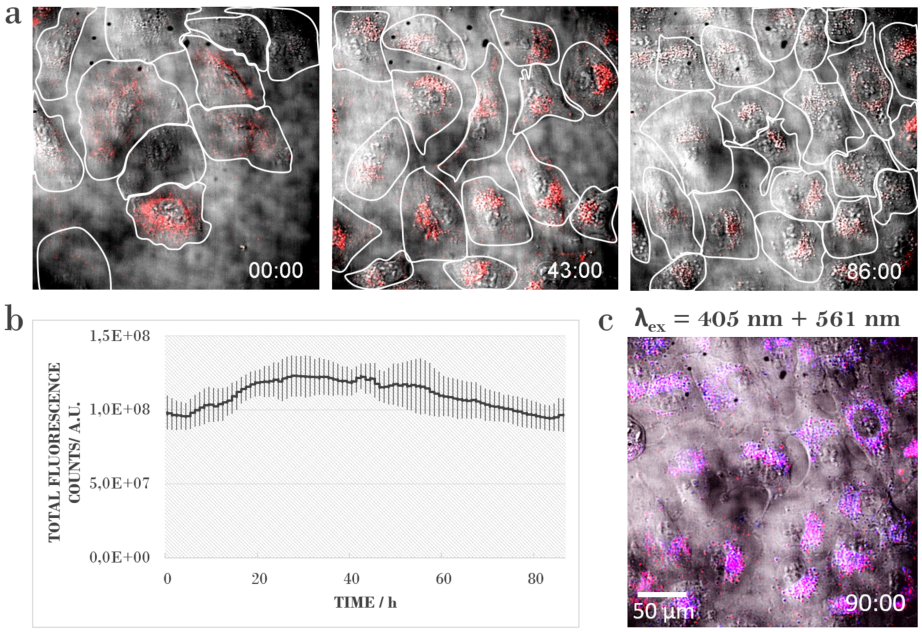

Figure 3.4: 86-h time-lapse confocal imaging showing long-term fate of dual-fluorescent polymersomes inside A549 cells. a) Selected frames at t = 0 h, t = 43 h, and t = 86 h. Polymersomes ($\lambda_{(ex)}$ = 561 nm; red) remains inside the cells throughout the entire imaging duration. Cell number increases due to proliferation and the fluorescence signal per cell decreases. b) Total fluorescence count ($\lambda_{(ex)}$ = 561 nm) per frame over 86 h (n = 5 positions) shows that the overall fluorescence signal of polymersomes remains quite stable over time. Increase in signal can be due to additional cells migrating into the frame. c) Intact polymersomes after 90 h of imaging confirmed by the presence and colocalization of TBR and SRB signal ($\lambda_{(ex)}$ = 561 nm (red) and $\lambda_{(ex)}$ = 405 nm (blue), respectively). Time is shown in hour : minute format. The full experiment is shown online in Video V1 in Askes *et al.* (2018).

The signal intensity of polymersomes remained relatively stable throughout the entire acquisition time. This is revealed by the total fluorescence counts per frame using five locations per time point (Figure 3.4 b). Naturally, during the 86 h single cells migrate in and out of the frames thus influencing the overall fluorescence profile slightly. Further, the incorporated number of polymersomes will vary from cell to cell. Besides the particle concentration and incubation time, also cell cycle and endocytosis dynamics determine the number of endocytosed nanoparticles per cell [32, 33]. This means,

that the particle-binding kinetics at the cell membrane and the dynamics of endosome formation regulate the final endosomal loading with nanoparticles [34].

At the end of time-lapse imaging , data including 405 nm excitation was obtained (Figure 3.4 c). The colocalization (violet) of TBP (blue) and SRB (red) signal revealed the prevailed integrity of PiB-PEG-polymersomes. This high long-term resistance is valuable for bioimaging, as an often-encountered problem is photobleaching of the probes and thus a decrease in fluorescence signal. Consequently, decreasing signal-to-noise ratio complicates the acquisition of usable data, particularly during a long-term imaging. Thus, developing resistant fluorescent nanomaterials which allow a high frame rate during imaging together with a high signal preservation is crucial to enable the observation of intracellular dynamics in real time.

During the 86 h - imaging duration, cells undergo regular mitosis. During this process, polymersomes are shuffled around in the mother cell and subsequently shared between two daughter cells. Partitioning of polymersomes occurs indirectly, as it is rather loaded endosomes and lysosomes that are segregated as intact entities during cell division [35]. Thus, despite nearly symmetrical vesicle inheritance, a variable vesicle loading can result in an asymmetric particle partitioning among the daughter cells [36].

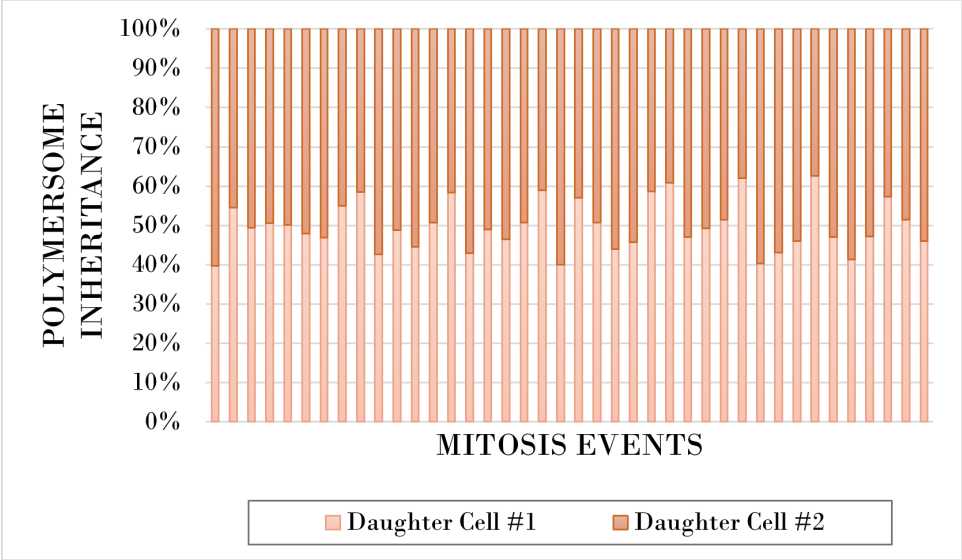

Figure 3.5: Distribution of polymersome inheritance between daughter cells after mitosis (n = 40 mitosis events. Inheritance ranges from 50/50 to 40/60, with an average of 50%. Polymersome number was measured indirectly by counting pixel values within the cells using a region of interest (ROI) around the cell edges. Daughter Cell ♯1 and ♯2 were defined randomly.

Inheritance distribution of dual-labelled polymersomes for 80 cells (40 mitosis events) is shown in Figure 3.5. The polymersome dose was measured indirectly using total fluorescence count within a ROI which drawn around cell edges. The fluorescence count of both daughter cells was used as 100% and not the fluorescence count of the mother cell. The reason is that the pixel count was found to vary slightly with the area which the cell is occupying at the measured time point. A fully stretched out and flat cell displays a higher number of polymersomes than a rounded cell, where polymersomes distribute in the z-plane and thus are not well detectable. Thus, to reduce the impact of this variation, the sum of the daughter cells was used as the overall polymersome value (= 100 %).

The segregation occurs slightly asymmetric between the daughter cells but shows a clear average of 50 % (n = 40 mitosis events). These numbers agree with literature showing a similar inheritance pattern [37–39] and indicate a relatively equal loading of endosomes with polymersomes. The dual-labelled polymersomes could serve as a robust optical tracer of the endo-lysosomal pathway without interfering with it. This can be a useful tool in various studies, including deciphering the mechanism determining vesicle inheritance.

Overall, these experiments show that the PiB-PEG-polymersomes remain intact when exposed to intracellular environment for 86 h. Additionally, these polymersomes are well tolerated by the cell long-term and are incorporated into the usual cell cycle. Although the polymersomes accumulate in lysosomes, they are not degraded during 86 h. Their resistance to lysosomal breakdown might be attributed to the high chemical inertness of the PiB polymer block. Meanwhile the fully PEGylated surface may serve as a reason why the polymersomes are not interfering with cellular activity.

3.2.3. LONG-TERM ANALYSIS FOR 11 DAYS

Based on the exceptional stability of the PiB-PEG-Me polymersomes during the first 90h, we set out to investigate their long-term integrity on a timescale of 11 days. Following the prior protocol, cells were incubated with dual-labelled polymersomes for 4 h and not (yet) endocytosed particles were removed by washing (Day 0). Imaging data was collected with brightfield exposure, and 405 nm and 561 nm excitation on Day 0, Day 3, Day 7, and Day 11 (Figure 3.6). To prevent over-confluency and cell stress, cells were passaged every 2-3 days. As observed before, the polymersomes are split during mitosis among the daughter cells and thus a subsequent decrease in the fluorescence signal per cell was to be expected.

Visual analysis of polymersome fluorescence over time showed a strong signal on day 3, consistent with our observations during the 86 h imaging period (Figure 3.6 a). Between day 3 and 7 a strong signal decline was measured with many cells displaying only TBP fluorescence, but barely SRB fluorescence. This indicates polymersome membrane rupture and leakage of SRB dye. The localized TBP signals confirms the presence of the collapsed PiB-PEG-membrane, and the absence of SRB signal confirms its excretion by the cell. On day 11, there was hardly any detectable fluorescence for TBP and SRB suggesting the full degradation or clearance of all polymersomes components.

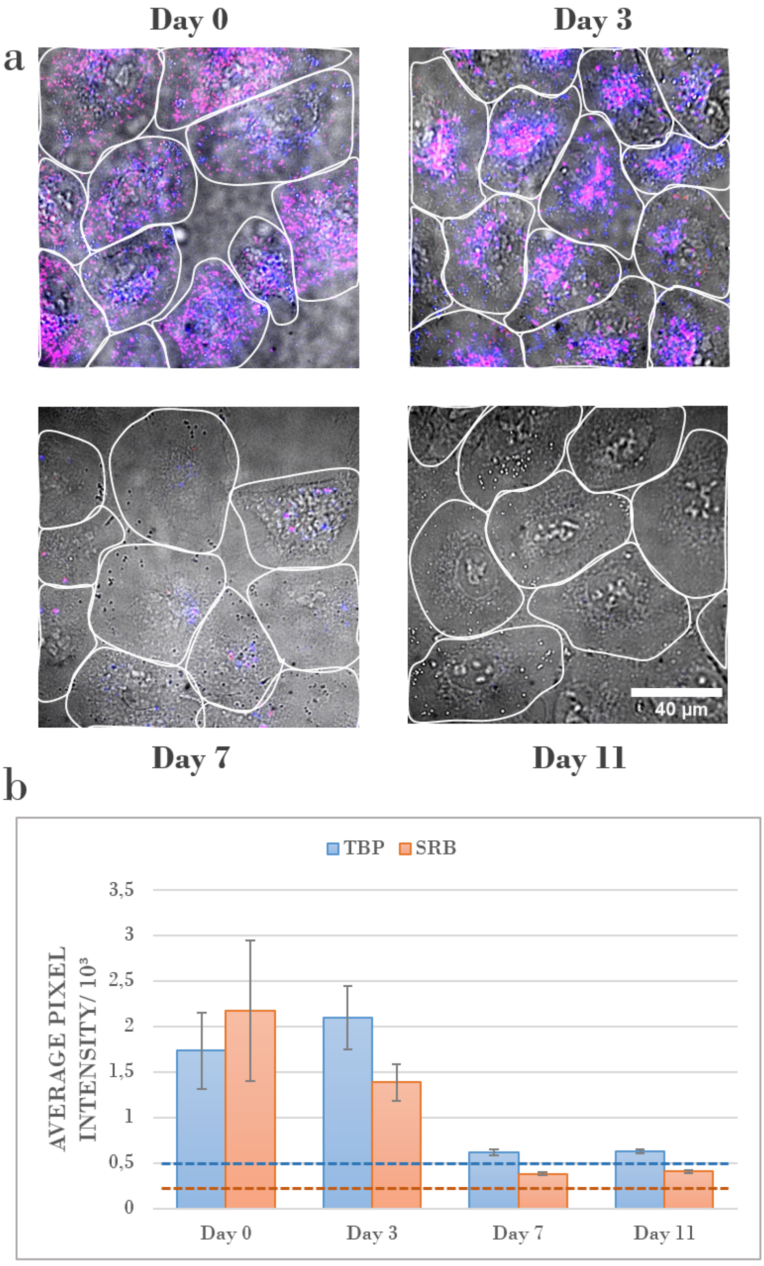

Figure 3.6: Observation of polymersomes fluorescence in A549 cells over 11 days. a) Representative composites of confocal bright field showing living A549 cells and fluorescence signal of dual-fluorescencet polymersomes ($\lambda_(ex)$ = 561nm (red) and $\lambda_(ex)$ = 405nm (blue); colocalization shown as purple). Polymersomes are fully intact and present at Day 0 and Day 7, considerably reduced at Day 7, and hardly detectable at Day 11. Each fluorescence shows a maximum intensity projection of 5 z-slices with 1.5 µm distance. b) Quantification of TBR (blue) and SRB (red) fluorescence intensity inside cells showing a drop around noise levels by Day 7 and Day 11. Fluorescence signal is expressed in mean pixel value using a ROI around the cell edges. Error bars showing standard deviation (n = 10 frames with several cells per measurement). Noise levels are indicated with blue and red dotted lines.

Additional *ex vivo* experiments (shown in corresponding publication Askes *et al.* (2018) [26], Fig. S 8) confirm an enzymatic degradation of the polymersomes which seems to occur due to a cleavage of the ester linker in the PiB-PEG block copolymer. Quantification of the signal intensity per cell area (N = 10 positions) at the different days displays the observed trend (Figure 3.6 b). It should be noted, that throughout the experiment duration no free-floating particles were observed, thus indicating no exocytosis also on a long-time scale.

The 11-day analysis confirmed the high resistance and biocompatibility of PiB-PEG-polymersomes. Up to 7 days the polymersomes remain fully intact, retaining a high dual-signal, withouth imparing cellular health. Even on Day 11, A-549 cells showed normal behavior without any signs of cytotoxicity. Additional FACS data confirmed the polymersomes signal and biocompatibility (Askes *et al.* (2018) [26], Figure 3.5). The polymsersomes are degraded slowly with a seeminlgy reaching full clearance after 11 days. The slow degradation of these nanovesicles can serve as a great feature for long-term imaging applications e.g. to investigate in more details the endo-lysosomal pathway.

3.2.4. CONCLUSIONS

This chapter introduced novel dual-fluorescent PiB-PEG-polymersomes and focused on their short-term and long-term dynamics within living cells using time-lapse fluorescence microscopy. Short-term analysis showed that these nanovesicles were quickly endocytosed by human lung carcinoma cells (A549) within the first minutes of incubation. Following, we observed directional transport of the polymersomes towards the perinuclear area and subsequent encapsulation by lysosomes.The SRB fluorescence signal was retained during the fast 2 h time-lapse with a frame rate of one image every 5 sec as well as a long-term 86 h time-lapse with images every 2 min, without compromising its intensity too much. This attribute is highly important for imaging experiments as a degrading signal complicates tracking of the particles and requires higher laser intensity for a better signal, which in turn is damaging for living cells. Using two fluorescent dyes within the membrane and within the intraluminal space, allowed to report on the integrity of the polymersomes within the intracellular environment by simply using fluorescence microscopy. Fluorescence time-lapse imaging also allowed to observe that the particles were equally divided among daughter cells during mitosis and slowly degraded until a full clearance between day 7-11.

In summary, these nanovesicles were highly biocompatible without impacting cellular health over the entire experimental duration and showed stable long-term fluorescence signal. Thus, these highly resistant polymersomes can be a great tool for diverse *in vivo* bio-imaging applications, serving either as an optical label for whole cells or marking the endolysosomal network.

3.3. MATERIALS AND METHODS

For details regarding the preparation of dual-fluorescent PiB-PEG polymersomes please find the publication Askes *et al.* (2018) (Biomaterials) [26].

3.3.1. GENERAL CELL CULTURE

A549 human lung carcinoma cells were cultured in 25 cm2 flasks in 8 mL Dulbecco's Modified Eagle Medium with phenol red (DMEM; Sigma Life Science, USA), supplemented with 8.2% v/v fetal calf serum (FCS; Hyclone), 200 mg/L penicillin and streptomycin (Pen/Strep; Duchefa), and 1.8 mM glutamine S (GM; Gibco, USA), under standard culturing conditions (humidified, 37 °C atmosphere containing 7.0% CO2). The cells were split approximately once per week upon reaching 70-80% confluency, using seeding densities of 2 x 105 cells, and the medium was refreshed once per week. Cells were passaged for 4-8 weeks.

3.3.2. CELL IMAGING PREPARATION

For cell-imaging, after passing and centrifuging, the cells were suspended in Opti-MEM (Life Technologies, USA), supplemented with 2.5% FCS, 200 mg/L Pen/Strep, and 1.8 mM GM. The cells were typically seeded in an IBIDI glass-bottom 8-well chamber slide at 20-40 x 103 cells per well or in a 35 mm glass-bottom dish at 50-60 x 103 cells and left in the incubator for 24 h before treatment. For experiments, cells were incubated with a 1:1 v/v mixture of sterilized polymersomes and OptiMEM for 2 or 4 h at a typical concentration of 0.5 mg/mL. Then, the cells were washed once with PBS and resupplied with OptiMEM. In case of staining with carboxy-fluorescein succinimidyl ester (CFSE), the cells were incubated with 10 mM CFSE for 20 min, washed twice with PBS and resupplied with OptiMEM before imaging.

3.3.3. LIVE-CELL IMAGING

Live-cell images were acquired on a Nikon Ti Eclipse inverted microscope (Nikon Corporation, Japan) equipped with a Yokogawa 10,000 rpm spinning disc unit (Andor Technology Ltd., United Kingdom) and a stage-top miniature incubation chamber (Tokai Hit, Japan; INUG2E-TIZ) with a TIZ-D35 sample holder mounted on a Nikon Ti-S-ER motorized stage. The cells were imaged with either a 40x (Nikon Plan Fluor, numerical aperture (NA) 0.75), 60x (Nikon Plan Apo l, NA 1.4), or 100x objective (Nikon SR Apo TIRF, NA 1.49). An Agilent MLC400B monolithic laser combiner (Agilent Technologies, Netherlands) was used for excitation at 405 nm, 488 nm and 561 nm in combination with a Semrock custom-made quad-band dichroic mirror for excitation wave- lengths 400-410, 486-491, 460-570, and 633-647 nm. The emission was filtered using a Semrock quad-band fluorescence filter (TR-F440-521-607-700), which has specific transmission bands at 440 ± 40 nm, 521 ± 21 nm, and 607± 34 nm, or otherwise a Semrock TR-F447-060 for $\lambda_{(ex)}$ = 405 nm or a Semrock TR-F607- 036 for $\lambda_{(ex)}$ = 561 nm . All images were captured by an Andor iXon Ultra 897 High-speed EM-CCD camera. Image acquisition was automated using NisElements software (LIM, Czech Republic). Typical exposure times per z-slice were 100-200 ms.

3.3.4. IMAGE ANALYSIS

All images and data were processed using Fiji ImageJ [40], and/or Microsoft Excel software. For Figure 3.4, total fluorescence count was calculated using mean grey value of whole frames for $\lambda_{(ex)}$ = 561 nm , and multiplied by the area in pixels (512 x 512). For Figure 3.5, integrated density within the ROI of one cell was used. For Figure 3.6, mean grey value within ROI of one cell was measured.

3.4. REFERENCES

[1] Jonghoon Kim, Nohyun Lee, and Taeghwan Hyeon. “Recent development of nanoparticles for molecular imaging”. In: *Philosophical Transactions of the Royal Society A: Mathematical, Physical and Engineering Sciences* 375.2107 (2017), p. 20170022.

[2] Héloïse Ragelle et al. “Nanoparticle-based drug delivery systems: a commercial and regulatory outlook as the field matures”. In: *Expert opinion on drug delivery* 14.7 (2017), pp. 851–864.

[3] Andreas Ettinger and Torsten Wittmann. “Fluorescence live cell imaging”. In: *Methods in cell biology* 123 (2014), pp. 77–94.

[4] Otto S Wolfbeis. “An overview of nanoparticles commonly used in fluorescent bioimaging”. In: *Chemical Society Reviews* 44.14 (2015), pp. 4743–4768.

[5] Guorong Sun et al. “Bright fluorescent nanoparticles for developing potential optical imaging contrast agents”. In: *Nanoscale* 2.4 (2010), pp. 548–558.

[6] Caterina LoPresti et al. “Polymersomes: nature inspired nanometer sized compartments”. In: *Journal of Materials Chemistry* 19.22 (2009), pp. 3576–3590.

[7] Dennis E Discher and Fariyal Ahmed. “Polymersomes”. In: *Annual Review of Biomedical Engineering* 8.1 (2009), pp. 323–341.

[8] Harry Bermudez et al. “Molecular weight dependence of polymersome membrane structure, elasticity, and stability”. In: *Macromolecules* 35.21 (2002), pp. 8203–8208.

[9] Fenghua Meng and Zhiyuan Zhong. “Polymersomes spanning from nano-to microscales: advanced vehicles for controlled drug delivery and robust vesicles for virus and cell mimicking”. In: *The Journal of Physical Chemistry Letters* 2.13 (2011), pp. 1533–1539.

[10] Tayebeh Anajafi and Sanku Mallik. “Polymersome-based drug-delivery strategies for cancer therapeutics”. In: *Therapeutic delivery* 6.4 (2015), pp. 521–534.

[11] Gong-Yan Liu, Chao-Jian Chen, and Jian Ji. “Biocompatible and biodegradable polymersomes as delivery vehicles in biomedical applications”. In: *Soft Matter* 8.34 (2012), pp. 8811–8821.

[12] Marzia Massignani et al. “Enhanced fluorescence imaging of live cells by effective cytosolic delivery of probes”. In: *PLoS one* 5.5 (2010), e10459.

[13] David A Christian et al. “Polymer vesicles with a red cell-like surface charge: microvascular imaging and in vivo tracking with near-infrared fluorescence”. In: *Macromolecular rapid communications* 31.2 (2010), pp. 135–141.

[14] P Peter Ghoroghchian, Michael J Therien, and Daniel A Hammer. “In vivo fluorescence imaging: a personal perspective”. In: *Wiley Interdisciplinary Reviews: Nanomedicine and Nanobiotechnology* 1.2 (2009), pp. 156–167.

[15] Marine Camblin et al. “Polymersomes containing quantum dots for cellular imaging”. In: *International journal of nanomedicine* 9 (2014), p. 2287.

[16] Judit E Puskas et al. “Polyisobutylene-based biomaterials”. In: *Journal of Polymer Science Part A: Polymer Chemistry* 42.13 (2004), pp. 3091–3109.

[17] Alexander L Klibanov et al. “Amphipathic polyethyleneglycols effectively prolong the circulation time of liposomes”. In: *FEBS letters* 268.1 (1990), pp. 235–237.

[18] Arnaud Vonarbourg et al. “Parameters influencing the stealthiness of colloidal drug delivery systems”. In: *Biomaterials* 27.24 (2006), pp. 4356–4373.

[19] Sven HC Askes et al. “Imaging upconverting polymersomes in cancer cells: biocompatible antioxidants brighten triplet–triplet annihilation upconversion”. In: *Small* 12.40 (2016), pp. 5579–5590.

[20] Wen-Chia Huang et al. “Development of a diagnostic polymersome system for potential imaging delivery”. In: *Colloids and Surfaces B: Biointerfaces* 128 (2015), pp. 67–76.

[21] Scott R Burks et al. “Co-encapsulating the fusogenic peptide INF7 and molecular imaging probes in liposomes increases intracellular signal and probe retention”. In: *PloS one* 10.3 (2015), e0120982.

[22] Sven Holger Christiaan Askes. “Upconverting nanovesicles for the activation of ruthenium anti-cancer prodrugs with red light”. PhD thesis. Leiden University, 2016.

[23] Adi F Gazdar et al. “Lung cancer cell lines as tools for biomedical discovery and research”. In: *Journal of the National Cancer Institute* 102.17 (2010), pp. 1310–1321.

[24] Michele Zanoni et al. “3D tumor spheroid models for in vitro therapeutic screening: a systematic approach to enhance the biological relevance of data obtained”. In: *Scientific reports* 6.1 (2016), pp. 1–11.

[25] Samantha L Hopkins et al. “An in vitro cell irradiation protocol for testing photopharmaceuticals and the effect of blue, green, and red light on human cancer cell lines”. In: *Photochemical & Photobiological Sciences* 15.5 (2016), pp. 644–653.

[26] Sven HC Askes et al. “Dynamics of dual-fluorescent polymersomes with durable integrity in living cancer cells and zebrafish embryos”. In: *Biomaterials* 168 (2018), pp. 54–63.

[27] Elizabeth Granger et al. “The role of the cytoskeleton and molecular motors in endosomal dynamics”. In: *Seminars in cell & developmental biology*. Vol. 31. Elsevier. 2014, pp. 20–29.

[28] Delphine Arcizet et al. “Temporal analysis of active and passive transport in living cells”. In: *Physical review letters* 101.24 (2008), p. 248103.

[29] Nuri Oh and Ji-Ho Park. “Endocytosis and exocytosis of nanoparticles in mammalian cells”. In: *International journal of nanomedicine* 9.Suppl 1 (2014), p. 51.

[30] Gaurav Sahay, Daria Y Alakhova, and Alexander V Kabanov. “Endocytosis of nanomedicines”. In: *Journal of controlled release* 145.3 (2010), pp. 182–195.

[31] Joanna Rejman, Alessandra Bragonzi, and Massimo Conese. “Role of clathrin- and caveolae-mediated endocytosis in gene transfer mediated by lipo-and polyplexes”. In: *Molecular Therapy* 12.3 (2005), pp. 468–474.

[32] Jong Ah Kim et al. “Role of cell cycle on the cellular uptake and dilution of nanoparticles in a cell population”. In: *Nature nanotechnology* 7.1 (2012), pp. 62–68.

[33] Parisa Foroozandeh and Azlan Abdul Aziz. “Insight into cellular uptake and intracellular trafficking of nanoparticles”. In: *Nanoscale research letters* 13.1 (2018), pp. 1–12.

[34] Paul Rees et al. “The origin of heterogeneous nanoparticle uptake by cells”. In: *Nature communications* 10.1 (2019), pp. 1–8.

[35] Trygve Bergeland et al. “Mitotic partitioning of endosomes and lysosomes”. In: *Current Biology* 11.9 (2001), pp. 644–651.

[36] Huw D Summers et al. “Quantification of nanoparticle dose and vesicular inheritance in proliferating cells”. In: *ACS nano* 7.7 (2013), pp. 6129–6137.

[37] Yan Yan et al. “Particles on the move: intracellular trafficking and asymmetric mitotic partitioning of nanoporous polymer particles”. In: *Acs Nano* 7.6 (2013), pp. 5558–5567.

[38] Kuang-Kai Liu et al. “Endocytic carboxylated nanodiamond for the labeling and tracking of cell division and differentiation in cancer and stem cells”. In: *Biomaterials* 30.26 (2009), pp. 4249–4259.

[39] Huw D Summers et al. “Statistical analysis of nanoparticle dosing in a dynamic cellular system”. In: *Nature nanotechnology* 6.3 (2011), pp. 170–174.

[40] Johannes Schindelin et al. “Fiji: an open-source platform for biological-image analysis”. In: *Nature methods* 9.7 (2012), pp. 676–682.

4

NEURAL PROGENITOR CELLS CHARACTERIZATION AND LABELLING

In this chapter, we introduce the murine neural progenitor cells line C17.2 and confirm its multipotency via differentiation into a mixed population of neurons and astrocytes. Further, several fluorescent labels are explored as well as the transduction with fluorescent reporters with the focus to label cell nucleus and body. The genetically modified cell line is used for time-lapse imaging and data analysis in chapter 5.

4.1. INTRODUCTION

Neural progenitor cells (NPCs) are multipotent stem cells of the central nervous system (CNS) which reside in specific niches in adults and embryos [1]. They have the capacity for continuous self-renewal and can differentiate into the three major cell lineages of the nervous system: neurons, astrocytes, and oligodendrocytes [2]. This is crucial for embryonic as well as adult neurogenesis. Additionally, NPCs secrete neurogenic factors which contribute to a healthy neural microenvironment [3]. Transplantation studies of NPCs into injured or degenerating CNS are promising and show high potential for the treatment of neurodegenerative disorders like Parkinson's, Alzheimer's, ALS, or stroke/ischemia [4, 5]. Since the discovery of neural progenitor cells, research effort has been focused on increasing our understanding of these cells [6]. A crucial breakthrough was the establishment of the first protocols in the 1990's, enabling isolation of NPCs from rodent brains and their culture under laboratory conditions [7].

Meanwhile, primary NPCs have been successfully isolated not only from rodents but also from human foetal brains [8, 9]. As extracted primary cells resemble the phenotypic profile of original tissue the closest, they remained to the present a prominent source to obtain NPCs for research purposes. However, primary cells have only a limited lifespan in culture. The common reason is the genetical predetermination of somatic cells to undergo growth arrest or cell death after a finite number of cell divisions. This finite number is explained by the Hayflick limit stating that upon each cell division the telomeres, which protect chromosome stability, shorten, and mitosis stops completely when telomeres reach a critical length [10]. Despite the multipotent nature of NPCs, which suggests continuous proliferation capacity *in vivo*, *in vitro* isolated primary NPCs also undergo cell death and show phenotypical or genotypical modifications after several subcultures. Next to telomere shortening, this can be due to the artificial culture environment which leads to cell stress and subsequently to an accumulation of abnormalities and senescence-associated changes. Additionally, isolated NPCs are of polyclonal origin and thus exhibit various degrees of potency and commitment. In culture, this results in a variation of properties and population heterogeneity. The limited stability of primary NPCs in culture generates a recurrent need for newly isolated samples from rodents or (human) foetal tissue.

To circumvent this problem and maintain cells indefinitely in culture it is possible to genetically modify them and thus generate an immortal cell line. Immortalization is essentially a partial deregulation of the cell cycle resulting in continuous proliferation of cells. This can be achieved through a variety of chemical or viral methods. A widely used technique is inserting v-myc into the cellular genome using a replication-defective, infective retroviral vector. Myc is a family of transcription factors that control many cellular processes. It regulates the cell cycle by stimulating proliferation and stemness, and repressing differentiation [11]. Villa *et al.* (2000) compared several immortalizing genes in their capability to produce a stable human NPC line (hNS1 and hNS2, formerly HNSC.100) and found that v-myc was the most effective option [12]. The authors suggest that v-myc preserves the telomeres due to expression of high telomerase activity, avoiding accumulation of chromosomal abnormalities and aging-associated modifications upon cell division. Next to hNS1, more neural progenitor lines have been established using v-myc including C17.2, HC2S2, and MAH cells [13–15]. The stable, clonal

NPC lines have been successfully employed for neural transplantation studies [16–18].

The genetic modifications that cells undergo to become immortal can result in loss of their natural characteristics, and thus not resemble their *in vivo* tissue of origin sufficiently. The closest approach to the tissue *in vivo* is using pluripotent stem cells. Pluripotent stem cells have a higher potential than multipotent stem cells, as they can differentiate into any cell type. However, these cells are usually more laborious to culture and their differentiation is a complex process which can be challenging to implement in the laboratory for the first time. Additionally, differentiation to neurons and glia cells can take up to several weeks, thus lengthening the timeframe of every experiment. For this reason immortalized cell lines are used for convenience as they are generally easy to handle and widely recognized and have been employed in this study.

The focus of this study was to set up experiments and gain initial data into basic NPC migration and behaviour. For this, the immortalized murine cell line C17.2 was selected. This is a multipotent cell line which can differentiate into a mixed culture of neurons and glia cell within 7 days [19]. In their progenitor state, the cells grow adherent to substrate allowing to seed them homogeneously distributed onto various surfaces. Culture requirements are relatively simple and include the widely used Dulbecco's Modified Eagle's Media (DMEM) mixtures, fetal calf serum (FCS), and two neurotrophic factors (NGF and BDNF) [19]. This multipotent cell line was isolated from the cerebellum of a neonatal mouse and immortalized using a v-myc transfection [15]. C17.2 neural progenitors are used as a model system and have been employed in numerous studies including CNS toxicity [20, 21], differentiation research [22], and neural regeneration [23, 24]. In the latter, these cells integrated into the diseased or injured CNS of animals and underwent neural differentiation. Although, as mentioned above, immortalized cell lines can diverge from their *in vivo* counterparts, they have many advantages, are widely published, and thus act as a practical model system.

In this chapter, the C17.2 cell line is characterized in culture and a dual-transduced monoclonal cell line is established exhibiting a nuclear and an actin label.

4.2. RESULTS AND DISCUSSION

4.2.1. CHARACTERIZATION OF C17.2 CELLS

C17.2 NPCs were purchased from Sigma (♯07062902) and cultured as advised by the provider in serum-containing media (details see Materials). The cells were maintained in culture for up to 25 passages. Under these conditions the progenitor state of the cells remained stable: no spontaneous neural differentiation or other changes were observed. In their undifferentiated state, C17.2 cells showed a homogeneous, elongated morphology with multiple processes (Figure 4.1 a).

In contrast to the by Sigma advised surface coating with Poly-L-Lysine (PLL), the cells were grown on laminin-coated dishes. Initially, cells were cultured on PLL - coated dishes but showed stress signs and exhibited higher death rates. Laminin was considered as an alternative coating as this extracellular matrix-protein is widely employed for neural cultures. A comparison by growing the cells on laminin and PLL for 20 passages showed a healthier cell appearance on laminin-coated surfaces with lower death num-

bers and no signs of any morphological changes (data not shown). Thus, laminin was selected for the daily culture protocol. To confirm the progeny state of the cells and to verify its preservation on laminin, an immunofluorescence targeting the neuroepithelial stem cell protein (nestin) was performed. Nestin is a cytoskeletal intermediate filament which is found during early development of the CNS and is characteristic for neural progenitor cells. It is related to essential functions like proliferation, differentiation, and migration [25]. As expected, cultured C17.2 cells showed a high expression of nestin [19] on both surface coatings (Figure 4.1 c, e).

C17.2 are a particularly interesting cell line due to their multipotent capacity and were shown to produce a mixture of neurons and astrocytes [19]. To confirm their ability for neural maturation, cells were cultured in differentiation media following the protocol established by Lundqvist *et al.* (2013). After 7 days, C17.2 produced as expected a mixed neural population (Figure 4.1 b). Morphological analysis showed typical neuronal phenotypes with small, spherical bodies and variable branches of neurites building a complex network (Figure 4.1 b, inset). Additionally, among the neurons, more flattened cells were found resembling astrocytes (Figure 4.1 c; inset, white arrow) [19]. An immunofluorescence analysis confirmed protein expression of the neuronal marker βIII-tubulin (Figure 4.1 d) [26], as well as the presence of the glial fibrillary acidic protein (GFAP) (Figure 4.1 f) [27].

In summary, cultured C17.2 cells were confirmed to be in their immature state and differentiated as expected into a neural population.

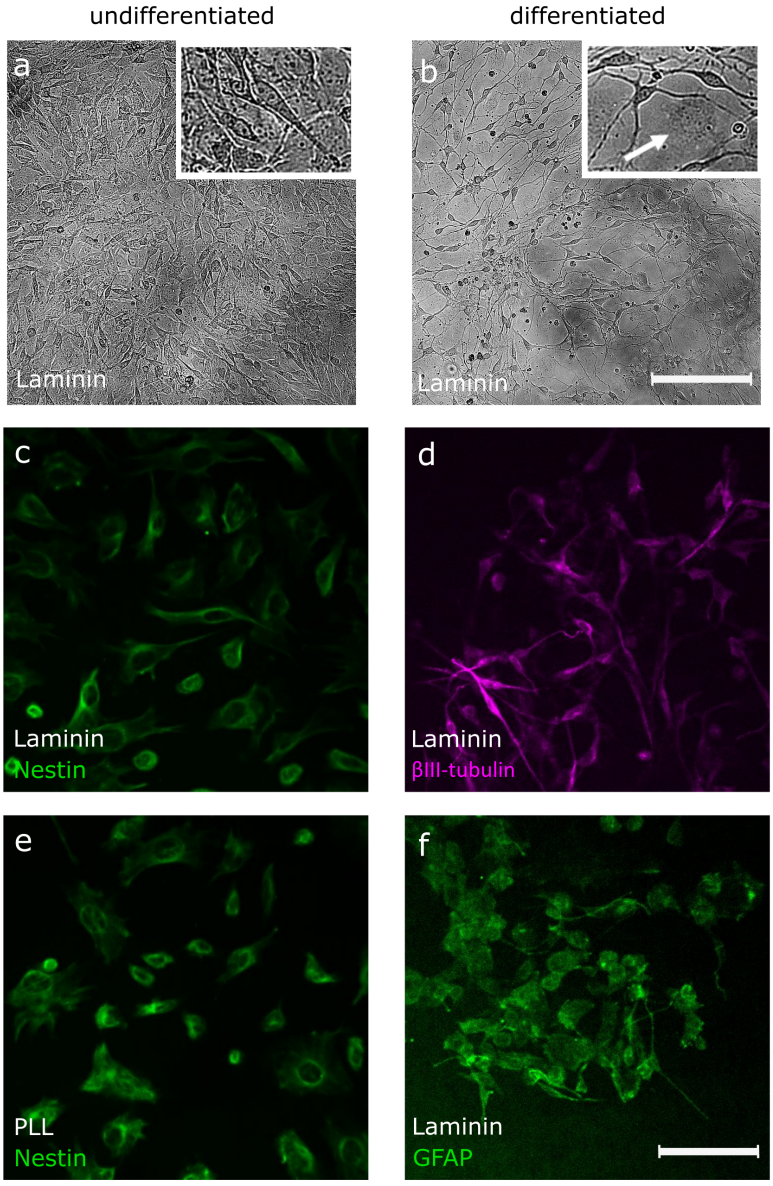

Figure 4.1: C17.2 NSCs in their immature and differentiated state. C17.2 NSCs in their immature and differentiated state. Immature C17.2 cells show an elongated cell body with processes (a) and express the neural progenitor marker nestin when cultured on laminin (c) and PLL-covered (e) surfaces. Differentiated C17.2 cells yield a neural network (b) with neurons showing small cell bodies and expressing the neuronal marker βIII-tubulin (d). Additionally, astrocytes showing a flat morphology (inset, white arrow) express the glial marker GFAP (e). The scale bar is 200 μm for (a-b) and 100 μm for (c-f).

4.2.2. FLUORESCENCE LABELS EXAMINATION

The objective of the study was to analyse NPC migration and behaviour by acquiring time-lapse imaging data using a fluorescence confocal microscope. Thus, fluorescent labels of cell nuclei and cell bodies were required. Ideally, the label should yield a stable signal over at least 24 h of data acquisition, a sufficiently high intensity for a clear signal at a 20x magnification (lens used here for tracking analysis), not interfere with the cellular functions and preferably absorbing at longer wavelengths. Exposing living cells to laser pulses of high intensity light can have a phototoxic effect, and particularly near UV range light can induce DNA damage. Several commercially available products have been assessed as possible fluorescent markers and are listed below. Hoechst 33342, FM4-64, Fluorescein diacetate (FDA), NeuroFluor™ CDr3, NucSpot® Live 650, were available in stock and thus tested for their usability. Whereas BioTracker, CellTracker, and SiR Actin labels were purchased with consideration to the above-mentioned requirements.

Hoechst 33342 (ThermoFisher) is a well-known and popular nuclear dye for living cells. Testing it at concentrations 2-5 μM produced the best results at 5 μM (Figure 4.2 a). Although the nuclei labelling was successful, the signal intensity was not very high and variable among cells. Additionally, the clear disadvantage of Hoechst is its absorption at 405 nm. As mentioned before, blue light is damaging to living cells compared to longer wavelengths, which becomes particularly problematic during frequent and long-term exposure of time-lapse imaging.

BioTracker 488 Green Nuclear Dye (Merck) was tried as an alternative nuclear label. This label is advertised as having higher photostability than Hoechst 33342 and has the advantage of absorbing in the green spectra which is moderately less toxic to living cells. Following the manufacturer's protocol, the labelling failed as the dye adsorbed onto the laminin-coated surface on which C17.2 cells were grown (Figure 4.2 b). The approach to label the cells in suspension before seeding was tested but yielded no nuclear signal (data not shown). In contrast, in parallel tested breast cancer cell line MDA-MB-231 did show nuclear staining (not shown). Lastly, NucSpot® Live 650, a nuclear dye advertised for long-term live cell imaging, was tested but yielded no fluorescence. Thus, all tested nuclear labels were discarded as an option for C17.2 tracking.

In parallel, several markers to visualize the cellular body were tested. Fluorescein diacetate (FDA) is commonly used as a viability probe as it fluoresces upon intracellular enzymatic activity. It absorbs in the green spectra and yields a cytoplasmic staining. Concentration of 50 μg/ml generated strongly labelled cells but impacted their health and lead to plasma membrane blebbing - a characteristic of injured cells - and cell death (data not shown). Lower tested concentrations did not produce a sufficiently strong signal. Additionally, upon laser exposure the dye bleached visibly within seconds.

NeuroFluor™ CDr3, a red fluorescent dye selectively labelling neural progenitor cells, was also tested. The staining was successful visualizing the cell cytoplasm (Figure 4.2 d). However, the label was not distributed homogeneously throughout the cell, thus making it difficult to distinguish the cell contours. Furthermore, time-lapse imaging resulted in fast bleaching of the dye within 2 h.

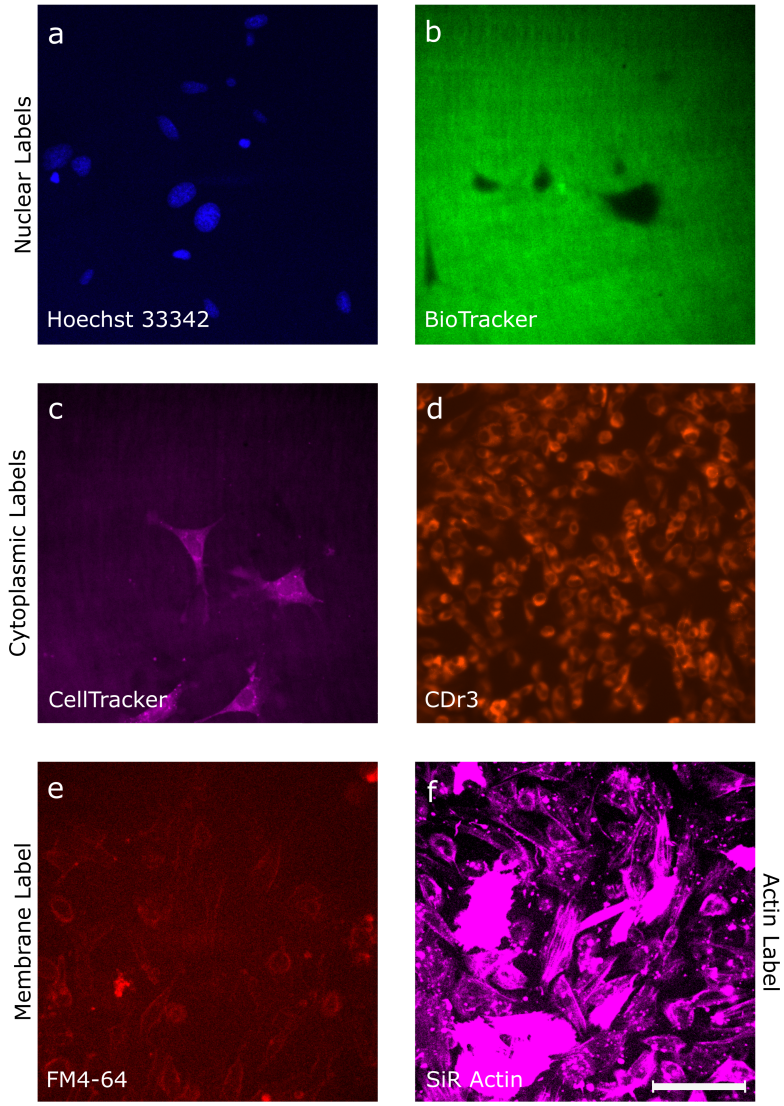

Figure 4.2: Testing of various fluorescence labels with C17.2 cells. Testing of various fluorescence labels with C17.2 cells. The nuclear label Hoechst 33342 produced a clear but partially weak signal (a), whereas BioTracker adsorbed to the laminin surface and failed to label cell nuclei (b). The cytoplasmic label CellTracker produced an insufficiently strong fluorescence with background noise (c), whereby the fluorescence of neural progenitor label CDr3 was not homogeneously distributed throughout the cell body (d). FM4-64 produced only a weak staining of the cell membrane (e). SiR Actin produced heterogeneous fluorescence intensity among cells with insufficiently clear actin label and dye clumping (f). Scale bar for (a-f) is 100 μm.

Next, CellTracker™ Deep Red Dye (ThermoFisher) is advertised as a multigenerational tracking dye with retention times above 72 h and non-toxic to cells. Along with its absorption maxima at 630 nm, it made an interesting candidate for planned experiments. However, the produced signal was very low with some accumulation of the dye around the nucleus and partial adsorption to the substrate (Figure 4.2 c). Testing different concentrations and incubation times, as well as labelling the cells in suspension before seeding did not change the outcome.

FM™ 4-64 Dye (ThermoFisher) was considered as an alternative as it is visualizing cell contours although it has a broad absorption spectrum between 300 - 600nm (maximum at 515nm) and short retention times of only several hours. It is a lipophilic dye staining cellular membrane and commonly used to study endocytic pathways. But this dye did not produce a sufficiently strong signal at 20x magnification and thus was also discarded as a label.

The optimal way to visualize the cell body for the experiments was considered to be a label of the cytoskeleton protein actin. However, availability of actin labels for living cells is still limited due to its dynamic nature that makes it highly challenging to produce a label which does not interfere with its polymerization. SiR actin (tebu-bio) is based on the fluorescent silicon rhodamine (SiR) and is advertised as showing high labelling specificity of F-actin in live cells with low background. With its absorption maxima at 652 nm it was a promising candidate. The manufacturer advises to use concentrations below 100 nM for time-lapse imaging to avoid interference of the probe with actin. Labelling produced a highly heterogeneous signal among individual cells as well as within the cell. Figure 4.2 f shows several over-exposed cells while other exhibit a weak signal. Also, the actin visualization within the cell was suboptimal with localized higher and lower signal intensity. Different concentrations and incubation times have been tested, but none yield a satisfactory result (data not shown). Thus, also this label was discarded as an alternative.

In summary, several commercially available fluorescence markers have been tested on C17.2 but none produced an effective labelling. Although fluorescent labels have revolutionized cell research, their success still faces challenges. A label needs to be cell-membrane permeant, specifically bind to the region of interest, show only fluorescence when specifically bound, not impair cell function, have a sufficient retention time within the cell, exhibit high fluorescence intensity, be photostable, and have a homogeneous distribution among and within cells. Generally, the response to exogenously introduced chemicals and proteins can vary among different cell types and even cell cultures established in different laboratories, thus complicating their application. Another reason for the failed fluorescence dye labelling could be high activity of transmembrane efflux pumps. Nestin-positive neural stem cells were found to express transmembrane ABC-transporters [28], which actively pump out toxins and other molecules from the cell interior. Additionally, C17.2 NSCs were found to be more sensitive to neurotoxins compared to other neural cell lines. This information coupled with our observations suggests that C17.2 cells can be challenging to label using fluorophore dyes and thus require other labelling methods.

4.2.3. DUAL-TRANSDUCTION WITH NUCLEAR AND ACTIN LABEL

An attractive alternative to using fluorescent dyes is to introduce genes coding for fluorescent proteins into the cellular genome. A transfection (non-viral) or transduction (viral) can also lead to impairment of cellular functions as it integrates exogeneous genes randomly into the cellular genome and thus can disrupt DNA transcription. The clear advantage of this method is the generation of cells which continuously express fluorescent molecules bound to the protein of interest, thus circumventing many complications which fluorescent dyes show. As non-viral transfection is known to be inefficient in neural progenitor cells and can be toxic [29, 30], the commercially available BacMam 2.0 transduction system was tested on C17.2 cells. BacMam uses a modified insect virus (baculovirus) which is advertised to be ready-to-use and produce a transient protein expression for up to 5 days. The systems CellLight™ Nucleus-RFP and CellLight™ Actin-GFP were tested with different protocol parameters, however no labelling signal was achieved (data not shown).

As published data showed successful transduction of C17.2 cell using a lentiviral vector [31, 32], this method was selected to eventually obtain a stable cell line with bright and homogeneous nuclei and actin labels. Lentiviral transduction demands higher safety measures and GMO-approval, as well as several weeks of time to establish a transduced cell line. Thus, this method was only selected after the possibility of using fluorescence dyes was ruled out.

For the nuclear label, the commercial product IncuCyte® NucLight™ Red Lentivirus Reagent (EF-1 Alpha, Puro) from Essen BioScience was purchased. It is advertised to produce a homogeneous expression of a nuclear-restricted red fluorescent protein, mKate2. The result was a 100% transduction efficiency showing a uniform and strong fluorescence signal of mKate2 (see signal distribution in Figure 4.3 c). For the dual label, the nuclear-labelled cells were transduced with an in-house lentivirus reagent by Dr. Sylvia de Dévédec (LACDR), expressing GFP lifeact. Lifeact is a marker visualizing the cytoskeletal element F – actin, without interfering with its dynamics [33]. The result was a high-efficiency transduction but with a heterogenous signal intensity (Figure 4.2 a, c). Furthermore, as both vectors incorporated a puromycin resistance for selection, many cells showed either the nuclear or the actin label (Figure 4.2 a).

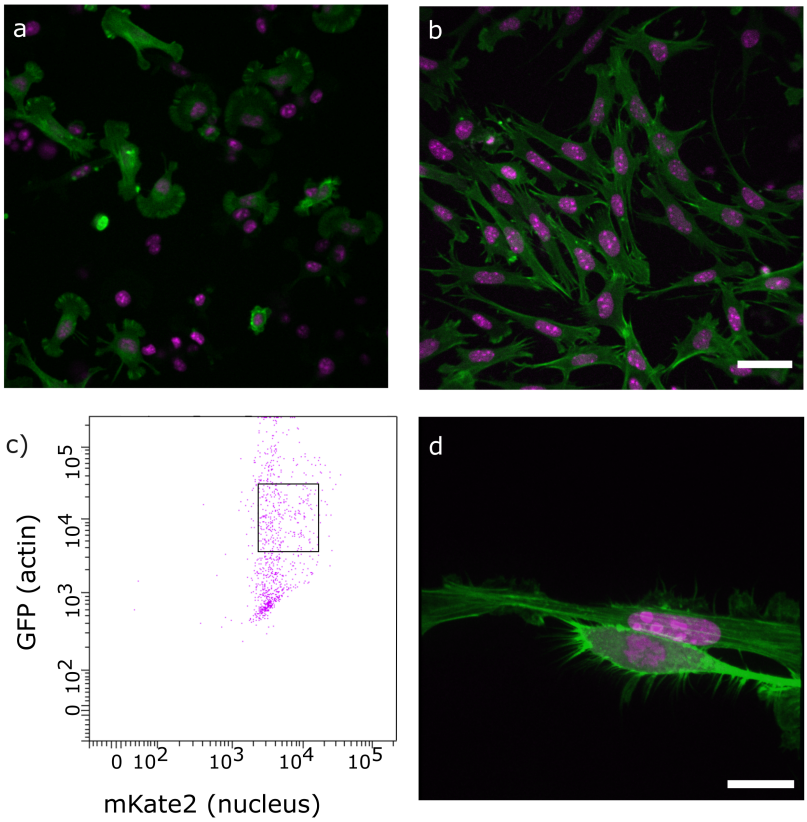

Figure 4.3: Dual-transduced nuclear- and actin-labelled C17.2 cells. Dual-transduced nuclear- and actin-labelled C17.2 cells. Dual-transduction produced a heterogeneous intensity of GFP-lifeact among cells with homogeneous fluorescence of mKate2-nucleus label, whereby several cells exhibited only one of the two labels (a). FACS data confirmed the presence of broad GFP fluorescence intensity and narrow mKate2 fluorescence intensity distribution (c); each point equals one cell. Black square shows the fluorescence parameters of the cell population selected for sorting. After FACS sorting and clone selection, 100 % of the cell population expressed double labels for actin and nuclei with homogeneous and strong fluorescence among (b) and within cells (d).

To obtain a pure culture of dual-labelled cells showing a homogeneously high fluorescence signal, Fluorescence-Activated Cell Sorting (FACS) was performed. Hereby, the fluorescence signal for a sample of the cell population is measured and cells expressing the desired signal intensity can be selected for further culture. The rest will be discarded. Figure 4.2 c shows the homogeneous signal intensity for mKate2 (nucleus) and the broadly heterogeneous signal distribution for GFAP (actin). The black square represents the parameter window for signal intensity based on which individual cells were selected for further culture. To establish a monoclonal cell line exhibiting the same location of gene insertion, FACS equipment was programmed to select single cells and direct

them into single wells of a 96-well plate with a feeder-layer. Feeders are growth-arrested cells which condition the media and thus enable an individual cell to survive and proliferate. A cell in isolation without conditioned media by its neighbours or feeder-cells would undergo growth arrest or cell death. The individual C17.2 cells were observed in culture over the following weeks. As the location and number of the inserted genes is not controlled, many monoclonal cell populations exhibited failed proliferation or changed morphology. Eventually one clone was selected based on its normal morphology and proliferation characteristics, as well as homogeneous and strong fluorescence signal of both labels (Figure 4.2 b). A close-up of two cells supports the homogeneous distribution of the nucleus and actin-bound fluorophores (Figure 4.2 d). This transduced monoclonal cell line was expanded and used for experiments shown in this thesis.

4.2.4. CONCLUSIONS

This chapter introduced the multipotent neural progenitor cell line C17.2 and confirmed its immature state as well as its capacity for neural differentiation. Additionally, a range of commercial fluorescent dyes has been tested to find a suitable nuclear and cell body label for fluorescence time-lapse imaging, but none produced a sufficient result. Lastly, viral transduction has been successfully employed to establish a monoclonal cell line with a homogeneous and strong fluorescence signal within the nucleus and actin of C17.2 neural progenitors. Although cell morphology and proliferation suggested no visible interference with cellular function, viral transduction can negatively affect neural differentiation [29] and should still be tested for.

4.3. MATERIALS AND METHODS

4.3.1. CELL CULTURE

C17.2 cells (Merck, 07062902) were maintained in plastic p60 (9cm^2)) plastic culture dishes in 5 mL Dulbecco's Modified Eagle Medium with phenol red (DMEM; Sigma), supplemented with 2 mM Glutamine (Gibco), 10% fetal calf serum (FCS; Biowest), 100 U/mL penicillin and streptomycin (P/S; Duchefa) under standard culturing conditions (humidified, 37 °C atmosphere containing 5.0% CO2). Culture dishes were pre-coated with 1-2 μg/mL laminin (Merck, L2020) in DMEM for at least 1 h in the incubator at 37 °C. For poly-l-lysine (PLL) coating, dish was covered with 10 μg/ml PLL (Sigma, P6282) in sterile distilled water for 5 min at room temperature. Then the solution was removed, and the dish dried with an open lid in the sterile hood for at least 1 h. Cells were split every 3-4 days when reached confluency of 80 - 90% and seeded 1 - 2 x 105 cells per p60 dish. Cells were cultured for up to 25 passages.

4.3.2. CELL DIFFERENTIATION

For neural differentiation, cells were seeded on laminin-coated dishes with 5 x 103 cells per cm2 in complete growth medium. On the next day, cells were washed twice with Phosphate Buffered Saline (PBS; Merck) and differentiation media added. Differentiation media consisted of DMEM : F12 (ThermoFisher) with N2 supplement (Invitrogen,

17502-048), 10 ng/ml brain-derived neurotrophic factor (BDNF; R&D systems, 248-BDB) and 10 ng/ml nerve growth factor (NGF; Merck, N6009). Media was refreshed every second day. Protocol is based on publication by Lundqvist *et al.* (2013) [19].

4.3.3. IMMUNOFLUORESCENCE (IF)

Cells were cultured on laminin-coated 8-chambered microscopy slides (ibidi, 80821). For this, uncoated (hydrophobic) μ-Slide 8 Well (ibidi, 80821) were exposed to UV for 30 min and incubated with laminin as described for regular cell culture above. For IF, cells were washed 2x with PBS and fixed for 10 min using 4% paraformaldehyde (PFA; Gibco). After 2x washing steps with PBS, cells were permeabilized with 0.1% TritonX for 5 min. Washed twice with PBS and incubated for 1 h in blocking buffer (1% bovine serum albumin (BSA; Gibco) and 0.3% Triton X (xxx) in PBS). Primary antibodies were diluted in blocking buffer as followed: Nestin (BioLegend, 839801) 1:1000, βIII-tubulin (BioLegend, MMS-435P) 1:1000, GFAP (Merck, HPA056030) 1:500. Cells were incubated with primary antibody solution overnight at 4 °C and washed 3x with PBS. Secondary antibodies were diluted in blocking buffer as followed: Alexa 488 goat anti-rabbit (ThermoFisher, ♯A-11034) 1:500, Alexa 568 anti-mouse (Abcam, ab175701) 1:500. Cells were incubated with secondary antibodies for 1 h at room temperature in the dark. After three washing steps with PBS, the cells were ready to be imaged.

4.3.4. FLUORESCENCE DYE LABELLING

For all labelling tests, cells were grown on laminin-coated 35 mm μ-Dishes (ibidi, 81151). For this, uncoated μ-Dishes were exposed to UV for 30 min and incubated with laminin as described for regular cell culture above. All protocols were repeated at least twice. All incubation steps were performed at 37°C in the dark.

Hoechst 33342 (ThermoFisher, 62249)
Cells were washed twice with PBS and incubated with 5 μM Hoechst 33342 in complete media for 30 min in the incubator. Then, cells were washed again twice with PBS and covered with complete media.

BioTracker™ Nuclear Dye (Merck, SCT120)
Cells media was removed, cells covered with BioTracker solution (diluted 1:1000 and 1:500 in culture medium) and incubated for 10 - 30 min at 37°C and imaged. Alternatively, trypsinized cells were incubated in a falcon tube with the BioTracker solution for 20 min, centrifuged, resuspended in fresh media, and seeded onto a laminin-coated dish.

NucSpot® Live 650 (Biotium, 40082)
Cell media was removed, cells covered with NucSpot solution (diluted 1:1000 and 1:500 in culture medium) and incubated for 10 - 30 min at 37°C and imaged. Alternatively, trypsinized cells were incubated in a falcon tube with the NucSpot solution for 20 min, centrifuged, resuspended in fresh media, and seeded onto a laminin-coated dish.

CellTracker™ Deep Red Dye (ThermoFisher, C34565)
Cells were washed with PBS and incubated with CellTracker solution (250 nM, 1 μM, 5μM, and 25 μM in serum-free culture medium) for 15-45 min. Then staining solution was removed and cells covered in complete culture medium. Alternatively, trypsinized cells were incubated in a falcon tube with the CellTracker solution for 30 min, centrifuged, resuspended in fresh media, and seeded onto a laminin-coated dish.

Fluorescein Diacetate (FDA; Merck, F7378)
Cells were washed with PBS and incubated with 20 μg/ml and 50 μg/ml FDA solution. Cells were ready to be imaged almost immediately.

FM4-64 (ThermoFisher, T13320)
FM™ 4-64 Dye (N-(3-Triethylammoniumpropyl)-4-(6-(4-(Diethylamino) Phenyl) Hexatrienyl) Pyridinium Dibromide). Cells were washed with PBS and incubated for 10 min in FM4-64 staining solution (2 μg/ml and 5 μg/ml in cell medium).

SiR Actin (Tebu-bio, SC006)
Cells were covered with SiR staining solution of 100 nM and 1 μM diluted in cell medium. Also, the addition of 10 μM verapamil (efflux pump inhibitor) was tested. After incubation of 1 h of 1 μM, and from 6 h - 12 h for 100 nM (as advised by manufacturer) cells were imaged. For better signal-to-noise ratio staining solution has been replaced with fresh cell medium.

CellLight^{TM} Nucleus-RFP and Actin-GFP, BacMam 2.0 (ThermoFisher, C10603 and C10506)
Cells were used at 30 - 50 % confluency. BacMam solution was mixed with media to 30, 40, and 50 particles per cell (PPC) and incubated with cells for 16 h.

NeuroFluor™ CDr3 (Stemcell, ♯01800)
Cells were incubated for 1.5 h with 1 - 2 μM CDr3 solution in cell medium. Staining solution was removed, cells washed twice with PBS, and fresh medium added.

4.3.5. LENTIVIRAL DUAL-TRANSDUCTION AND FACS SORTING

Cells were seeded 24 h before and reached about 30% confluency. For the initial transduction with IncuCyte® NucLight Red Lentivirus Reagent (Sartorius, 4476), six different concentrations and combinations of the lentivirus reagent (3 - 6 MOI) with and without Polybrene (4 – 8 μg/mL) were applied and incubated overnight. Then cell media was refreshed and incubated for another 24 h. For stable cell line generation, a kill curve was performed on C17.2 cells, and the optimal puromycin concentration of 100 μg/ml determined. 48 h after transduction, cells were maintained in cell medium with 100 μg/ml puromycin. Medium was refreshed every 2 -3 days until only living cells were present, which were further cultured and expanded.

For dual-transduction, NucLight Red-transduced C17.2 cells were seeded 24 h before and reached 30% confluency for transduction. Cells were transduced with GFP-lifeact by Dr. Sylvia de Dévédec (LACDR, Leiden University) at different concentrations, and selected by culturing in cell medium with 100 μg/ml puromycin.

Fluorescence activated cell sorting (FACS) was performed at the LUMC Flow cytometry Core Facility (FCF). Cell population was sorted using GFP and mKate2 fluorescence channels. Single cells were seeded into a 96-well plate containing a layer of feeder-cells. Feeder cells consisted of mouse fibroblasts (MEFs) which were treated with mitomycin to inactivate proliferation and were seeded the day before at low concentration. Sorted C17.2 cells were growth in full medium and split when reached a confluency of 80 - 90%. Cells exhibiting normal growth rate and typical C17.2 morphology, as well as stable expression of GFP (actin label) and mKate2 (nucleus label) were expanded. Other cells were discarded.

4.3.6. FLUORESCENCE MICROSCOPY

Images of live and fixed cells were acquired on a Nikon Ti Eclipse inverted microscope (Nikon Corporation, Japan) equipped with a Yokogawa 10,000 rpm spinning disc unit (Andor Technology Ltd., United Kingdom) and a stage-top miniature incubation chamber (Tokai Hit, Japan; INUG2E-TIZ) with a TIZD35 sample holder mounted on a Nikon Ti-S-ER motorized stage. The cells were imaged using a 20x (Nikon Plan Apo WD 1.0, numerical aperture (NA) 0.75), or a 60x (Nikon Oil Plan Apo λ, NA 1.4). An Agilent MLC400B monolithic laser combiner (AgilentTechnologies, Netherlands) was used for excitation at 405 nm, 488 nm, 561 nm, and 640 nm in combination with a Semrock custom-made quad-band dichroic mirror for excitation wavelengths 400 – 410, 486 – 491, 460 – 570, and 633 – 647 nm. The emission was filtered using a Semrock quad-band fluorescence filter (TR-F440-521-607-700), which has specific transmission bands at 440 ± 40 nm, 521 ± 21 nm, and 607 ± 34 nm, or otherwise a Semrock TR-F447-060 for λexc = 405 nm or a Semrock TR-F607-036 for λexc = 561 nm. All images were captured by an Andor iXon Ultra 897 High-speed EM-CCD camera. Image acquisition was automated using NisElements software (LIM, Czech Republic).

4.4. REFERENCES

[1] Julia P Andreotti et al. “Neural stem cell niche heterogeneity”. In: *Seminars in cell & developmental biology*. Vol. 95. Elsevier. 2019, pp. 42–53.

[2] Kirsten Obernier and Arturo Alvarez-Buylla. “Neural stem cells: origin, heterogeneity and regulation in the adult mammalian brain”. In: *Development* 146.4 (2019).

[3] Paul Lu et al. “Neural stem cells constitutively secrete neurotrophic factors and promote extensive host axonal growth after spinal cord injury”. In: *Experimental neurology* 181.2 (2003), pp. 115–129.

[4] Linda Ottoboni, Beatrice von Wunster, and Gianvito Martino. “Therapeutic plasticity of neural stem cells”. In: *Frontiers in neurology* 11 (2020), p. 148.

[5] Yasushi Takagi. “History of neural stem cell research and its clinical application”. In: *Neurologia medico-chirurgica* 56.3 (2016), pp. 110–124.

[6] Joshua J Breunig, Tarik F Haydar, and Pasko Rakic. “Neural stem cells: historical perspective and future prospects”. In: *Neuron* 70.4 (2011), pp. 614–625.

[7] Brent A Reynolds and Samuel Weiss. “Generation of neurons and astrocytes from isolated cells of the adult mammalian central nervous system”. In: *science* 255.5052 (1992), pp. 1707–1710.

[8] Armine Darbinyan et al. “Isolation and propagation of primary human and rodent embryonic neural progenitor cells and cortical neurons”. In: *Neuronal Cell Culture*. Springer, 2013, pp. 45–54.

[9] Weixiang Guo et al. “Isolation of multipotent neural stem or progenitor cells from both the dentate gyrus and subventricular zone of a single adult mouse”. In: *Nature protocols* 7.11 (2012), pp. 2005–2012.

[10] Leonard Hayflick and Paul S Moorhead. “The serial cultivation of human diploid cell strains”. In: *Experimental cell research* 25.3 (1961), pp. 585–621.

[11] Gabriel Bretones, M Dolores Delgado, and Javier León. “Myc and cell cycle control”. In: *Biochimica et Biophysica Acta (BBA)-Gene Regulatory Mechanisms* 1849.5 (2015), pp. 506–516.

[12] Ana Villa et al. “Establishment and properties of a growth factor-dependent, perpetual neural stem cell line from the human CNS”. In: *Experimental neurology* 161.1 (2000), pp. 67–84.

[13] Susan J Birren and David J Anderson. “A v-myc-immortalized sympathoadrenal progenitor cell line in which neuronal differentiation is initiated by FGF but not NGF”. In: *Neuron* 4.2 (1990), pp. 189–201.

[14] Minoru Hoshimaru et al. “Differentiation of the immortalized adult neuronal progenitor cell line HC2S2 into neurons by regulatable suppression of the v-myc oncogene”. In: *Proceedings of the National Academy of Sciences* 93.4 (1996), pp. 1518–1523.

[15] Elizabeth F Ryder, Evan Y Snyder, and Constance L Cepko. “Establishment and characterization of multipotent neural cell lines using retrovirus vector-mediated oncogene transfer”. In: *Journal of neurobiology* 21.2 (1990), pp. 356–375.

[16] Alberto Martínez-Serrano and Anders Björklund. “Immortalized neural progenitor cells for CNS gene transfer and repair”. In: *Trends in neurosciences* 20.11 (1997), pp. 530–538.

[17] Evan Y Snyder et al. “Multipotent neural cell lines can engraft and participate in development of mouse cerebellum”. In: *Cell* 68.1 (1992), pp. 33–51.

[18] Booma D Yandava, Lori L Billinghurst, and Evan Y Snyder. ““Global” cell replacement is feasible via neural stem cell transplantation: evidence from the dysmyelinated shiverer mouse brain”. In: *Proceedings of the National Academy of Sciences* 96.12 (1999), pp. 7029–7034.

[19] Jessica Lundqvist et al. “Optimisation of culture conditions for differentiation of C17. 2 neural stem cells to be used for in vitro toxicity tests”. In: *Toxicology in Vitro* 27.5 (2013), pp. 1565–1569.

[20] Kristina Attoff et al. “Whole genome microarray analysis of neural progenitor C17. 2 cells during differentiation and validation of 30 neural mRNA biomarkers for estimation of developmental neurotoxicity”. In: *PloS one* 12.12 (2017), e0190066.

[21] Jessica Lundqvist et al. “Altered mRNA expression and cell membrane potential in the differentiated C17. 2 cell model as indicators of acute neurotoxicity”. In: *Applied In Vitro Toxicology* 3.2 (2017), pp. 154–162.

[22] Bu Wang, Sabrina Jedlicka, and Xuanhong Cheng. “Maintenance and neuronal cell differentiation of neural stem cells C17. 2 correlated to medium availability sets design criteria in microfluidic systems”. In: *PLoS One* 9.10 (2014), e109815.

[23] Wei-Guo Liu et al. “Dopaminergic neuroprotection by neurturin-expressing c17. 2 neural stem cells in a rat model of Parkinson’s disease”. In: *Parkinsonism & related disorders* 13.2 (2007), pp. 77–88.

[24] Yajie Liang et al. “Neural progenitor cell survival in mouse brain can be improved by co-transplantation of helper cells expressing bFGF under doxycycline control”. In: *Experimental neurology* 247 (2013), pp. 73–79.

[25] Aurora Bernal and Lorena Arranz. “Nestin-expressing progenitor cells: function, identity and therapeutic implications”. In: *Cellular and Molecular Life Sciences* 75.12 (2018), pp. 2177–2195.

[26] AJI Roskams, X Cai, and GV Ronnett. “Expression of neuron-specific beta-III tubulin during olfactory neurogenesis in the embryonic and adult rat”. In: *Neuroscience* 83.1 (1998), pp. 191–200.

[27] L_F Eng et al. “An acidic protein isolated from fibrous astrocytes”. In: *Brain research* 28.2 (1971), pp. 351–354.

[28] Tingting Lin, Omedul Islam, and Klaus Heese. “ABC transporters, neural stem cells and neurogenesis–a different perspective”. In: *Cell research* 16.11 (2006), pp. 857–871.

[29] RB Tinsley, J Faijerson, and PS Eriksson. “Efficient non-viral transfection of adult neural stem/progenitor cells, without affecting viability, proliferation or differentiation”. In: *The Journal of Gene Medicine: A cross-disciplinary journal for research on the science of gene transfer and its clinical applications* 8.1 (2006), pp. 72–81.

[30] You-Chan Kim et al. “Co-transfection with cDNA encoding the Bcl family of anti-apoptotic proteins improves the efficiency of transfection in primary fetal neural stem cells”. In: *Journal of neuroscience methods* 117.2 (2002), pp. 153–158.

[31] Anna Falk et al. “Gene delivery to adult neural stem cells”. In: *Experimental cell research* 279.1 (2002), pp. 34–39.

[32] Thor Ostenfeld et al. “Neurospheres modified to produce glial cell line-derived neurotrophic factor increase the survival of transplanted dopamine neurons”. In: *Journal of neuroscience research* 69.6 (2002), pp. 955–965.

[33] Julia Riedl et al. “Lifeact: a versatile marker to visualize F-actin”. In: *Nature methods* 5.7 (2008), pp. 605–607.

5

NEURAL PROGENITOR CELLS *in vitro* MIGRATION AND BEHAVIOUR

Neural progenitor cells are in the focus of attention for treatment of neurodegenerative diseases and injuries of the central nervous system. As these cells need to migrate to the affected areas upon injection or recruitment, for successful treatments it is crucial to gain more understanding about their migratory dynamics and behaviour. In this chapter, we establish several minimalistic in vitro systems to analyse neural progenitor cells dynamics within a controlled environment and present preliminary results. On the statistical level, we observe that the cells move in a persistent random motion independent of the environment. On the case-by-case level, we observe recurrent behavioral patterns like frequent turning of direction or competing for space that results from the interaction with the environment and neighboring cells.

5.1. INTRODUCTION

Cell migration plays a pivotal role in a myriad of physiological processes, such as immune response, neurogenesis, tissue remodelling, or metastasis. In the case of brain-related disorders, migratory defects can contribute to neurological diseases like epilepsy or mental retardation [1]. Thus, uncovering the principles of cellular dynamics and interactions with neighbouring cells is crucial for our understanding of neurological disease development and their treatments. The motility of a cell is governed by a complex interplay between the cytoskeletal machinery, substrate adhesion units, and environmental sensing. While migrating *in vivo*, cells encounter multiple challenges, like physical constrictions or other cells. Deconstructing this complexity and analysing cellular dynamics and social behaviour *in vitro*, gives valuable insights and enhances our understanding of these processes [2].

One such reductionist approach uses the importance of extracellular matrix (ECM) proteins and mimics the variety of geometries *in vivo* by creating defined protein patterns on 2D substrates *in vitro*. This so called micropatterning spatially controls the adhesive regions, and thus cell attachment, and enables highly reproducible experiments for cell adhesion and migration studies. Studies using this method uncovered interesting findings in cell biology by linking the influence of ECM patterns to cell orientation, directional guidance, and differentiation [3–5]. Further, they are applied for tissue engineering and drug screening [6, 7]. Several techniques were developed to produce these microscopic ECM patterns on substrates, such as micro-contact printing (μCP) [8] and micro plasma-initiated pattern (μPIP) [9] and are employed in this chapter to produce varying geometries.

Despite the complexity of cell migration, the essence of their dynamics over long distances (>> cell body), can be captured by relatively simple mathematical equations of motion [10]. To describe individual cell migration in 2D, the most common model is the persistent random walk (PRW) model that is based on Brownian motion [11]. This model describes that on short times scales, cells display directional persistence, demonstrating a correlation of subsequent steps and ultimately meaning that cells are likely to continue walking in the direction of their previous step. On longer times scales however, in the absence of directional cues, cells display a completely random motion, corresponding to a random walk (RW) model [10]. These modes of migration can be extracted by calculating the averaged explored area over time (i.e., mean squared displacement, MSD) and fitting the models to the acquired data. This approach yields descriptive parameters like persistence time, velocities, and diffusion constant, giving insights into the overall dynamics of cells (for formulas, see section Materials and Methods 5.3).

As described in the introduction in chapter 1, neural progenitor cells (NPCs) are highly motile cells. Due to the increasing motivation to employ these cells for therapeutic purposes, it is crucial to gain more understanding about the basic mechanisms of NPC migration and behaviour. In this chapter, minimalistic systems are established to facilitate research of NPC dynamics. Next to the comparison of NPC migration on two-dimensional substrates that were uniformly coated with different ECM proteins, also micropatterning of diverse geometries is used here to constrict the motion area of NPCs and observe their response.

The dynamics of the cells are analysed by global statistics and further conclusions are

gathered by case-by-case observation. NPCs with fluorescent reporters for cytoskeleton and nuclei (for details see chapter 4) are also employed to facilitate the tracking and observational analysis. Finally, a short look is taken into a further development of the minimalistic systems to the 3D, by establishing microchannels and adding constrictions that mimic the environmental confinement NPCs experience *in vivo*.

5.2. RESULTS AND DISCUSSION

5.2.1. NPCS MIGRATION ON DIFFERENT ECM PROTEINS

In the central nervous system (CNS), various extracellular membrane (ECM) proteins are present. Their role is to structurally and biochemically support the embedded cells and provide attachment sites for migrating NPCs. Fibronectin and laminin are two prominent ECM proteins that are commonly used in *in vitro* cell culture. Here, we compared the basic migratory behaviour of NPCs on a uniform distribution of these two proteins on 2D substrates. Using fluorescence confocal microscopy, time-lapse data was collected with a frame rate of one image every 10 min for a period of 20 h.

To gain insight into the overall behaviour of NPCs, cell trajectories were gathered by tracking fluorescently labelled nuclei (for details see Materials and Methods 5.3). Cells were tracked until they divided and new tracks were started with individual daughter cells. Due to the high proliferation rate of these NPCs, the short time between two divisions lead to relatively short single trajectories. To extend these, a proliferation inhibitor was tested (i.e., RO3306 (SML0569, Sigma-Aldrich). However, this led to dedifferentiation of the cells making this option not feasible (data not shown). To acquire relevant data, trajectory lengths below 30 steps (= 5 h) were excluded from the analysis. The collected trajectories are displayed in Figure 5.1 a, with a uniform distribution of collected trajectory lengths.

Cell trajectory plots (Figure 5.1 b) display a qualitative analysis of the trajectory lengths and travel direction. On both substrates, NPCs move in all directions with a maximum radius of 100 μm. The polar plots of angle distributions (Figure 5.1 c) show a primarily even distribution of cell migration in all directions. As no chemical gradient was employed, this was the expected behaviour as cells normally do not exhibit a preference to any direction without a guiding chemical attractant or repellent.

Statistical analysis of tracking data can give more information about the migration behaviour of cells. Here, the mean squared displacement (MSD) over all trajectories was calculated and plotted over lag time (Figure 5.2 a, b). Fitting the power-law for lag times < 50 min on laminin and fibronectin, resulted in an adequate fit from which average velocities (v_0) and persistence times (τ) were extracted (insets in Figure 5.2 a, b).

The MSD fits on both substrates show that cells exhibit partly directed movement on short time scales (< 50 min), then randomness starts to dominate until the movement results in completely random motion on long time scales (> 100 min). This accurately resembles the PRW model, concluding that although on shorter time scales cells seem to move towards a particular direction, on longer time scales they just randomly explore their environment.

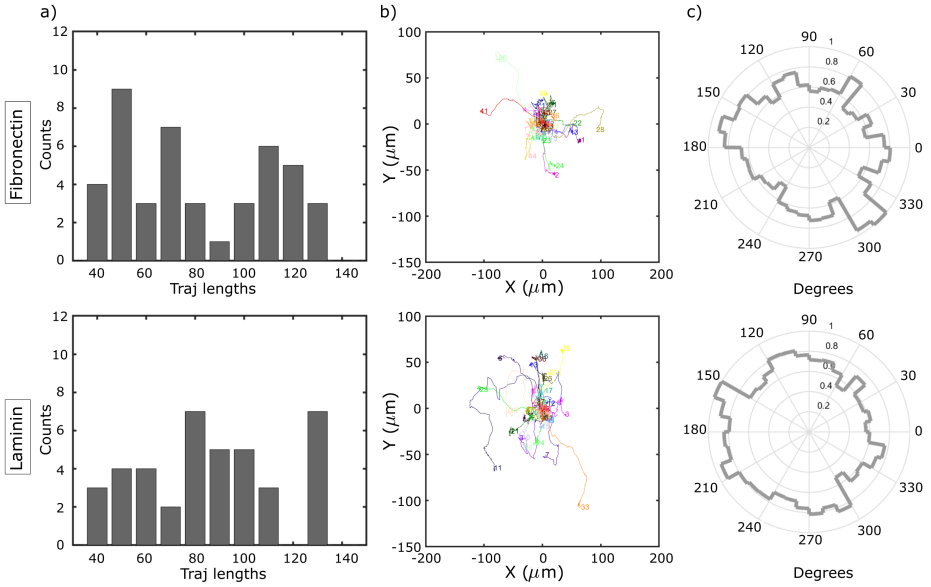

Figure 5.1: Trajectory analysis on ECM proteins. Distribution of trajectory lengths (a) displays the collected and evaluated trajectories on fibronectin and laminin. Cell trajectories plotted centred (b) and angle histogram plots (c) shows directionality of NPC migration on fibronectin and laminin into all directions.

The directional persistence (τ) time of cells characterizes the average time a cell exhibits between significant changes of direction [12]. NPCs observed here had a slightly higher persistence time on fibronectin with 48.7±7.6 min than on laminin with 43.6±2.7 min. The linear fit of the RW model yielded the diffusion constant (D_{eff}) values for cell motion on lag times over 80 min (Figure 5.2 b). Interestingly, the diffusion constants are considerably lower on fibronectin with 0.39±0.03 μm^2/min than on laminin with 1.51±0.06 μm^2/min. Likewise, the approximated average velocity (v_0) for fibronectin with 0.13±0.01 μm/min is almost half of the value on laminin with 0.27±0.01 μm/min (Figure 5.2 a).

Further, instantaneous velocity was calculated, and their respective frequencies were plotted (Figure 5.2 c). The average instantaneous velocity (v) on fibronectin (0.177±0.006 μm/min) was much lower than on laminin, however with a narrow distribution around this value. On laminin, the velocity is almost double with 0.304±0.009 μm/min, but the value distribution is slightly broader here. Comparing the average velocity approximated via the MSD fit (Figure 5.2 a, LN = 0.27±0.01 μm/min, FN = 0.13±0.01 μm/min) with the measured average velocity (Figure 5.2 c), gives a good indication of the accuracy of the fit and supports our results.

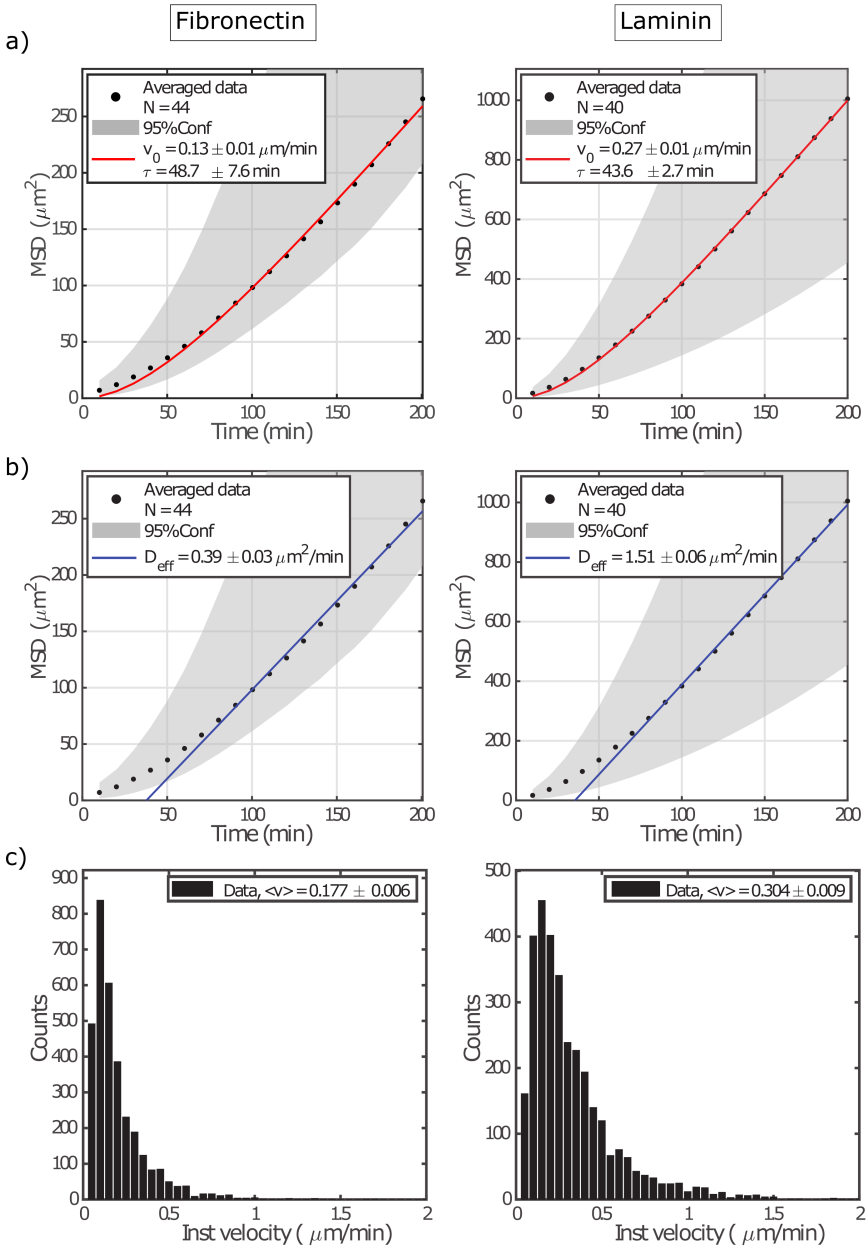

Figure 5.2: NPCs migration on ECM proteins. Mean-squared displacement (MSD) plots of NPC trajectories on fibronectin and laminin with power-law fitted as function of time (a) and linear fit (b) to extract the diffusion constant. Grey area represents the 95% confidence interval of the average of MSDs of all individual trajectories. Frequency distribution of instantaneous velocities and average values for fibronectin and laminin (c).

The explanation for the lower speed values on fibronectin might be explained by an influence of ECM proteins on cell motion. However, the reason here might also be an experimental error in the fibronectin coating. To firmly confirm the cause of the observed difference repetition of these experiments is needed. Interestingly, although the diffusion constant and the velocity are lower on fibronectin, the persistence time is comparable to laminin. Thus, although the fibronectin coating seems to affect cell attachment and thus the speed that the cells can move with, it does not impact the time during which the NPCs are moving in one direction.

CONCLUSIVE BULLET POINTS

Here the results of the current subchapter are summarized:

- NPC migration on uniform laminin and fibronectin substrates can be described by the PRW model
- On laminin, NPCs moved faster compared to fibronectin, with higher average velocities (LN: 0.304±0.009 μm/min, FB: 0.177±0.006 μm/min) and diffusion coefficients (LN:1.51±0.06 μm^2/min, FB: 0.39±0.03 μm^2/min)
- On fibronectin, the persistence times were slightly higher (48.7±7.6 min) than on laminin (43.6±2.7 min)

5.2.2. MIGRATION ON PATTERNED LINES

NPCs use ECM scaffolds, blood vessels, and glia cells as guiding structures while migrating in the brain [13, 14]. Due to the compact environment, NPCs can be constricted to tube-like spaces during migration. To approach the complex *in vivo* situation in a simplified way, line patterns of ECM proteins can be deposited on a two-dimensional (2D) surface, confining the cells to one dimension. Pluronic F-127 is a chemical that was shown to prevent cell attachment [15] and is often employed to enhance selective adhesions of cells to the applied ECM pattern.

Employing micro-contact printing (μCP), we generated fibronectin lines with deposited Pluronic F-127 in the interspaces. To explore the influence of small geometrical variations on NPC dynamics, we created varying line widths of 10 μm (L 10), 15 μm (L15), 20 μm (L 20), and 25 μm (L25). As expected, NPCs aligned on all lines with a broader expansion on lines with increasing width (Figure 5.3). Notably, the ability of cells to align on topographical patterns is important in various physiological contexts [16, 17], known as contact guidance [18]. This phenomenon was reproduced *in vitro* using different patterning techniques [19].

Occasionally, the μCP method did not result in uniform ECM printing (Figure 5.3 c, arrow), whereby the imperfect lines were mostly missing the pattern in its centrum. Thus, the cells could still align to the edges of the pattern, taking up the full line width (Figure 5.3 c), and were thus considered as successfully aligned. However, patterning of the L15 yielded many lines with only a thin pattern on one side. As a high number of lines was still intact, the data is incorporated into the analysis and consequences of the ineffective pattern are pointed out in the respective results section.

To analyse NPC dynamics on the different lines, fluorescence time lapse microscopy was performed for 22h and images collected every 10 min.

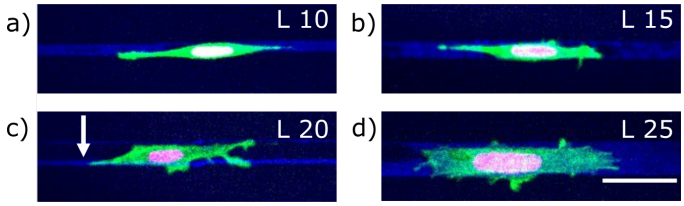

Figure 5.3: NPC alignment on fibronectin lines. NPCs stretch out (both in cell body and nucleus) and align on all patterned lines showing a broader morphology with increasing width (from a to d). Scale is 50 μm.

STATISTICAL ANALYSIS

Statistical analysis of NPC migration was performed on patterned lines as in section 5.2.1 and yielded insights into global behaviour under one-dimensional confinement. As before, trajectory lengths below 30 steps were excluded from the analysis, yielding a uniform distribution of trajectory lengths (Figure 5.4 a). As expected, direction of movement was highly constricted to the x-axis on L10 and shows increasingly more movement into y-direction on wider L25 (Figure 5.4 b). The maximum walked distance in x-direction was 200 μm (Figure 5.4 b) and thus longer than without confinement (section 5.2.1). Angle histograms are illustrating the motion constriction to x-direction and the slight additional range of motion that cells experience on wider lines (Figure 5.4 c).

Global MSD calculations with subsequent PRW and RW fits were applied (as in section 5.2.1) to gather data about the overall NPC dynamics on pattered lines. Both fits accurately followed the calculated data points for all line widths, except for L15. Here, the PRW fit is more linear than exponential at short lag times (Figure 5.5 a, L15), and the RW fit aligns with the data points earlier (Figure 5.5 b, L15) compared to the other line widths (Figure 5.5 b). This alignments suggests a low persistence and mainly random motion on L15, as can also be seen on the calculated persistence time (τ) (Figure 5.5 a, L15, inset) that is about half the value of the persistence times on the other lines.

These result might be explained by the ineffective patterning of L15 as was pointed out above. Additionally, at the start of the experiment, the cells on L15 were present in a slightly higher number (L15 = 55 cells) compared to other lines (L10 = 42 cells, L20 = 50 cells, L25 = 28 cells). These two conditions together probably created obstacles for the NPCs and inhibited movement into one direction for longer times. As NPCs encountered the discontinuity in pattern and/or other cells more frequently on L15 than on other lines, this resulted more often in the interruption of their moving direction, yielding the considerably lower persistence time value.

On lines L10, L20, and L25 the persistence times of motion are fairly similar with 19.7±1.2 min, 25.3±2.7 min, and 20.9±2.8 min, respectively (Figure 5.5 a). However, on L20 the persistence time is the highest with 25.3±2.7 min. Interestingly, also the velocity has the highest value on L20 compared to the other lines (Figure 5.6 c). A hypothesis to explain this result might be that a width of 20 μm provides a good balance between contact guidance and sufficient space for proper cell attachment and movement, thus facilitating faster and more directional migration of NPCs. In comparison to uniform substrates (LN: 43.6±2.7 min, FB: 48.7±7.6 min), the persistence times are considerably lower. This can be due to several reasons. NPCs are here restricted to one dimensional movement which leaves them with a binary decision to go either left or right. The confinement leads to the inevitability of encountering other cells in the way, forcing the NPCs to change their directed motion. In contrast, on the uniform substrates NPCs have all degrees of freedom to move in any direction for longer times.

Another explanation might be rooted in the confinement of the cells, which changes the physical dimensions of the system to nearly 1D and thereby also the associated equations. This influences the values found for both, the persistence time and diffusion constant in the PRW and RW fits, but not the velocities (as this is independent of the dimensionality). Interestingly, the persistence times on lines are about half the values compared to the times on 2D laminin. By adjusting the equations to 1D (for details see Materials and Methods section 5.3), the calculated persistence times would be 39.4±2.4 min, 50.6±5.4 min, and 41.8±2.8 min for L10, L20, and L25, respectively, which are more comparable to the value on 2D laminin with 43.6±2.7 min (section 5.2.1, Figure 5.1). The calculated diffusion coefficients on L10, L15, L20, and on L25 are 0.9±0.01 μm^2/min, 0.98±0.02 μm^2/min, 0.99±0.03 μm^2/min, and 0.90±0.01 μm^2/min, respectively (Figure 5.5 b). Again, finding the highest motion value for L20, like in our previous observations, these results support a facilitation of the NPCs migration on lines of 20 μm width. Notably, the ineffective patterning of L15 and the higher cell number did not influence the inherent motion of NPCs (like it did for the persistence time), as the velocity and the diffusion values do not diverge from the values on other lines.

Figure 5.4 ***(following page)*****: Trajectory analysis on fibronectin lines.** a) Left column, distribution of trajectory lengths displays the collected and evaluated trajectories on L10, L15, L20, and L25 lines. b) Middle column, spatial plots of cell trajectories showing the directionality and range of NPC movement. Note, the X and Y axis differ in scale by about 10-fold. c) Right column, angle histogram plot displaying restricted cell movement to the X plane and increasing movement in the Y plane with wider lines (from L10 to L25).

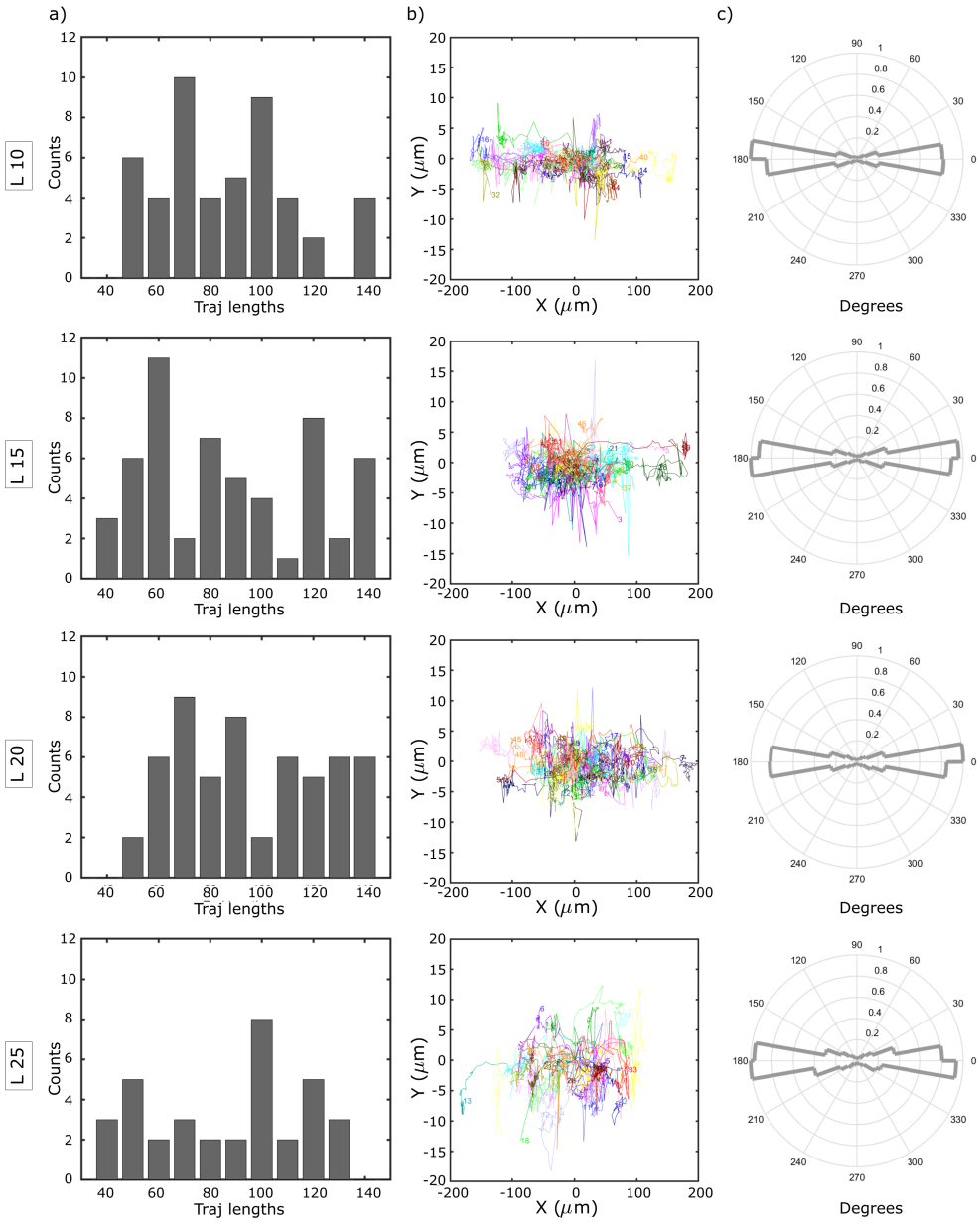
a)
b)
c)
L 10
L 15
L 20
L 25
Counts
Traj lengths
Y (μm)
X (μm)
Degrees

Taking into account the one-dimensionality (1D) of the lines and adjusting the formulas also in this case (for details see Materials and Methods 5.3), leads to diffusion constants of 1.79±0.01 μm^2/min, 1.96±0.04 μm^2/min, 1.98±0.06 μm^2/min, and 1.80±0.02 μm^2/min for L10, L15, L20, and L25, respectively. These results are comparable to uniform laminin with 1.51±0.06 μm^2/min but lie above its value. Thus, the 1D values, collected on lines, are not a perfect half of the 2D value, collected on plain surfaces. This can be explained by the fact that this is a biological system that we observe and not an ideal system, yielding an environment in which the NPCs have still some freedom in movement on the lines and beyond, thus influencing the calculated values.

The velocity values on the lines are similar with 0.284±0.008 μm/min, 0.304±0.009 μm/min, 0.268±0.008 μm/min, and 0.28±0.1 μm/min for L10, L15, L20, and L25, respectively (Figure 5.6. These values lie within the range of published mean velocity values (0.1 - 1 μm/min) that were collected in a World Cell Race with 54 different cell types, performed on printed 4 μm and 12 μm lines [20]. Compared with the tested highly migratory cell types, NPCs correspond to the rather slow-moving cells.

Comparing the velocities on lines to the velocities gathered on plain 2D surfaces (section 5.2.1), the averaged velocity values are comparable to the value on laminin substrate (0.304±0.009 μm/min, Figure 5.2). Coming back to the velocity results on plain fibronectin surface, whereby an experimental error in deposing the protein might have caused the lower value, another point would be interesting to consider here. Assuming, that the motion of uniform fibronectin was indeed slower than on uniform laminin, but the velocity values on fibronectin lines are comparable to the values on uniform laminin, using unidirectional lines might have increased cell velocity. In previous studies it has been shown that contact guidance by topographical cues does enhance the migration velocity compared to migration on a uniform substrate [21]. To make a valid conclusion in this case, additional experiments are needed to exclude experimental errors and additionally generate patterned laminin lines to compare the data comprehensively.

Figure 5.5 ***(following page)*****: Cell migration of NPCs on fibronectin lines.** Mean-squared displacement (MSD) plots of NPC trajectories on L10, L15, L20, and L25 lines. a) Power-law is fitted (red) to the MSDs as a function of time displaying persistence times (τ) and approximated velocities (v_0). b) A linear fit (blue) to the MSDs (middle) to extract the diffusion constant. Grey area represents the 95% confidence interval of the average of MSDs of all individual trajectories.

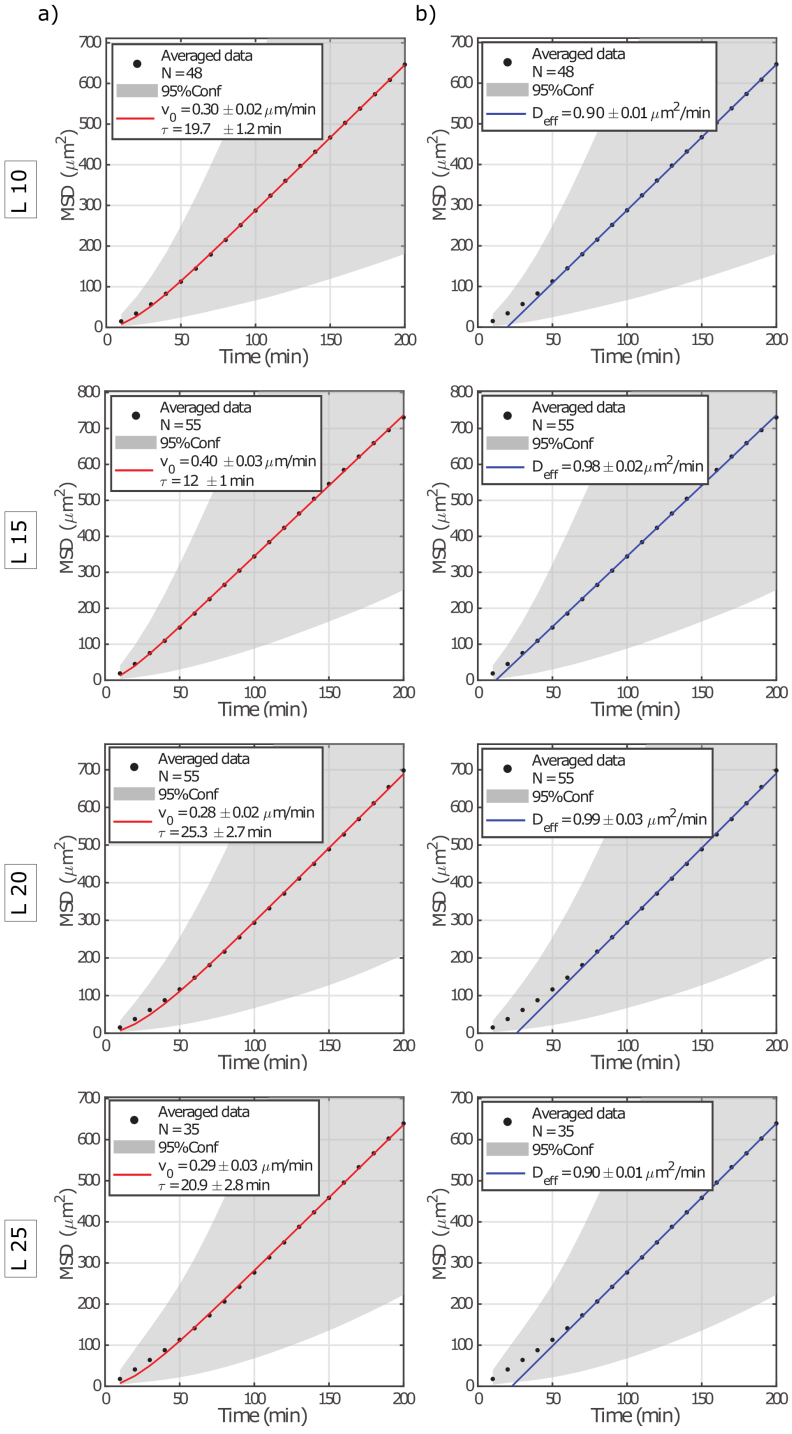
a)
b)
L 10
L 15
L 20
L 25
Averaged data
N = 48
95%Conf
v0 = 0.30 ± 0.02 μm/min
τ = 19.7 ± 1.2 min
Deff = 0.90 ± 0.01 μm²/min
N = 55
v0 = 0.40 ± 0.03 μm/min
τ = 12 ± 1 min
Deff = 0.98 ± 0.02 μm²/min
v0 = 0.28 ± 0.02 μm/min
τ = 25.3 ± 2.7 min
Deff = 0.99 ± 0.03 μm²/min
N = 35
v0 = 0.29 ± 0.03 μm/min
τ = 20.9 ± 2.8 min
Deff = 0.90 ± 0.01 μm²/min
MSD (μm²)
Time (min)

5

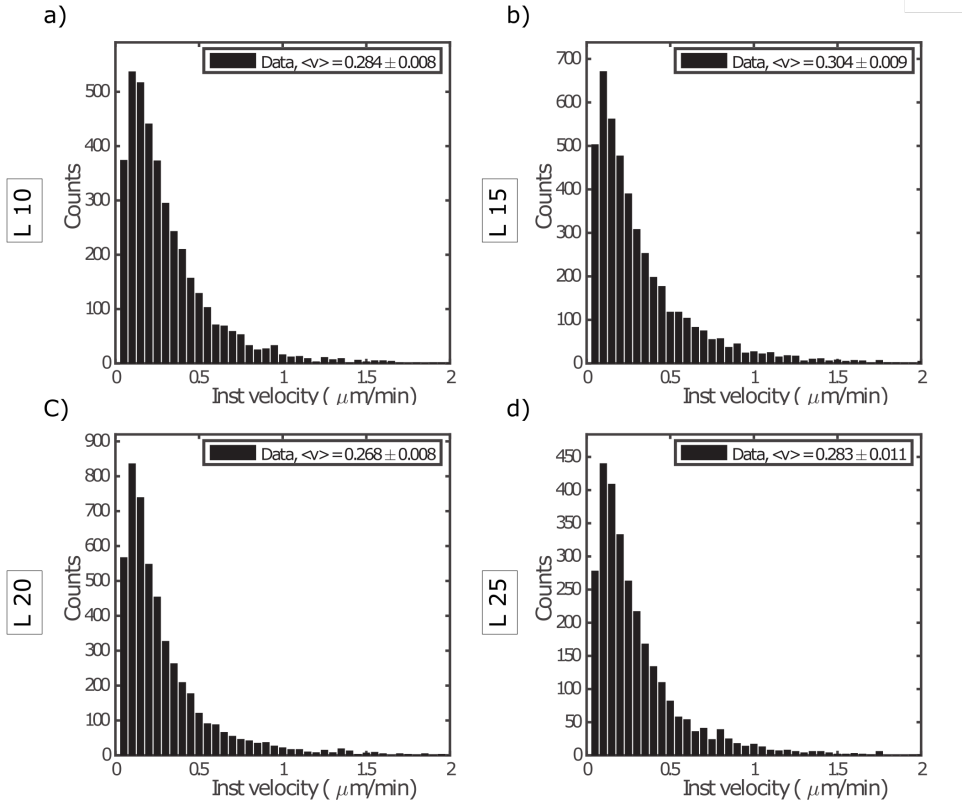

Figure 5.6: Cell migration of NPCs on fibronectin lines. Instantaneous velocity on L10, L15, L20, and L25 lines. The frequency distribution of instantaneous velocities and average values for all line widths.

VISUAL OBSERVATIONS

Statistical analysis provides useful information about NPC dynamics. However, as solely nuclei were used for cell tracking and the calculated values are averaged, it cannot capture the details of cell behaviour. By restricting NPC movement to line patterns, additional complexity was introduced to the system, making direct observation of the NPCs movement more necessary. Thus, time-lapse data was also analysed via visual observations whereby repeated behavioural patterns in NPCs were detected. These behaviours were found to occur on all lines, independent of the widths. Thus, only selected representative images are shown and discussed in this subsection.

Cell migration is a multistep action that is initiated by the polarization of the cell body, whereby the front and the rear of the cell become clearly distinguishable. The cell extends actin-based membrane protrusions at its leading edge, called lamellipodia and filopodia, which are a flat and an almost organelle-free region. The process continues with adhesion to substrate near the front edges of these protrusions, then the cell body contracts, and the cell releases the substrate adhesions at its rear end, thus moving the cell body forward (Figure 5.7) [22]. These morphological dynamics were clearly observed

in NPCs on patterned lines, thanks to an actin-GFP -reporter (Figure 5.8 a). Interestingly, NPCs were found to regularly reverse into opposite direction. Each time, cells elongated a new process into the new direction and retracted the pre-existing leading process.

In the representative image sequence, the observed cell changed its direction on the line six times within 630 min (Figure 5.8 a.) NPCs exhibited this behavioural pattern although there was no obvious obstacle like another cell or discontinuation of the line. Consistent with these results, previous observation of SVZ neuroblasts showed that they routinely change direction from a few degrees to complete reversals [23]. A previous study by Martinez-Molina *et al.* (2011) analysed in detail neuroblasts turns and direction changes in brain slices and observed an array of different turning types [24]. They found three different patterns of directional reversals, whereby the reversal in 180 °, as observed in our experiment, was the second most common form. Thus, restricting NPCs to a unilinear pattern can help to specifically research one form of directional reversals that NPCs exhibit naturally *in vivo*.

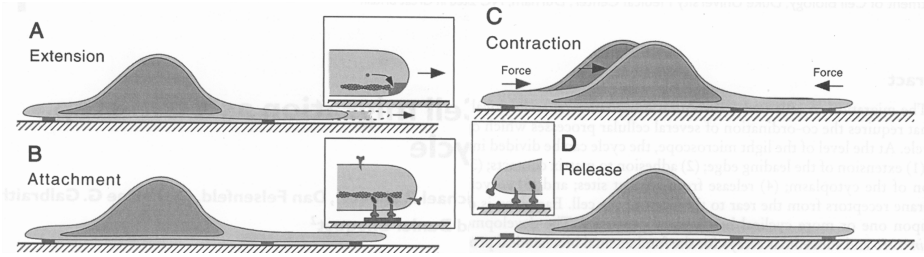

Figure 5.7: Illustration of cell migration steps.a) Extension: Assembly of actin filaments drives protrusion of cell membrane and the extension of the leading edge. b) Attachment: Focal adhesions are formed to attach the new leading edge to the substrate. c) Contraction: The cell contracts, together with Release (d) this results in forward locomotion. d) Release: Focal adhesions at the rear part of the cell are relased. Figure reprinted from Sheetz *et al.* (1999)[25]

.

Exhibiting frequent reversals and thus lacking a long-term directional persistence, these NPCs clearly exhibit “exploratory behaviour” [24, 26]). These observations support the PRW model found in the statistical analysis, showing that on short time scales cells move directionally and on long timescales their movement is random. In accordance with the observed behaviour, migrating neuroblasts in post-stroke striatum were found to spend time exploring their environment and change their direction frequently [13, 27]. This low directional migration was suggested to occur due to an insufficient production of directional cues, associated with adult mammalian’s brain low capacity for regeneration. As in our experiments no chemoattracts are employed, this resembles the observed *in vivo* situation when lacking sufficient directional cues.

Exploring the environment by changing directions and probing it with extending and retracting protrusions is crucial for cells to sample their environment and receive fine-tuned directional information. Additionally, to extending protrusions along patterned lines, NPCs often explored the interspace between the lines (Figure 5.8 b). Due to the non-adhesive substrate (Pluronic F-127) that was used to enforce specific cell attach-

ment to patterned lines, NPCs were clearly not able to adhere at the interspaces resulting in the formation of ruffles in lamellipodia (Figure 5.8 b). Membrane ruffles is a common occurrence which was found to originate when the lamellipodia failed to properly attach to substrate and consequently were retracted towards the cell body, producing a wave-like appearance [28].

At times, NPCs were observed to stretch out until the neighbouring line and "jump" over (Figure 5.9). The distance between the lines was 100 μm, showing the considerable flexibility and reach of these cells. Due to heterogeneity of ECM and microenvironment *in vivo*, cells require the ability to span over non-adhesive gaps. This so called "bridging" is crucial to achieve mechanical stability and integrity of tissue in processes like wound healing, regeneration, and development [29]. Using micropatterned lines, Buskermolen *et al.* (2020) recently analysed myofibroblasts bridging by modifying the line widths and interline spacings. They found that the cells were still able to span lines at 20 μm interspacing but not anymore at 50 μm [30]. However, interline jumps, as observed here, were not reported.

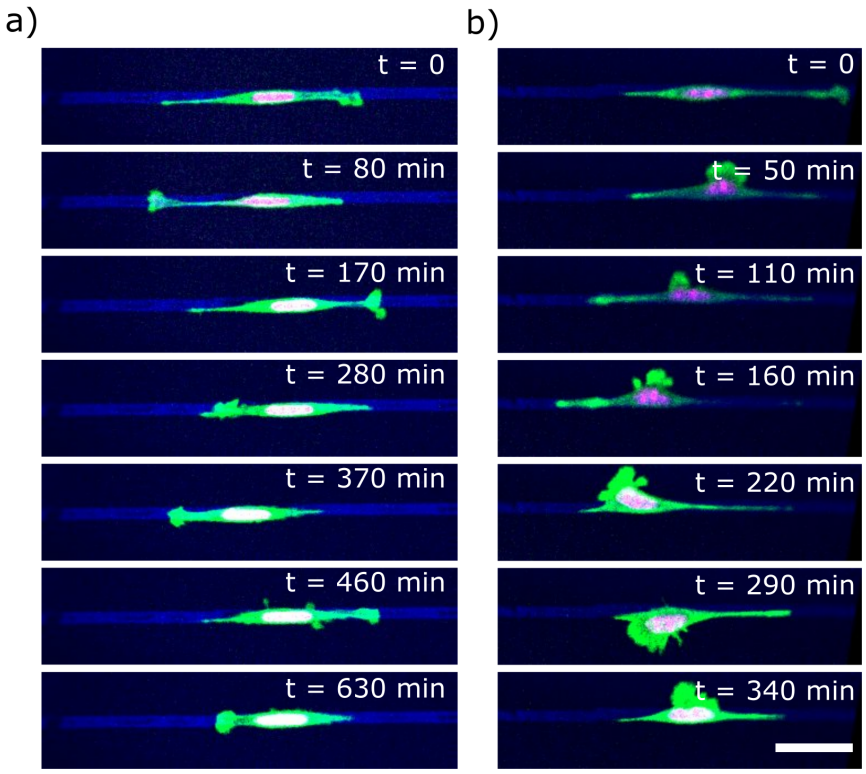

Figure 5.8: Individual NPCs exploring environment. a) Migratory shape of NPC as in Figure 5.7 with polarized cell body is frequently reversing its direction. b) NPC is extending lamellipodia into the line interspace. Scale 50 μm.

Here, it seems like NPCs were able to stretch over the non-adhesive gaps and attach their lamellipodium to another line but did not remain in a bridged state and pulled over to the other side (Figure 5.9). Comparing literature and our data it might be that a bridged state was either not possible at the large distance of 100 μm or it was simply not energy efficient for the NPCs.

Notably, jump events were less frequent on L25, than on the thinner lines. Possibly, on wider lines NPCs were able to stretch out and take up more space thus displaying less motivation to explore. As stated before, cell speed was comparable on all line widths, excluding the possibility that on L25 NPCs were less motile and thus jumped less.

Every cell divided 1 - 2 times throughout the imaging duration of 22 h. When NPCs entered mitosis, they exhibited the typical round shape, and their "anchorage" fibres were clearly oriented along the patterned line (Figure 5.10 a, first image). When cells round up and the cell membrane retracts during mitosis, retraction fibres remain attached to the substrate to ensure cell stability and retention of orientational information. Using micropatterns, researchers found that the orientation of the mitotic spindle is determined by the polarity of the cytoskeletal network and adhesion forces, and consequently modifying micropattern geometry results in different division orientations [31, 32]. Thus, our observation of the NPC division orientation along the lines is comparable with previous studies by exhibiting this conserved mechanism.

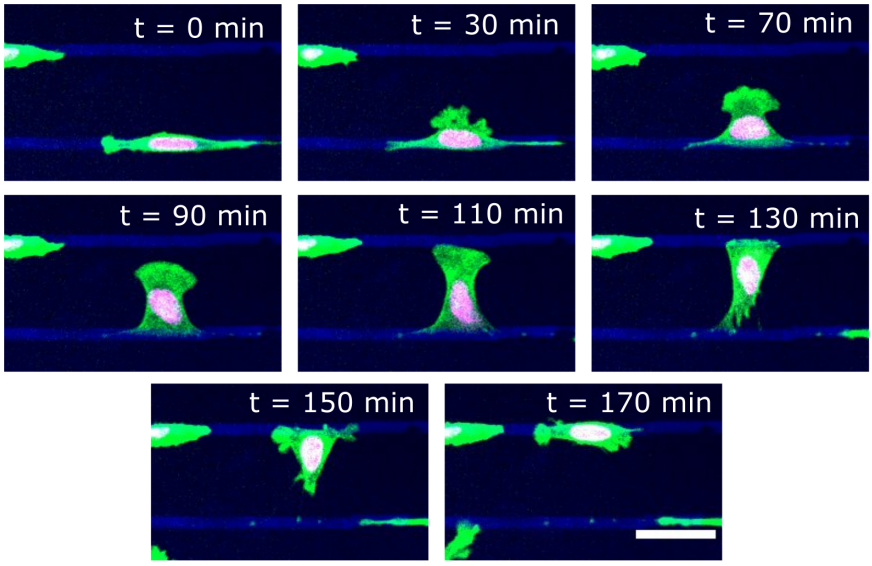

Figure 5.9: NPC jumping between lines. NPC extending over the interspace region between two lines until it reaches the neighboring line and pulls the cell body over. Scale 50 μm.

Interestingly, directly following division, NPCs show directional movement away from each other for up to 50 min after division (i.e., 5 time frames) (Figure 5.10 a). As observed in our experiment, Dix *et al.* (2018) found the same behaviour for RPE1 cells on lines

that, in their shown example (Figure S1 in Dix *et al.* (2018) [33]), migrated away from each other for 90 min after division. This process is crucial for daughter cells to separate from each other after mitosis and re-spread. Using this process to guide cell direction after mitosis might be a valuable asset to control NPC spreading in CNS implants.

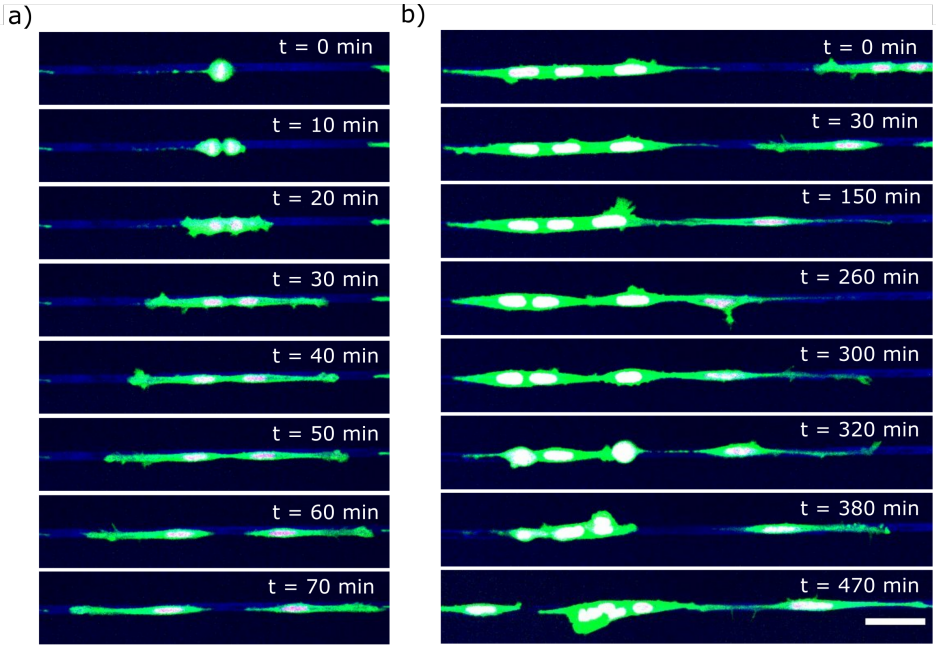

Figure 5.10: NPC mitosis and social behaviour on lines. a) Upon mitosis, daughter cells migrate into opposite direction. b) Upon encountering a cell ensemble, NPC first exhibits contact inhibition of locomotion (t = 380 min) and then reconnects again (t = 470 min). Scale bar 50 μm.

A last striking behavioural pattern was the preference of NPCs for each other's company. Cells often accumulated with 4 - 6 neighbouring cells, although there was enough space available to move away (Figure 5.10 b). However, NPCs did not accumulate all together, but rather found a balance between exploratory single cells and collective assemblies. Notably, these states were often temporary as NPCs kept moving and interacting. A crucial aspect of cell migration *in vivo* is the direct interaction with other cells. Hereby, cells communicate with each other via chemical and physical interactions, and cell-cell contacts play a major role in coordinating their behaviour [34]. Thus, for these NPCs physical contact seems to be particularly important and would be highly interesting to investigate in detail in further experiments.

While migrating *in vivo* or on 2D substrates, cells often collide with other cells. In various publications, micropattern techniques have been used to explore collisions of migrating cells on lines patterns [35, 36]. Hereby, different behavioural patterns have been observed: Upon head-to-head collisions, cells can react with contact inhibition lo-

comotion (CIL), showing repulsive behaviour and moving away from the contacted cell [37]. When a cell walks into the tail end of another cell, contact following of locomotion (CFL) has been observed, whereby the cell starts migrating towards the tail of the neighbouring cell [35].

Analysing our data for these behaviours, we found only rare occasions of CIL. One example of CIL is shown in Figure 5.10 b, whereby one cell (from right) bumps into a cell assembly (on the left) and reverses its movement. Notably, this cell just divided and thus had the momentum of migrating away from its sister cell. This indicates that cells need a certain minimum of directional persistence and speed to exhibit CIL. Thus, the reason for low occurrence of CIL in our experiments, might be that NPCs here do not exhibit high directional persistence and often reserve direction thus not fully colliding into their neighbours. However, to form and test this hypothesis further experiments are required.

Neuroblasts migrating in the rostral migratory stream (for more details, see chapter 1) often move in chains [14], thus making CFL an expected behaviour. However, NPCs were not observed to collide and follow the tail of other cells, which must be due to the lack of real colliding events, as stated above. Notably, walking by or over other cells was another common behaviour NPCs exhibited when neighbouring cells were in their path, showing a rather different behaviour than CIL or CFL.

CONCLUSIVE BULLET POINTS

Here the results of the current subchapter are summarized:

Statistical analysis

• On 2D printed lines, NPCs follow the PRW motion model
• Average velocity values are 0.284±0.008 μm/min, 0.304±0.009 8 μm/min, 0.268±0.0088 μm/min 0.283±0.011 μm/min for L10, L15, L20, and L25, respectively • Persistence times of motion are with 19.7±1.2 min, 25.3±2.7 min, and 20.9±2.8 min for L10, L20, and L25, respectively
• Diffusion coefficients are 0.9±0.01 μm^2/min, 0.98±0.02 μm^2/min, 0.99±0.03 μm^2/min, and 0.90±0.01 μm^2/min for L10, L15, L20, and L25, respectively
• Together, NPCs move slightly faster on L20 lines than on other lines, thus indicating that a width of 20 μm might facilitate cell motion

Observational analysis

• NPCs frequently reverse direction as do neuroblasts *in vivo*
• NPCs show highly explorative behaviour, with short directional persistence thus confirming PRW also by visual observations
• NPCs do not bridge non-adhesive regions, but jump to neighbouring lines
• Upon mitosis, NPCs separate and migrate away from each other
• NPCs stay as single cells and accumulate in small groups
• NPCs hardly show collisions upon locomotion in our experiments, and thus hardly exhibit CIL or CFL behaviour

5.2.3. MORE COMPLEX 2D GEOMETRIES

As stated above, NPCs migrate through a complex ECM network and use blood vessels and astrocytes as guiding scaffolds. These structures intersect and branch, providing a variety of challenges and cues to migrating NPCs. Another crucial aspect of cell migration *in vivo* is the direct interaction with other cells. To approach this higher complexity in a minimalistic way, we created different 2D laminin micropattern geometries using honeycomb and square patterns in a smaller and larger size variation. This allowed to tackle broader geometrical substrate variation, and influence and observe single cell-cell contacts. Length parameters of both patterns until intersections were 50 μm and 150 μm, further referred to as "small" and "big". Big honeycomb and squares were provided with small islands around the intersection to promote cell spreading in these regions and isolate the protrusions. Pattern widths were set to 10 μm, to approach the diameter of blood vessels in murine brains by still accounting the lack of 3D space [38].

To catch the dynamics of NPCs, time lapse of 15 h duration with brightfield images every 1 min were performed. For these experiments, solely analysis by visual observations was employed and a set of behavioural patterns in NPCs was found on these geometries. As the big honeycomb pattern resembles the cerebral vasculature arrangement the most, taking into account the high simplification and placement on 2D substrate, we primarily focused on the analysis of this geometry. Important to note here is that upon analysis it became clear that resulting widths of big honeycomb and squares arms were not 10 μm but below 5 μm. This probably occurred due to technical difficulties of μPIP with this pattern, whereby the plasma was not able to entirely flood through the full width of the arm channels. However, as murine brain capillaries have been measured to have a mean diameter around 4 μm [38], we proceeded our analysis with these patterns.

On all patterns, changes of cell shapes were observed that were imposed by the NPCs spreading on the 2D confined environment. This behaviour is consistent with literature were cells seeded on patterned adhesive proteins were shown to spread out and adapt to shape and size of the pattern [39].

On the big honeycomb patterns, on rare occasions NPCs have been found to stretch out along the arm (Figure 5.11 a). However, as intended by placing islands at intersections, NPCs preferred to spread at the intersections, extending their protrusions to all three directions (Figure 5.11 b). Interestingly, in these states several NPCs were found to stay in a stretched out state for a long time without changing their morphology. In the shown example, NPCs extended on the line remained for 527 min, and on the intersection for 300 min. On small squares and honeycombs, NPCs often spread over 2-3 pattern units, trying to take up more space. Here, cells were more mobile as compared to the big patterns.

As established in section 5.2.2, explorative motion is innate to NPCs. Likewise, on these more complex geometries, NPCs were found to explore their surroundings. However, on these patterns the cells were mostly stationary and explorative dynamics were primarily performed via lamellipodia and filopodia extensions. Figure 5.11 c exemplifies this behaviour, showing a cell centred at the intersection of the honeycomb and extending its lamellipodia into all three directions. Nam *et al.* (2007) found that stationary cells *in vivo* exhibited longer and more processes. Together with our observations, this sug-

gests that when the cell body remains immobile, the cell uses its processes to explore the area and collect directional cues.

Migration of NPCs was only observed right after cell division (Figure 5.11 d), whereby the daughter cells walked for a short distance away from each other (as already discussed in section 5.2.2). An intriguing question would be where the lines is between NPCs showing migratory behaviour and NPCs preferring to align on pattern and remain rather stationary? Most cell types migrate on unidirectional lines [20] and align and stretch out on other geometrical patterns [39]. Thus, it would be interesting to create geometrical variations to tackle this question.

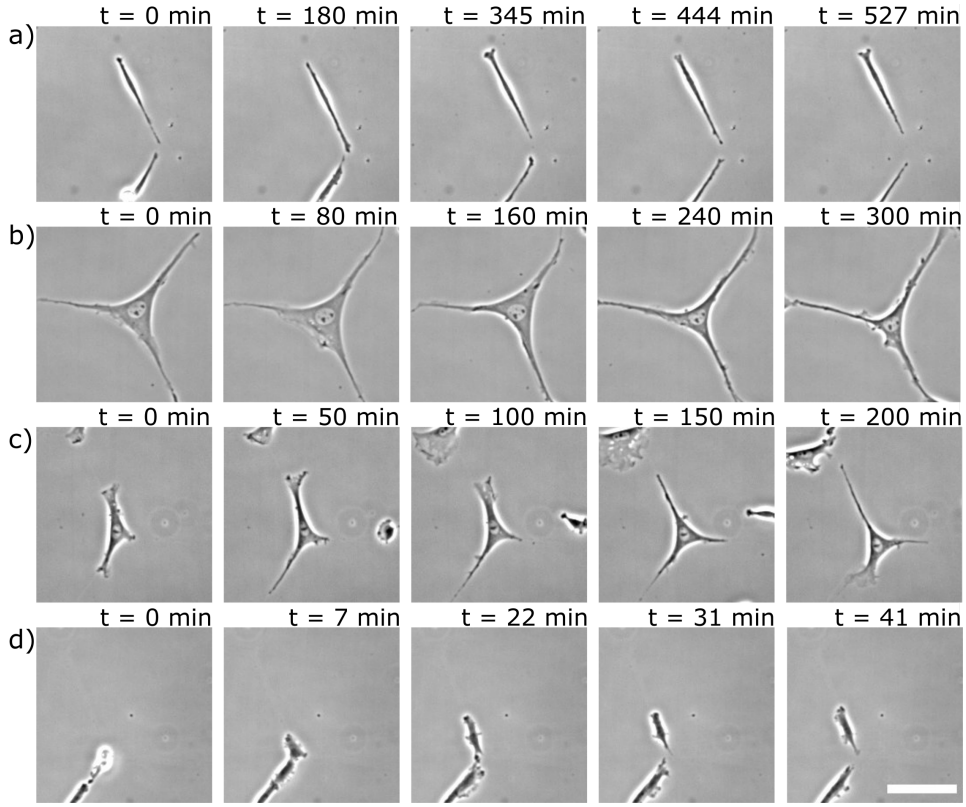

Figure 5.11: NPC distribution and pattern formation after 15 h. NPCs align on the small honeycomb by stretching between two intersections (a), whereas on the big honeycomb (b), small squares (c), and big squares (d), NPCs mainly place their bodies at the intersections. This repetitive behaviour results in a pattern formation. Scale bar is 100 μm.

The employed geometries and used cell seeding numbers allowed for regular cell-cell interactions. Interestingly, NPCs were often observed to tackle each other with their protrusions, appearing to also push and fight for space (Figure 5.12). Figure 5.12 a shows how one NPCs occupies the intersection and interacts via its protrusion with a neigh-

bouring cell. First, the NPC is extending the protrusion, forcing back the protrusion of the neighbouring cell, but then gives in to the extension of the neighbouring cell.

Another example for space competition shows how three NPCs extend their protrusions towards one intersection, whereby one NPC coming from above moves faster towards it and takes the space over by spreading its cell body over it (Figure 5.12 b). Figure 5.12 c exemplifies how three NPCs occupy one honeycomb intersection until one NPC is defeated. Upon giving up the space it allowed the other two cells to spread out more. The last scenario shows a cell division on the intersection resulting in two daughter cells competing for the space (Figure 5.12 d).

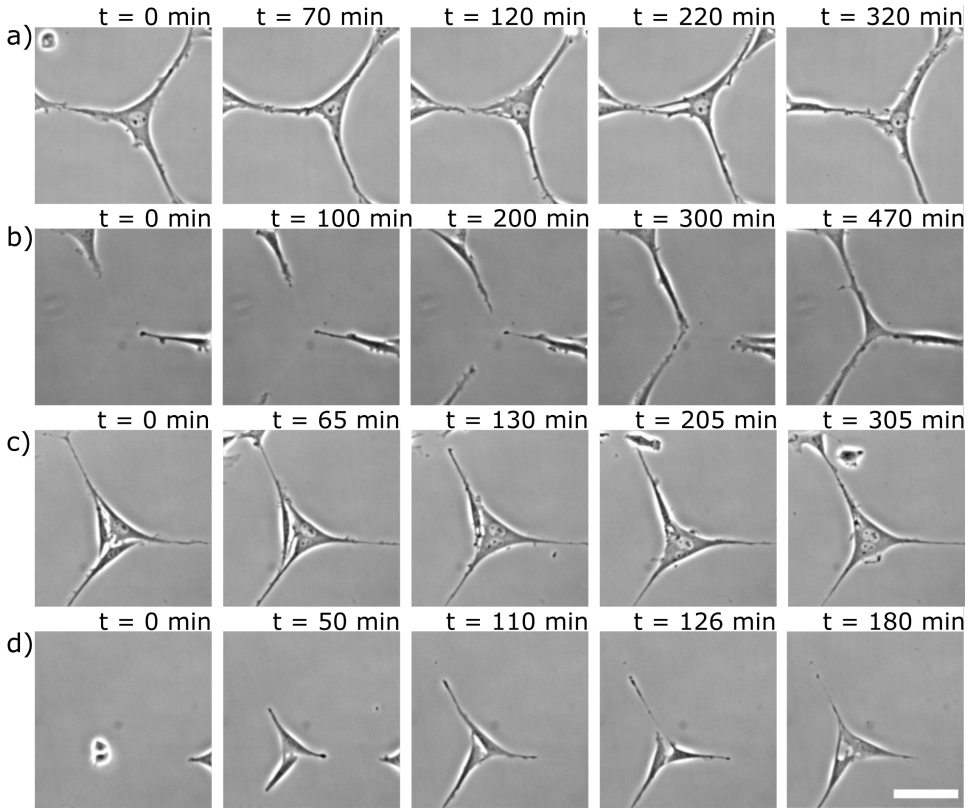

Figure 5.12: NPC competition for space on honeycomb intersections. a) NPC is stretched out at the intersection and is using its extension to push against a cell invading from the left side. b) Three NPCs are competing for the space at one intersection, whereby the left cell loses and retracts in the last two frames. c) From all three sides, NPCs are moving towards one intersection, whereby the cell coming from above manages to place its body and stretch out slightly in the last frame. d) Upon mitosis, daughter cells are stretching out and competing for the space at the intersection. Scale bar is 50 μm.

Except for literature analysing collisions upon locomotion (see section 5.2.2), no publications have been found researching the topic of competition for space, especially on an individual cell level. Thus, this observations are highly interesting. Using our set-up would be ideal in creating a framework to research this competitive behaviour in detail and contributing to our understanding of NPC migratory behaviour and distribution *in vivo*.

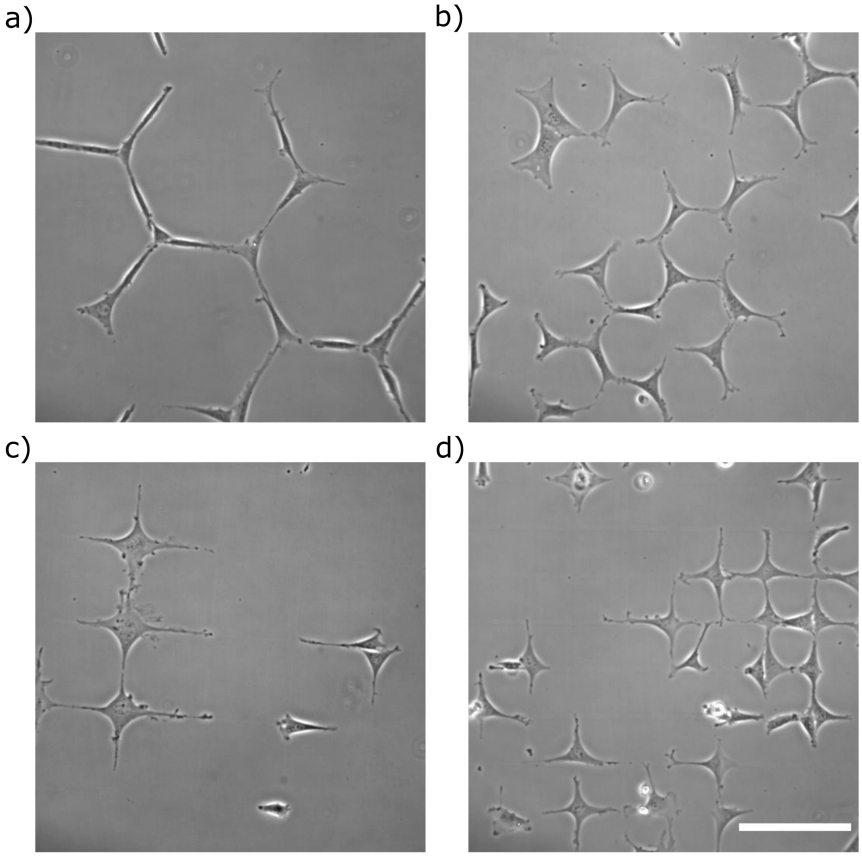

Figure 5.13: NPC distribution and pattern formation after 15 h. NPCs align on the small honeycomb by stretching between two intersections (a), whereas on the big honeycomb (b), small squares (c), and big squares (d), NPCs mainly place their bodies at the intersections. This repetitive behaviour results in a pattern formation. Scale bar is 100 μm.

All described behaviours together result in a nearly homogeneous spreading of NPCs on the patterns (Figure 5.13). The ongoing exploration of the environment, the alignment of cell morphology to the pattern, and the competition for bigger space all lead to a "network" of NPCs on the patterned geometries. Once the space is distributed, the cells keep their network for longer time scales and adjust only when they are dividing and producing more progeny to share the space with.

On small honeycomb pattern (Figure 5.13 b), NPC often stretch in between two intersection, connecting their two arms on side with two arms of the neighbouring cell. On the big honeycomb, cells either stretch out on the intersections or align in between them (Figure 5.13 a). On squares, big and small, NPCs prefer to place their body on the intersections and spread their protrusions in all four directions (Figure 5.13 c, d).

CONCLUSIVE BULLET POINTS

Here the results of the current subchapter are summarized:

- By using more complex geometries, we observed additional behaviours to those found on patterned lines (section 5.2.2)
- NPCs are rarely migrating and are rather stationary with highly dynamic protrusions
- When individual NPCs elongate or spread out taking up more space, they often keep their shape including their protrusions static (until mitosis)
- NPCs compete for space on intersections
- With time, NPCs distribute the space nearly evenly, producing "networks" on the patterns

5.2.4. MICROCHANNELS AND CONFINEMENT

In vivo, cells migrate through dense three-dimensional (3D) environment passing through different barriers imposed by the microstructural extracellular matrix (ECM) and other cells. Adherence to their surrounding in all directions and the possibility to use all sites to push themselves forward, influences the migratory dynamics of cells. Thus, as a next step in in attempting a more detailed understanding of NPC migration behaviour *in vivo*, a minimal 3D-environment system is introduced below. Here, only first experiments were performed and are shortly discussed, as for a full analysis more data is required.

By using PDMS moulded microchannels placed upside-down on substrate, we created a 3D environment for NPCs while still keeping their movement restricted to a unilinear condition. PDMS and substrate were coated with laminin to enhance cell adhesion. NPCs were seeded on one side of the mould and invading cells were observed to probe the tunnel first with protrusions before crawling inside the tunnel and migrating along it (Figure 5.14 a). Apparently, NPC were using the channel walls to attach and move forward (Figure 5.14 a, white circles). By employing our reporter cell line with nucleus and actin labels (chapter 4), this set-up opens the possibility to track migration in microchannels as well as observe the explorative behaviour by following the GFP-labelled actin polymerization. Statistical analysis as performed on 2D substrate and lines (sections 5.2.1 and 5.2.2), would be highly interesting yielding more insight into NPC motion

in a 3D-confined environment. However, due to technical reasons and time constraints, this data set could not be analysed.

An additional element cells regularly encounter *in vivo* are spatial confinements with sizes smaller than the cell diameter. To overcome these obstacles and squeeze through narrow pores, cell migration critically depends on cellular shape adaptation [40]. While the cytoplasm and plasma membrane are flexible, the nucleus is the largest organelle with stiffness values 2-10- fold higher than the surrounding cytoplasm [41, 42], making it the main restricting component in migration [43, 44].

By creating 3D microchannels with constrictions, we created an easy system to observe NPC dynamics and behaviour upon encountering spatial confinement with sizes smaller than their nucleus diameter. Performing a time-lapse of an imaging period of several hours with images taken every 30 sec, we captured a cell squeezing its nucleus through the restriction (Figure 5.14 b). From the start of the imaging period, where the front tip of the nucleus was already within the constriction (t = 0 min), this NPC needed 260 min to push through until the rear tip of the nucleus reached the constriction. Interestingly, squeezing the first part of the nucleus took more time and once the cell nucleus was half through the confinement (Figure 5.14 b; star) after 180 min, the pushing accelerated. From here, it took only 80 min until the second part of the nucleus was through the constriction. As overcoming this kind of confinement influences the migration time, collecting and evaluating these dynamics will be valuable to learn about the dynamics of NPCs while migrating *in vivo*.

Another interesting element observed here were the fixed attachment sides of the cytoskeleton at the channel walls (Figure 5.14 b, first image white circles). Seemingly, they were used as ankers which the cell used to push away from as well as pull towards to, and remained the same throughout the imaging time. As an example, as zoom in of the upper attachment side at the constriction shows the actin polymerization (Figure 5.14 c) and thus force generation of the cytoskeleton [45, 46].

In contrast to the fixed attachment sides, the filopodia were highly dynamic (Figure 5.14 d) and might have also served as an additional force generation or had just an explorative function. The microchannel system mimics the bigger gaps in the extracellular matrix (ECM) through which NPCs are migrating. Additionally, it approaches environment of the rostral migratory stream highway on which neuroblasts move along [47]. Additional constrictions mimic small pores of the ECM. Together, this system provides a simple approach to learn more about how NPC overcome obstacles *in vivo* and regulate their shape and nuclear dynamics.

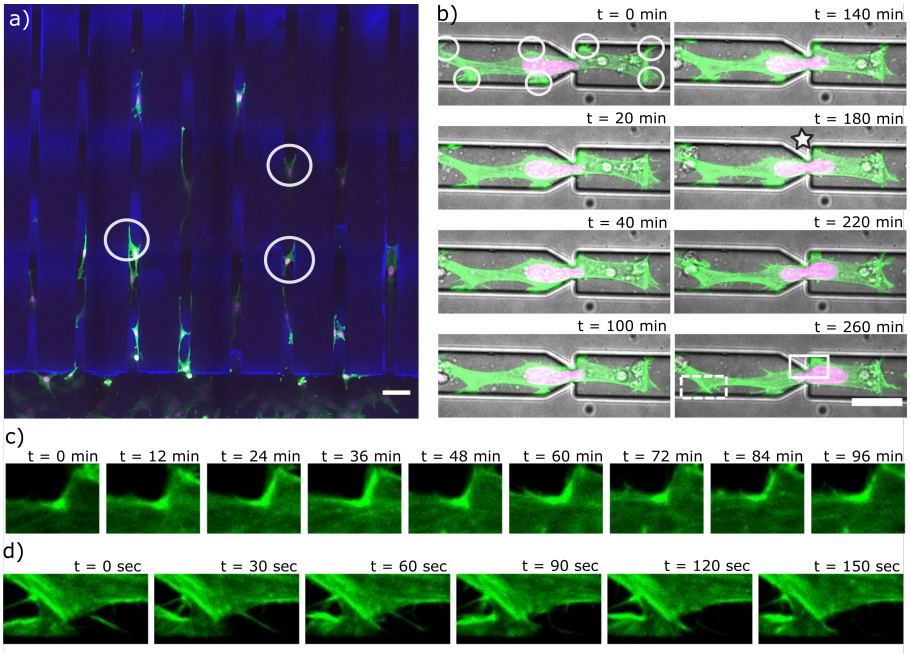

Figure 5.14: NPCs moving through microchannels and confinement. a) NPCs move along microchannels using the walls to move forward (white circles). Scale bar is 100 μm. b) Time-lapse imaging of a cell pushing its nucleus through a confinement, exhibiting stable attachment sides throughout the process (white circles). Scale bar is 50 μm. c) White rectangle from last image b. Zoom in of cell attachment side, showing on attachment side, showing actin polymerization (bright green) to generate force against the channel wall. d) White dashed rectangle from last image in b. Zoom showing that the pseudopodia are highly mobile.

CONCLUSIVE BULLET POINTS

Here the results of the current subchapter are summarized:

- Microchannels mimic bigger gaps in the extracellular matrix through which NPCs migrate *in vivo* while constrictions model small pores that NPCs need to squeeze through while migrating
- In microchannels, NPCs use channel walls to attach and move along
- When squeezing through a constriction, NPCs use fixed attachment sides to generate force for pushing away and pulling towards
- While attachment sides are fixed, filopodia are highly dynamic throughout the squeezing process

5.2.5. CONCLUSIONS

Neural progenitor cells (NPCs) have high regenerative capacity and are highly promising for therapeutic applications in neurodegenerative diseases and central nervous system injuries. Thus, understanding their innate behaviour and migratory patterns is crucial for the development of successful treatment. Minimalistic *in vitro* systems help to deconstruct the high *in vivo* complexity and provide valuable insights that contribute to this understanding. Although these systems were used to research other cell types [2], literature investigating NPC migration under standardized microenvironments *in vitro* is missing.

Here, we employed various minimalistic systems and performed statistical analysis as well as visual observations to acquire data on NPC dynamics. The focus was to establish these systems for NPC and to produce preliminary statistical output as well as qualitative assessment.

The experiments showed that NPCs move in a persistent random walk (PRW) on 2D uniform ECM substrate as well as 2D ECM-printed lines. Qualitative analysis of NPCs on patterned lines and more complex 2D geometries provided insights a set of behavioural patterns these cells express innately and as a reaction to the environment. Lastly, testing NPC dynamics in microchannels with and without constrictions, showed that the cells readily invade the channels and squeeze their nucleus through small pores while using the channel walls as support to push against and pull forward.

The generated results contribute to fundamental understanding of NPC dynamics. The calculated values of NPC speed, diffusion, and persistence time can be used for theoretical modelling to establish predictions of NPC migration under different scenarios. Further insights can be used to control NPC recruitment and tissue patterning for therapeutic applications.

After validating the minimal systems introduced here, the next step would be to combine them and thus creating a higher complexity set-up yielding more data on NPC dynamics. By creating microchannels with constrictions in a big honeycomb geometry, seeding NPCs on one side and placing a chemoattract on the other side, the *in vivo* situation can be mimicked whereby neuroblasts exit the rostral migratory stream (RMS) to move towards an injury. Adding different sizes of constrictions would give more insight into their deformation capacity and influence of small pores *in vivo* on migration speed and route choice. Alternatively, by presenting neurons and astrocytes that were damaged by high laser exposure (instead of a chemoattract), a more sophisticated system could be established providing the additional possibility to observe NPC differentiation and integration into the neural network. Once established, different types of neuroblast precursors [48] can be tested to investigate possible differences in their motility patterns.

In this chapter, for the first time (to our knowledge) neural progenitor cells were exposed to standardized microenvironments and preliminary statistical and visual data on their dynamics was collected. Expanding these experiments and learning more about the fundamental motility patterns of NPCs, as well as testing their response to various obstacles under controlled conditions, will be crucial for the establishment of successful treatments of neurodegenerative diseases and CNS injuries.

5.3. MATERIALS AND METHODS

5.3.1. PREPARATION OF PDMS STRUCTURES

To prepare the master slide, the design of the pattern was created by constructing a stereolithography CAD (computer-aided design) file (STL format). The CAD design was converted to laser coordinates using Nanowrite (Nanoscribe). The 3D structure was then exposed in a photoresist (IP-S, Nanoscribe)via two-photon polymerisation (2PP) with the Photonic Professional GT2 equipment (Nanoscribe) (these steps were performed and master mould provided by J. A. J. Wondergem). This master mould was subsequently used to prepare a patterned poly(dimethylsiloxane) (PDMS) stamps. PDMS (Sylgard 184, Dow Corning) is a two-component silicon elastomer which consists of a prepolymer and a curing agent. The prepolymer was mixed with the curing agent in a ratio of 1:10 and desiccated at 60 mbar for 1 h (MZ2NT, vacuubrand), ensuring escape of trapped air. In parallel, an adjacent vacuum chamber was used to deposit a Trichloro(1H,1H,2H,2H-perfluorooctyl)silane layer (448931, Sigma), on the master mould to ensure that PDMS can be peeled off easily later. Next, PDMS was poured over the master mould and vacuum applied again (60 mbar 1h) to ensure that the polymer enters all tunnels. Lastly, the structure was baked at 110 °C for 3h (or at 90 °C overnight) in an oven (Melag) to solidify the PDMS. After cooling down, the stamp was cut and peeled off ready for experimental use.

5.3.2. FABRICATION OF 2D PATTERNS AND MICROCHANNELS

ECM protein coating (for section 5.2.1)
A 35 mm μ-Dish (uncoated, 81151, Sigma) was open placed into a UV chamber (UVO Cleaner, Jelight Company Inc.) and exposed to UV light for 10 min. Subsequently, the dish was covered with either 1-2 μg/mL laminin (Merck, L2020) in DMEM for at least 1 h in the incubator at 37 °C or covered with fibronectin (F1141; Sigma) diluted 1:10 in MilliQ for 1 h at room temperature.

μCP of Fibronectin lines (for section 5.2.2)
To produce 2D line pattern micro-contact printing (μCP) technique was used. The PDMS pattern was exposed for 15 min to UV (UVO Cleaner, Jelight Company Inc.) and then a drop of fibronectin solution was deposited on its surface and incubated for 30 min in the dark. Fibronectin solution: 50 μg/ml fluorescent fibronectin linked with Alexa Fluor 647 (kindly provided by Schmidt group) was mixed with 10 μg/ml un-labelled fibronectin and filled to 40 μl with MilliQ water. After incubation, not adsorbed fibronectin was washed away with MilliQ and left for 20 min to dry in the cell culture hood. An uncoated 35 mm μ-Dish (81151, ibidi) was exposed to UV light for 15 min to activate its surface. The PDMS stamp was flipped onto the dish surface, gently pressed down, and incubated for 30 min in the dark. Subsequently, the stamp was removed, and the dish was washed with 70% ethanol and covered with 0.25% Pluronic F-127 for 1h. Finally, the dish was washed 2x with PBS and used for cell seeding and experiments. Alternatively, the patterned dish could be stored for maximum 2 days at 4 °C before use.

μPIP of honeycomb and square patterns (for section 5.2.3)
For the microscale plasma-induced patterning (μPIP), the PDMS pattern was cut along the pattern borders to ensure that plasma can flow in every tunnel. The cut PDMS was placed onto an uncoated 35 mm μ-Dish (81151, ibidi) with the pattern facing downwards and gently pressed down. Next, the dish with the PDMS was exposed to plasma for 6 min (Plasma-Surface-Technology, Diener electronic). When finished, the stamp was gently removed, and the surface covered with 0.2% Pluronic F-127 for 1h at room temperature. To return to sterile conditions, the dish was washed with 70% Ethanol and 2x with PBS. The dish was covered with a laminin solution (1-2 μg/ml) and incubated for 1h in the incubator at 37 °C. Finally, the patterned dish could be used for experiment or be stored for maximum 1 day in the incubator at 37 °C before use.

Microchannels and constrictions (for section 5.2.4)
To ensure cell invasion, the PDMS pattern had to be cut along the start of the channels. For microchannels, an ibiTreat 35 mm μ-Dish (81156, ibidi) was used. The PDMS pattern was exposed for 15 min to UV light (UVO Cleaner, Jelight Company Inc.) and incubated with fibronectin solution as described in section above to ensure cell attachment and visualize the lines. For microchannels with confinement, an ibiTreat 4 Well μ-Slide was used (80426, ibidi) and the PDMS pattern was exposed 15 min to UV (UVO Cleaner, Jelight Company Inc.) and incubated with 1:10 fibronectin (F1141, Sigma) solution in MilliQ. In both cases, the PDMS pattern was flipped onto the dish surface, gently pressed down and the dish was covered with cell culture media. Then, the dish was placed without the lid into a p60 culture dish, and its lid closed and exposed to vacuum for 10 min at 20 mbar (MZ2NT, vacuubrand) to facilitate fluid perfusion throughout the channels. Lastly, the structure was used for experiments or was stored for maximum 1 day in the incubator at 37 °C before use.

5.3.3. CELL CULTURE

C17.2 cells (Merck, 07062902) were cultured as described in chapter 4. NPCs with labelled actin and nuclei were generated via transduction as described in chapter 4.

5.3.4. LIVE CELL IMAGING

Cells were imaged with a Nikon Eclipse Ti-E inverted microscope (Nikon Instruments Europe, Netherlands), equipped with a spinning disk unit (Yokogawa, 10,000 rpm). An automated XY stage facilitated imaging multiple fields of view. Positions were illuminated either with 488 nm, 561 nm, and/or 647 nm lasers (Agilent MLC400 monolithic laser combiner, Agilent Technologies, Netherlands), and/or with bright-field. Images were captured with an Andor iXon Ultra 897 High-speed EM-CCD camera. Image acquisition was automated using NisElements software (LIM, Czech Republic). Stable conditions throughout the measurements were ensured by using a Tokai Hit stage incubator set to 37 ∘C and 5% CO2. The incubator is equipped with a water bath to maintain a certain humidity.

Imaging specifics. Section 5.2.1: Plan Apo λ 20x objective, large image 6x6, time-lapse with imaging period of 20 h and images taken every 10 min with 488 nm and 561 nm lasers to visualize the actin network and cell nuclei, respectively. Section 5.2.2: Plan

Apo λ 20x objective, large image 6x10, time-lapse with imaging period of 22h and images taken every 10 min with 488 nm and 561 nm lasers to visualize the actin network and cell nuclei, respectively. At the end of the experiment, one image with 647 nm illumination was performed to visualize the patterned lines. Section 5.2.3: Plan Fluor 10x Ph1 DLL, multiple positions 30 XY, time-lapse with imaging period of 15 h and images taken every 1 min with brightfield. Section 5.2.4 5.1.4: a) microchannels: Plan Apo λ 20x objective, large image 12x6, time-lapse with imaging period of 48 h and images taken every 15 min with 488 nm, 561nm, and 647 nm to visualize actin, cell nuclei, and fibronectin-labelled lines. b) microchannels with confinement: Plan Apo λ 60x Oil objective, time-lapse with imaging period of 35 min and images taken every 30 sec with 488 nm and 561 nm lasers to visualize the actin network and cell nuclei, respectively, and brightfield to visualize the channel.

5.3.5. CELL TRACKING AND ANALYSIS

Cell movement was analysed by tracking the nucleus of the cells. Fluorescent time-lapse images (excitation at 561 nm) were rendered into binary images using ImageJ (http://imagej.nih.gov/ij/). Tracking was performed using the Image J Plugin TrackMate [49], whereby all trajectories had to be corrected manually. With each cell division, a new trajectory was started and trajectory lengths with less than 30 points were omitted. Based on this data, trajectory length and directions, and movement statistics based on the mean squared displacement (MSD) were calculated and plotted, using a home-made Matlab algorithm written by J. A. J. Wondergem. The MSD measures the space a cell explores over time. The trajectory data are arrays of the position r(t) = x(t) + y(t) of the cell at time t. The displacement δ r is given by

$$\delta r(t) = r(t+\delta t) - r(t) \tag{5.1}$$

where δt is the inverse frame rate. The MSD of a cell trajectory is defined as the average of squared displacements for all lag times τ = k δ t, given by

$$\langle \delta r(\tau)^2 \rangle = \frac{1}{N-k} \sum_{i=1}^{N-k} (r(t_i+\tau) - r(t_i))^2 \tag{5.2}$$

where N is the number of points in the trajectory and k = 1, 2,..., N - 1.

ll values of the MSD are averaged over the number of trajectories. The 95% confidence bounds were determined by using a t-distribution using an α value of 2.5% and the degrees of freedom set to the number of trajectories.

To analyse the trajectory data, we used an MSD PRW fit (equation 1.1) and an MSD linear fit to diffusive regime (equation 1.3). Specifically, the MSD curve was fitted to the following formula derived for a 2D PRW [50]:

$$\langle \delta r(\tau)^2 \rangle = 2v^2\tau_p^2(\frac{\tau}{\tau_p} + e^{\frac{-\tau}{\tau_p}} - 1) \tag{5.3}$$

where τ is the lag time, v is the instantaneous velocity, and τ_p the persistence time. Fitting the MSD to this equation allows to extract the migration parameters v and τ_p. For fits of 1D motion, the factor of 2 drops out of equation 1.3.

At short timescales ($t << \tau_p$), the motion described by equation 4.3 is ballistic ($\langle \delta r(\tau)^2 \rangle \approx (vt)^2$) due to persistence in orientation of the cell. At long timescales ($t >> \tau_p$), equation 4.3 is approximated by $\langle \delta r(\tau)^2 \rangle \approx 2v^2 2\tau_p t$ (for fits in 1D, this becomes $\approx v^2\tau_p$ t), which describes diffusive motion.

To find an effective diffusion coefficient D_eff, the MSD was fitted linearly at long times using the formula:

$$\langle \delta r(\tau)^2 \rangle \xrightarrow{\tau \gg \tau} 4D_eff\tau \tag{5.4}$$

For fits of 1D motion, the factor of 4 becomes 2 in equation 1.4. Subsequently, the average velocity (v) was extracted based on the calculated velocities using $\delta r/\delta$ t.

5.4. REFERENCES

[1] Ramsés Ayala, Tianzhi Shu, and Li-Huei Tsai. "Trekking across the brain: the journey of neuronal migration". In: *Cell* 128.1 (2007), pp. 29–43.

[2] Juan Manuel Garcia-Arcos et al. "Reconstitution of cell migration at a glance". In: *Journal of cell science* 132.4 (2019), jcs225565.

[3] Antonetta BC Buskermolen et al. "Entropic forces drive cellular contact guidance". In: *Biophysical journal* 116.10 (2019), pp. 1994–2008.

[4] Amélie Béduer et al. "Engineering of adult human neural stem cells differentiation through surface micropatterning". In: *Biomaterials* 33.2 (2012), pp. 504–514.

[5] Arjan P Quist and Sven Oscarsson. "Micropatterned surfaces: techniques and applications in cell biology". In: *Expert opinion on drug discovery* 5.6 (2010), pp. 569–581.

[6] Menekse Ermis, Ezgi Antmen, and Vasif Hasirci. "Micro and Nanofabrication methods to control cell-substrate interactions and cell behavior: A review from the tissue engineering perspective". In: *Bioactive materials* 3.3 (2018), pp. 355–369.

[7] Changjiang You and Jacob Piehler. "Functional protein micropatterning for drug design and discovery". In: *Expert opinion on drug discovery* 11.1 (2016), pp. 105–119.

[8] András Perl, David N Reinhoudt, and Jurriaan Huskens. "Microcontact printing: limitations and achievements". In: *Advanced Materials* 21.22 (2009), pp. 2257–2268.

[9] Bryan A Langowski and Kathryn E Uhrich. "Microscale plasma-initiated patterning (μpip)". In: *Langmuir* 21.23 (2005), pp. 10509–10514.

[10] David Selmeczi et al. "Cell motility as random motion: A review". In: *The European Physical Journal Special Topics* 157.1 (2008), pp. 1–15.

[11] Daniel Campos, Vicenç Méndez, and Isaac Llopis. "Persistent random motion: Uncovering cell migration dynamics". In: *Journal of theoretical biology* 267.4 (2010), pp. 526–534.

[12] Mitchell H Gail and Charles W Boone. "The locomotion of mouse fibroblasts in tissue culture". In: *Biophysical journal* 10.10 (1970), pp. 980–993.

[13] Takuro Kojima et al. "Subventricular zone-derived neural progenitor cells migrate along a blood vessel scaffold toward the post-stroke striatum". In: *Stem cells* 28.3 (2010), pp. 545–554.

[14] Naoko Kaneko, Masato Sawada, and Kazunobu Sawamoto. "Mechanisms of neuronal migration in the adult brain". In: *Journal of neurochemistry* 141.6 (2017), pp. 835–847.

[15] Valerie A Liu, William E Jastromb, and Sangeeta N Bhatia. "Engineering protein and cell adhesivity using PEO-terminated triblock polymers". In: *Journal of biomedical materials research* 60.1 (2002), pp. 126–134.

[16] Kenneth R Chien, Ibrahim J Domian, and Kevin Kit Parker. “Cardiogenesis and the complex biology of regenerative cardiovascular medicine”. In: *Science* 322.5907 (2008), pp. 1494–1497.

[17] Hug Aubin et al. “Directed 3D cell alignment and elongation in microengineered hydrogels”. In: *Biomaterials* 31.27 (2010), pp. 6941–6951.

[18] Arja Ray et al. “Anisotropic forces from spatially constrained focal adhesions mediate contact guidance directed cell migration”. In: *Nature communications* 8.1 (2017), pp. 1–17.

[19] Claire Leclech and Catherine Villard. “Cellular and subcellular contact guidance on microfabricated substrates”. In: *Frontiers in Bioengineering and Biotechnology* 8 (2020), p. 1198.

[20] Paolo Maiuri et al. “The first world cell race”. In: *Current Biology* 22.17 (2012), R673–R675.

[21] Camila Londono et al. “Nonautonomous contact guidance signaling during collective cell migration”. In: *Proceedings of the National Academy of Sciences* 111.5 (2014), pp. 1807–1812.

[22] Revathi Ananthakrishnan and Allen Ehrlicher. “The forces behind cell movement”. In: *International journal of biological sciences* 3.5 (2007), p. 303.

[23] Akiyoshi Kakita and James E Goldman. “Patterns and dynamics of SVZ cell migration in the postnatal forebrain: monitoring living progenitors in slice preparations”. In: *Neuron* 23.3 (1999), pp. 461–472.

[24] Noelia Martinez-Molina et al. “Rostral migratory stream neuroblasts turn and change directions in stereotypic patterns”. In: *Cell adhesion & migration* 5.1 (2011), pp. 83–95.

[25] Michael P Sheetz et al. “Cell migration as a five-step cycle.” In: *Biochemical Society Symposium*. Vol. 65. 1999, pp. 233–243.

[26] Sang Chae Nam et al. “Dynamic features of postnatal subventricular zone cell motility: A two-photon time-lapse study”. In: *Journal of Comparative Neurology* 505.2 (2007), pp. 190–208.

[27] Rui L Zhang et al. “Patterns and dynamics of subventricular zone neuroblast migration in the ischemic striatum of the adult mouse”. In: *Journal of Cerebral Blood Flow & Metabolism* 29.7 (2009), pp. 1240–1250.

[28] Bodo Borm et al. “Membrane ruffles in cell migration: indicators of inefficient lamellipodia adhesion and compartments of actin filament reorganization”. In: *Experimental cell research* 302.1 (2005), pp. 83–95.

[29] Qing Zhang. “The Research Advance of Cell Bridges in vitro”. In: *Frontiers in Bioengineering and Biotechnology* 8 (2020), p. 1349.

[30] Antonetta BC Buskermolen et al. “Cellular contact guidance emerges from gap avoidance”. In: *Cell Reports Physical Science* 1.5 (2020), p. 100055.

[31] Manuel Théry et al. “The extracellular matrix guides the orientation of the cell division axis”. In: *Nature cell biology* 7.10 (2005), pp. 947–953.

[32] Alexandra Fink et al. “Area and geometry dependence of cell migration in asymmetric two-state micropatterns”. In: *Biophysical journal* 118.3 (2020), pp. 552–564.

[33] Christina L Dix et al. “The role of mitotic cell-substrate adhesion re-modeling in animal cell division”. In: *Developmental cell* 45.1 (2018), pp. 132–145.

[34] John R Davis et al. “Inter-cellular forces orchestrate contact inhibition of locomotion”. In: *Cell* 161.2 (2015), pp. 361–373.

[35] David Li and Yu-li Wang. “Coordination of cell migration mediated by site-dependent cell–cell contact”. In: *Proceedings of the National Academy of Sciences* 115.42 (2018), pp. 10678–10683.

[36] Elena Scarpa et al. “A novel method to study contact inhibition of locomotion using micropatterned substrates”. In: *Biology open* 2.9 (2013), pp. 901–906.

[37] Brian Stramer and Roberto Mayor. “Mechanisms and in vivo functions of contact inhibition of locomotion”. In: *Nature reviews Molecular cell biology* 18.1 (2017), pp. 43–55.

[38] Joe Steinman et al. “3D morphological analysis of the mouse cerebral vasculature: Comparison of in vivo and ex vivo methods”. In: *PloS one* 12.10 (2017), e0186676.

[39] Manuel Théry. “Micropatterning as a tool to decipher cell morphogenesis and functions”. In: *Journal of cell science* 123.24 (2010), pp. 4201–4213.

[40] Marina Krause et al. “Cell migration through three-dimensional confining pores: speed accelerations by deformation and recoil of the nucleus”. In: *Philosophical Transactions of the Royal Society B* 374.1779 (2019), p. 20180225.

[41] Haijiao Liu et al. “In situ mechanical characterization of the cell nucleus by atomic force microscopy”. In: *ACS nano* 8.4 (2014), pp. 3821–3828.

[42] Jan Lammerding. “Mechanics of the nucleus”. In: *Comprehensive physiology* 1.2 (2011), p. 783.

[43] Alexandra Lynn McGregor, Chieh-Ren Hsia, and Jan Lammerding. “Squish and squeeze—the nucleus as a physical barrier during migration in confined environments”. In: *Current opinion in cell biology* 40 (2016), pp. 32–40.

[44] Francisco J Calero-Cuenca, Cátia S Janota, and Edgar R Gomes. “Dealing with the nucleus during cell migration”. In: *Current opinion in cell biology* 50 (2018), pp. 35–41.

[45] Alex Mogilner. “On the edge: modeling protrusion”. In: *Current opinion in cell biology* 18.1 (2006), pp. 32–39.

[46] Matthew J Footer et al. “Direct measurement of force generation by actin filament polymerization using an optical trap”. In: *Proceedings of the National Academy of Sciences* 104.7 (2007), pp. 2181–2186.

[47] Archana Gengatharan, Rodrigo R Bammann, and Armen Saghatelyan. “The role of astrocytes in the generation, migration, and integration of new neurons in the adult olfactory bulb”. In: *Frontiers in neuroscience* 10 (2016), p. 149.

[48] Verónica Martínez-Cerdeño and Stephen C Noctor. “Neural progenitor cell terminology”. In: *Frontiers in neuroanatomy* 12 (2018), p. 104.

[49] Jean-Yves Tinevez et al. “TrackMate: An open and extensible platform for single-particle tracking”. In: *Methods* 115 (2017), pp. 80–90.

[50] Reinhold Fürth. “Die brownsche bewegung bei berücksichtigung einer persistenz der bewegungsrichtung. mit anwendungen auf die bewegung lebender infusorien”. In: *Zeitschrift für Physik* 2.3 (1920), pp. 244–256.

SUMMARY

Microscopy is the science of examining objects that are too small to be perceived by the human eye. Since microscopes became a popular tool in biological research in the 17^{th} century, this instrument has experienced an immense technological evolution. Particularly, fluorescence microscopy established as a highly valuable standard method in scientific research, giving rise to the development of an enormous range of fluorescent markers and materials. As cells are mainly composed of water and are translucent, fluorescent tagging allows to visualize and differentiate the different cellular structures. The establishment of an incubator stage opened the way to investigate living cells over days or weeks while the development of fast-scanning microscopes enabled fast imaging. Together with the possibility of time-lapse microscopy, whereby the software is programmed to automatically take images in regular time intervals over a set period of time, allowed to gain deeper insights into the dynamics of living cells and their interactions with fluorescent materials.

In this thesis, time-lapse fluorescent microscopy plays a pivotal role in investigating functional materials within living cells as well as the migratory behaviour of neural progenitor cells. The first part of the thesis focuses on two different functional nanomaterials, whereas the second part explores fluorescent labelling of neural progenitor cells and cell dynamics within different *in vitro* systems.

Fluorescent nanomaterials present an exceptionally practical tool to label cells and their organelles. Within the past decades high research effort has been put into developing materials that have a strong and robust fluorescence, that are easily taken up by cells and do not influence cellular processes or health. Further research effort went into designing functional fluorescent materials, that do not solely label an existing structure but respond to the processes inside cells and offer a variability in their response. For example, recent biochemical developments enabled to use the fluorescent signal as a voltage sensor within neurons, functioning as an indicator for neural activity. Along with these developments, chapter II introduces a fascinating hybrid material consisting of a combination of DNA molecules and silver clusters, called DNA-encapsulated silver nanoclusters (Ag-DNA). Ag-DNA show unique optical properties which are tuneable with the selection of the DNA sequence and length, as well as show high sensitivity to its environmental conditions. In other publications, these nanomaterials have been used for metal ions detection *in vitro* or DNA mismatch sensing. In Chapter II, we employ Ag-DNA in living cells and show how the selection of the DNA template influences the resulting structures and yields Ag-DNA constructs that perform different functions within cells. Specifically, we present three different Ag-DNA constructs that show different fluorescence responses upon internalization in cells, including characteristic excitation and emission shifts. Furthermore, by varying the DNA sequence and lenght, it is possible to tune the cytotoxicity of these nanomaterials, adding the possibility of anti-cancer or anti-bacterial applications.

Another category of fluorescent materials is introduced in Chapter III. This chapter focuses on polymersomes that are artifical vesicles consisting of a lipophilic membrane and an aqueous interior which can be loaded with different molecular entities. In our experiments, polymersomes labelled with two different fluorescent dyes are analyzed within living cancer cells. Time-lapse microscopy is employed to observe the internalization process and the fate of the polymersomes inside living cells over the period of 2 hours and 86 hours, respectively. We find that the cells rapidly internalize the dual-labelled nanovesicles and distribute them equally among daughter cells during division. Further, the fluorescence signal remains stable for up to 3 days thus showing the potential of these nanomaterials for long-term bioimaging applications.

The second part of the thesis turns its focus to the multipotent stem cells of the central nervous system – the neural progenitor cells (NPCs). Their multipotency and regenerative capacity makes them an outstanding candidate for the treatment of neurodegenerative diseases and injuries of the central nervous system. We employ the murine neural progenitor cell line C17.2 for our experiments. In chapter IV, we first confirm the neural progenitor state of undifferentiated C17.2 by using morphological analysis and fluorescent immunolabelling. By differentiating the cells into neurons and astrocytes, and using the same analysis methods, we also confirm the presence of their multipotency. Second, several fluorescent dyes and genetic markers are tested with the focus to label the nucleus and cell body or cytoskeleton of C17.2 cells. Finally, a viral dual-transduction is successfully performed and a stable cell line generated with a labelled nucleus and cytoskeleton. This fluorescent C17.2 line is employed in chapter V for the analysis of cellular dynamics.

Despite the numerous publications of studies showing the regenerative capability of neural progenitor cells in disease and injury animal models, basic insights into the migratory behaviour of these cells are missing. In chapter V we introduce different minimalistic *in vitro* systems that are used to produce preliminary results on neural progenitor cells dynamics. More specifically, we coat substrates with extracellular matrix proteins in a plain as well as in a patterned way and observe the behaviour of C17.2 cells under the different conditions via fluorescence time-lapse microscopy. We look at the general statistical values of their migration on plain surfaces and on confined patterns. We calculate the average times that C17.2 cells move into one direction before changing, as well as their average velocities and diffusion values on plain surfaces and on patterned lines of different widths. Furthermore, we find that the NPCs follow a persistent random motion model, whereby they show persistence on short time scales but random motion on long time scales. Additionally, visual analysis of these cells within different patterned environments yielded insights into a set of recurrent behaviours including their frequent turns of direction to explore their environment and their competition for space. The preliminary results can be used for initial modeling purposes focused on understanding how NPCs migrate *in vivo*. All introduced experimental set-ups can be employed in future studies to perform more detail analysis and higher complexity like chemical guidance gradients can be added to mimic the *in vivo* situation closer.

The research presented in this thesis covers different topics that are all joined by the employed investigative tool of spinning disc confocal fluorescent microscopy and the application of fluorescent materials and markers with living cell systems. The presented

results provide new information on how the selection of a DNA template yields Ag-DNA constructs with different functionalities within living cells. It shows the possibility of these materials to be used as stable fluorescent labels for cells, as intracellular sensors, or have the purpose of causing cell death. The observations on the second investigated fluorescent material, dual-fluorescent polymersomes, contribute to our understanding of the short- and long-term fate of these nanovesicles within living cells allowing their application as fluorescent trackers in other biological system. The established stably fluorescent NPCs enable other researchers to use this reporter-cell line for other studies. Lastly, the presented minimalistic *in vitro* systems and the acquired first insights into the dynamics and behaviour of neural progenitor cells set a starting point for further and more detailed analysis of these cells that are crucial for future regenerative treatments of the central nervous system.

SAMENVATTING

Microscopie is de wetenschap van het onderzoeken van objecten die te klein zijn om waar te nemen met het blote oog. Sinds microscopen populaire gebruiksvoorwerpen werden voor biologisch onderzoek in de zeventiende eeuw, hebben deze instrumenten een immense technologische revolutie ondergaan. Vooral fluorescentie microscopie heeft zijn weg gebaand in wetenschappelijk onderzoek, waaraan de ontwikkeling van een enorme hoeveelheid aan fluorescente markers en materialen gepaard ging. Gezien cellen vooral uit water bestaan en doorschijnend zijn, kunnen verschillende cellulaire structuren gevisualiseerd en onderscheiden worden door ze fluorescent te markeren. De integratie van het incubatie-platform opende het pad naar het onderzoeken van levende cellen over periodes van dagen en zelfs weken, terwijl de ontwikkeling van snelscannende microscopen ons in staat stelde snel afbeeldingen te maken. Gecombineerd met tijdsverloop-microscopie, waarbij software zo geprogrammeerd wordt dat er automatisch afbeeldingen gemaakt worden op regelmatige tijdsintervallen over een bepaald tijdsbestek, werd het mogelijk om diepere inzichten te krijgen in de dynamica van levende cellen en hun interactie met fluorescerende materialen.

In dit proefschrift speelt tijdsverloop-microscopie een cruciale rol in het onderzoeken van functionele materialen binnenin levende cellen, en het migratie-gedrag van neuronale progenitorcellen. Het eerste gedeelte van dit proefschrift focust zich op twee verschillende (nano)materialen, en het tweede gedeelte behandelt het fluorescente labelen van neuronale progenitorcellen en cel dynamiek binnen verschillende in vitro systemen.

Fluorescente nanomaterialen presenteren zichzelf als exceptionele praktische werktuigen voor het labelen van cellen en hun organellen. Gedurende de voorgaande decennia is er veel moeite gestopt in het ontwikkelen van materialen die sterke en robuuste fluorescentie hebben, gemakkelijk worden opgenomen door cellen, en niet de cellulaire processen en de gezondheid van de cel beïnvloeden. Verder onderzoek werd er gedaan naar het ontwikkelen van functionele fluorescente materialen die niet alleen een bestaande structuur labelen, maar ook nog reageren op processen binnenin de cel en een variabiliteit in hun respons bieden. Bijvoorbeeld, een ontwikkeling in de biochemie maakt het mogelijk om een fluorescent signaal te gebruiken als spanningsensor binnenin neuronen, daarbij functionerend als een indicator voor neurale activiteit. Gepaard met deze ontwikkelingen, introduceert hoofdstuk II een fascinerend hybride materiaal bestaande uit een combinatie van DNA-moleculen en zilveren clusters, een DNA-omsloten zilveren nanocluster (Ag-DNA) genaamd. Ag-DNA vertoont unieke optische eigenschappen die afgestemd kunnen worden door middel van de DNA-sequentie en DNA-lengte, en is zeer gevoelig voor de omgevingscondities. In vorige publicaties werden deze nanomaterialen gebruikt voor het detecteren van metaalionen in vitro of om verkeerde combinaties in DNA-sequenties op te sporen. In Hoofdstuk II gebruiken we Ag-DNA in levende cellen en laten we zien hoe de selectie van het DNA-sjabloon de re-

sulterende structuren beïnvloed en Ag-DNA constructies teweegbrengt die verschillende functies uitvoeren binnenin de cel. Meer specifiek gekeken, presenteren we drie verschillende Ag-DNA constructen die verschillende fluorescerende reacties hebben wanneer deze worden opgenomen in levende cellen, inclusief karakteristieke excitatie- en emissie- verschuivingen. Verder was het mogelijk om de cytotoxiciteit van deze nanomaterialen zo af te stemmen, door de DNA-sequentie en lengte te variëren, dat deze juist biocompatibel werden en mogelijk interessant kunnen zijn voor antikanker of antibacteriële toepassingen.

Een andere categorie van een fluorescerend materiaal wordt geïntroduceerd in Hoofdstuk III. Dit hoofdstuk focust zich op polymersomen, dat zijn synthetische blaasjes bestaande uit een lipofiel membraam en een waterige binnenkant die geladen kan worden met verschillende moleculaire entiteiten. In onze experimenten worden polymerosomen geladen met twee verschillende fluorescerende kleurstoffen en geanalyseerd in levende kankercellen. Tijdsverloop-microscopie wordt ingezet om het internalisatieproces te analyseren en het lot van de polymerosomen in levende cellen te volgen gedurende een tijdsbestek van twee uren en 86 uren, respectievelijk. We zien dat cellen de dubbel-gelabelde nanoblaasjes snel internaliseren en deze gelijkmatig verdelen over de dochtercellen gedurende de celdeling. Ook blijft het fluorescente signaal stabiel tot drie dagen, waarmee de potentie van deze nanomaterialen voor lange-termijn biologische studies wordt aangetoond.

Het tweede gedeelte van dit proefschrift is gefocust op de multipotente stamcellen van het centrale zenuwstelsel – neurale progenitorcellen (NPCs). Hun multipotente en regeneratieve capaciteiten maken ze uitstekende kandidaten voor het behandelen van neurodegeneratieve ziekten en letsels in het centrale zenuwstelsel. Wij gebruiken de murine neurale progenitorcellijn C17.2 voor onze experimenten. In Hoofdstuk IV bevestigen we eerst de neurale progenitor status van ongedifferentieerde C17.2 door gebruik te maken van morfologische analyse en fluorescente immunolabels. Als tweede worden verschillende fluorescente kleurstoffen en genetische labels getest met als doel de nucleus en cellichaam of cytoskelet van C17.2 cellen te labelen. Als laatste wordt een virale dubbel-transductie met succes uitgevoerd waarbij een stabiele cellijn ontstaat met gelabelde nucleus en cytoskelet. Deze fluorescente C17.2 cellijn wordt gebruikt in hoofdstuk V voor de analyse van cel dynamica.

Ondanks talrijke publicaties omtrent de regeneratieve capaciteiten van neurale progenitor in ziekte- en letselstudies in dierenmodellen, ontbreekt er basiskennis over hun migratiegedrag. In Hoofstuk V introduceren we verschillende minimalistische in vitro systemen die gebruikt worden voor het produceren van preliminaire resultaten omtrent de dynamica van neuronale progenitor cellen. We coaten substraten met extracellulaire matrix eiwitten in zowel een simpel vlak als een in een patroon, vervolgens observeren we het gedrag van C17.2 cellen in verschillende condities via fluorescente tijdsverloop-microscopie. We kijken naar de algemene statistische waardes van hun migratie op eenvoudige oppervlaktes en begrensde patronen. We berekenen de gemiddelde tijden waarin C17.2 cellen in een bepaalde richting bewegen tot wanneer ze van richting veranderen. Ook wordt hun gemiddelde snelheid en diffusiewaarden berekend op simpele oppervlaktes en op patronen waarbij lijnen zijn aangebracht met verschillende breedtes. Ook observeren we dat NPCs een persistent willekeurig bewegingsmodel volgen, waarbij

ze persistent over kortere tijdschalen zijn, maar willekeurig bewegen over langere tijdsschalen. Door middel van visuele analyse hebben we inzicht gekregen in een set van terugkerend gedrag, waaronder frequente veranderingen in richting om de omgeving te verkennen en hun competitie naar ruimte, wanneer deze cellen zich in verschillende omgevingen bevinden met verschillend patronen. Deze vroegtijdige resultaten kunnen gebruikt worden voor de eerste wiskundige modellen die zich focussen op het begrijpen van hoe NPCs migreren in vivo. Alle geïntroduceerde experimentele opstellingen kunnen gebruikt worden in vervolgstudies om in een nog groter detail en complexiteit de metingen te doen, chemische sturingsgradiënten kunnen bijvoorbeeld toegevoegd worden om de in vivo situatie nauwkeuriger na te bootsen.

Het onderzoek dat beschreven wordt in dit proefschrift behelst verschillende onderwerpen die verbonden zijn door de gebruikte afbeeldingstechniek van draaischijf confocale fluorescentie microscopie en de gebruikte fluorescente materialen en markers in levende cel systemen. De gepresenteerde resultaten verschaffen nieuwe informatie in hoe de selectie van een DNA-sjabloon Ag-DNA moleculen voortbrengt met verschillende functionaliteiten in levende cellen. Het laat ook zien dat deze materialen gebruikt kunnen worden als stabiele fluorescente labels in cellen – als intracellulaire sensoren – of als werktuigen om celdood te bewerkstelligen. De observaties omtrent de duo-fluorescente polymerosomen helpen mee aan ons begrip van wat het lot is van deze nanoblaasjes op zowel korte- en lange- termijn in levende cellen, en maakt het mogelijk om ze te gebruiken als fluorescente labels in andere biologische systemen. De vastgestelde stabiele fluorescente NPCs kunnen gebruikt worden door onderzoekers voor vervolgstudies. Als laatste, de gepresenteerde minimalistische in vitro systemen en de verworven eerste inzichten in het dynamische gedrag van neurale progenitor cellen, markeren een startpunt voor verder en gedetailleerdere analyse van deze cellen die cruciaal zijn voor het ontwikkelen van toekomstige behandelingen tegen regeneratieve ziektes van het centrale zenuwstelsel.

CURRICULUM VITÆ

Nelli BOSSERT

08-07-1986	Born in Kokchetav, Kazakhstan.

EDUCATION

1993–1998	Elementary School Kokchetav, Kazakhstan (1993–1996) Pirmasens, Germany (1996–1998)
1998–2007	Secondary and Highschool Pirmasens, Germany
2009–2012	Bachelor in Science Julius Maximilians University (JMU), Würzburg, Germany *Thesis:* Expressional Profile of Candidate Genes of Psychiatric Disorders in the Murine Brain *Host:* Neurobiological Laboratory at Medical Centre for Psychiatry, Psychosomatics, and Psychotherapy
2012–2014	Master in Science Julius Maximilians University (JMU), Würzburg, Germany *Thesis:* Modeling of the Blood-Brain Barrier using Murine Endothelial Cells and Astrocytes *Host:* Tissue Engineering and Regenerative Medicine
2015–2021	PhD in Biophysics Leiden University, Netherlands
From 2021	Marketing Coordinator DSM LUMICKS, Amsterdam

LIST OF PUBLICATIONS

- **N. Bossert**, D. de Bruin, M. Götz, D. Bouwmeester, and D. Heinrich, *Fluorescence-tunable Ag-DNA biosensor with tailored cytotoxicity for live-cell applications*, Scientific Reports **6**, 1 (2016) .

- L. Weissflog, N. Becker, **N. Bossert**, F. Freudenberg, S. Kittel-Schneider, and A. Reif, *Expressional profile of the diacylglycerol kinase eta gene DGKH. European archives of psychiatry and clinical neuroscience*, European archives of psychiatry and clinical neuroscience **267**, 445 (2017).

- C. van der Wel, **N. Bossert**, Q. J. Mank, M. G. Winter, D. Heinrich, and D. J. Kraft, *Surfactant-free colloidal particles with specific binding affinity*, Langmuir **133**, 9803 (2017).

- S. C. H. Askes, **N. Bossert** J. Bussman, V. S. Talens, M. S. Meijer, R. E. Kieltykaa, A. Kros, S. Bonnet, and D. Heinrich, *Dynamics of dual-fluorescent polymersomes with durable integrity in living cancer cells and zebrafish embryos*, Biomaterials **168**, 54 (2018).

- D. de Bruin, **N. Bossert** A. Aartsma-Rus,and D. Bouwmeester, *). Measuring DNA hybridization using fluorescent DNA-stabilized silver clusters to investigate mismatch effects on therapeutic oligonucleotides*, Journal of nanobiotechnology **16**, 1 (2018).